POLITECNICO DI MILANO

School of Industrial Engineering and Information
Master of Science in Mechanical Engineering
Department of Mechanical Engineering

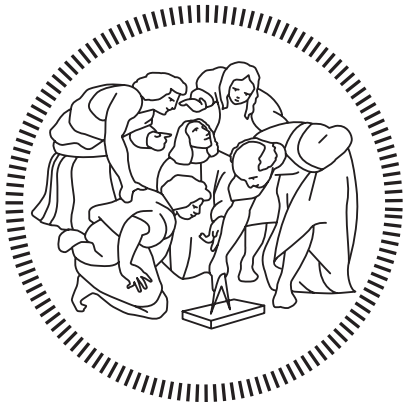

ASSESSMENT OF A NUMERICAL PROCEDURE TO EVALUATE THE SAFETY PERFORMANCE OF AN FHR DEVICE IN TERMS OF HUMAN NECK LOADS

Advisor: Prof. Marco ANGHILERI
Coadvisor: Ing. Paolo PANICHELLI

M.Sc. Thesis by:
Michele ROSSI - ID: 920972

Academic Year 2021/2022

Engineering is the art of modelling materials we do not wholly understand, into shapes we cannot precisely analyse so as to withstand forces we cannot properly assess, in such a way that the public has no reason to suspect the extent of our ignorance.

Dr. AR Dykes

Abstract

Front Head Restraint (FHR) devices have been introduced since the early 1980's to reduce the high number of serious head and neck injuries in motorsport auto racing. The aim of this study is to evaluate the safety performance of FHR devices in terms of human neck loads using the THUMS Human Body Model. The purpose has been pursued by considering three possible injury criteria and approaches. The first injury criterion, it is derived from N_{ij} criterion for Hybrid III dummy and it is based on force and moment calculation on THUMS' vertebral sections. The second criterion is based on anatomy studies and in particular on RoM of cervical spine segments. The third criterion is based on osteology and especially on the plastic strain that causes bone fractures. Initially, an experimental sled testing campaign with the Hybrid III anthropomorphic test device has been performed in the La.S.T. - TRANSPORT SAFETY LAB of the Politecnico di Milano's Aerospace Science and Technology Department. In these tests, four different Hybrid III dummy configurations, with and without FHR devices, have been tested with always the same range of deceleration around 70 g. The acquired experimental data have been used to validate Hybrid III Finite Element models created reproducing the experimental setups. These validated Finite Element models then have been used with the THUMS in order to compare the human neck loads and assess neck injury criteria.

KEYWORD: FHR, THUMS, Hybrid III, neck injury, crash test, frontal impact, Nij, HANS, Hybrid PRO, Finite Element simulations, LS-DYNA®, PRIMER®.

Acknowledgments

I would like to thank a number of people for their help and support during the production of this thesis. First of all, I would like to thank my advisor, Prof. Marco Anghileri, for putting me in touch with FIA and for giving the possibility to work on a so interesting topic. Thanks to FIA for giving me the chance to work with Ing. Paolo Panichelli on this project. Thanks to Paolo himself, for being always available at any time and day to solve doubts and problems, for having transmitted me the passion for this field of study that is passive safety, for the patience, for the advices even not related to this work itself and for the conversations about time and physics. Thanks to LaST personnel, especially Ing. Andrea Milanese and the laboratory technicians Adriano and Mirko for helping me in the experimental tests and for the lunches based on *pasta aglio, olio e peperoncino.* Thanks to Ing. Ivan Colamartino and Ing. Giulia Vignati that helped me with the "smart working" issues. Thanks to the other LaST master thesis' students, in particular Marco and Claudio for sharing this adventure, problems and lunches.

I cannot forget to thank my family, especially thank you to my parents, for your endless support and for always giving me the opportunity to do what I like. Thank you to my grandparents for always being proud of me, to my sisters for the help given also in this thesis and to my little nieces for always making me smile. Thanks to Sara for sharing with me this journey, for supporting me and putting up with me. Thank you to Gianluca for helping me in the video editing for this thesis. To conclude, thank you to Dynamis PRC. You truly have been a family to me.

Thank all of you for being part of my most beautiful memories in these years.

Contents

List of Figures

List of Tables

Chapter 1

Introduction

The aim of this chapter is to briefly describe the main topics and objectives of the work. This thesis was made in collaboration with FIA[1].

1.1 Work Objectives

There are many dangers associated with motorsport auto racing, as with other sports, but the risks tend to be more heightened and often more real. This is because of a combination of reasons that include the speed of the cars, the conditions of the tracks, circuits and roads, the elements of the car that present the risk of malfunction, as well as the fact that there are many other drivers racing alongside each other. The most obvious, notable and frequent risk is that of crashing. It happens often and to varying degrees depending on the type of race, the type of car and the driver. This risk is simply inevitable and hard to minimize. Depending on the severity of the crash, injuries can compromise the motor skills of the occupants, or even cause death. Since the early 1900s, more than 500 drivers died in crashes related to the sport of auto racing, in races, in qualifying, in practice or in private testing sessions [50]. At least 150 of which, caused by a broken neck or severe neck injuries [3]. These are one of the most common and dangerous injuries caused by car crashes. In frontal impacts, the vehicle is subjected to a forced backward acceleration, but the head lags behind and so the neck is forced into a motion called whiplash motion [17].

To practically reduce these types of injuries, Frontal Head Restraint (FHR) devices have been introduced and become mandatory in most of the motorsport competitions. An FHR restrains the driver's head relative to his torso during a frontal or angled-frontal impact thereby, trying to reduce the loads in the neck. The two main types of FHR homologated by FIA are the Head And Neck Support (HANS) system and the Hybrid/Hybrid PRO system, whose characteristics will be discussed later in this Chapter 2.1.

Another way to prevent neck injuries is the use of some criteria or approaches, applied in

[1] Fédération Internationale de l'Automobile

certification tests for cars, motorbikes and safety devices to study neck injuries. These tests make use of the so-called Anthropomorphic Test Devices (ATD) and with these criteria we can understand if the analyzed test situation can lead to severe injuries to the human neck. But it is not possible to repeatedly perform ATD tests because of their cost in terms of both money and time. Nowadays, Finite Element Methods (FEM) are popular and diffused tools for the crash investigation. FEMs offer the possibility to run several numerical simulations saving time and money while maintaining test repeatability. In order to perform Finite Element Analysis (FEA), Finite Element (FE) models of ATD and Human Body Models (HBM) have been implemented. The former has a lower biofidelity than the latter, as it has to match a real dummy. Mannequin are developed to be enough durable to perform repeatable tests. Hence, HBMs provide a better prevision of the human kinematic during crashes. THUMS[2] is one of the most popular HBM in crashworthiness, but there are no official neck injury criteria that are used for assessing neck injury in numerical simulations.

The aim of this study is to evaluate the safety performance of FHR devices in terms of human neck loads using the THUMS Human Body Model. The purpose has been pursued by considering three possible injury criteria and approaches. The first injury criterion, it is derived from N_{ij}[3] criterion for Hybrid III dummy and it is based on force and moment calculation on THUMS' vertebral sections. The second criterion is based on anatomy studies and in particular on RoM[4] of cervical spine segments. The third criterion is based on osteology and in particular on the plastic strain that causes bone fractures. The THUMS crash test models have been created on the basis of an FE model with the Hybrid III, validated through the data obtained from experimental tests.

1.2 Problem definition

The first part of the work consisted in planning and performing an experimental test campaign of frontal impacts using the Hybrid III ATD, placed on a reclined seat sled with six-points racing harnesses mounted. The tests were made in the La.S.T. - TRANSPORT SAFETY LAB of the Politecnico di Milano's Aerospace Science and Technology Department, testing four different dummy configurations with always the same range of deceleration around 70 g:

1. Dummy witohut helmet
2. Dummy with helmet
3. Dummy with helmet and HANS device
4. Dummy with helmet and Hybrid PRO device

[2]Total HUman Model for Safety
[3]Normalized Neck Injury Criterion
[4]Range of Motion

Then, FE models of the experimental setups have been created matching the geometries and positions of the real ones, and combined with the Hybrid III FE model provided by FIA. The validation of the FE model was carried out by comparing the results of the real crash tests conducted on the real dummy, with the results of the numerical simulations. After having validated it, the THUMS model replaced the Hybrid III one, and all the numerical simulations have been redone. Finally, from the THUMS results, the safety performance of the FHR devices have been evaluated, using the criteria previously presented. All the numerical simulation has been done using the LS-DYNA® solver software. The LS-DYNA keyword input files were created by using the PRIMER® software environment.

Chapter 2

State of the Art

This chapter gives the reader an overview on the history and characteristics of the FHR devices, on the development of passive safety and neck injury criteria, and describes the anatomy of the neck and cervical spine in particular. Regarding passive safety, the main focus will be the development of numerical models and the reasons behind their implementation. The FE models used in the work are described too, as they are indispensable to understand the work done.

2.1 Front Head Restraint devices

Fatal craniovertebral junction (CVJ) injuries were the most common causes of death in high-speed motor sports prior to 2001. [3] Following the death of a mutual friend and race car driver, the biomechanical engineer Dr. Robert Hubbard, along with race car driver and brother-in-law Jim Downing, developed the concept for the Head and Neck Support (HANS) device, the first Front Head Restraint (FHR) model. Nowadays these devices are mandatory in most of the motor sport competitions and they must be homologated by the FIA, passing the SFI SPECIFICATION 38.1 [27].

According to clinical literature, basilar skull ring fractures occur from distraction or compressive forces. [32, 48] Compression ring fractures occur from a vertical fall from a height or direct impact to the top of the head and are often associated with fatal downward displacement of the posterior fossa, brainstem, and vascular structures. Flexion- distraction ring fractures and atlantooccipital dislocations occur when forces applied to the head are sufficient to cause suture diastasis during acceleration experienced by the head and torso, which is often fatal as well. [4, 5, 26, 43, 51] Pollanen et al. evaluated a series of eight fatal basilar skull fractures and found that fractures of the petrous portion of temporal bones will often involve laceration of the internal carotid arteries, leading to massive hemorrhage. These fractures can involve the middle ear as well and create a carotid–middle ear fistula leading to rapid exsanguination. [40]

To reduce the probability to have these injuries, the FHRs use a raised collar and two

polyester-fabric tethers to secure the driver's head. The driver's shoulder belts hold the tall, stiff collar securely in place. The tethers link the sides of the driver's helmet to collar anchor points. When g-loads build during a forward impact, the HANS device assures that the driver's helmeted head moves with his torso so vulnerable neck and skull bones are not overloaded.

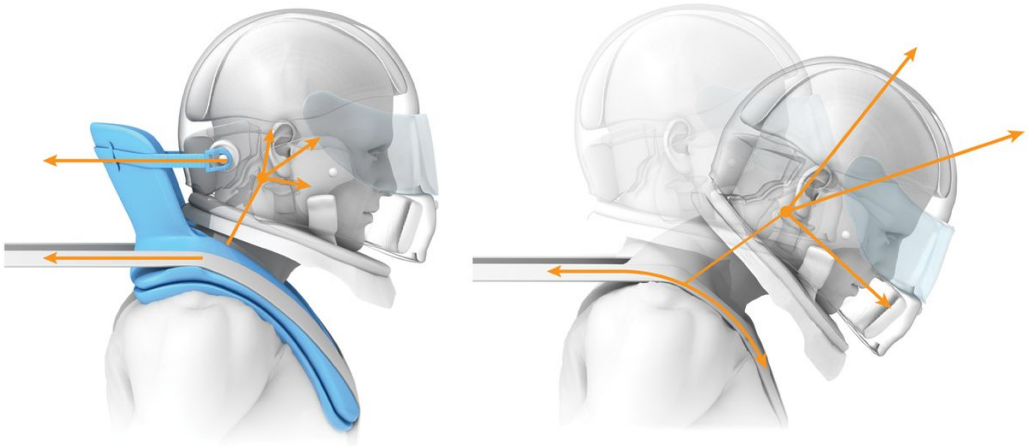

Figure 2.1: Forces exchanged with and without HANS device (ROY RITCHIE).

There are two main types of FHR:

- Head And Neck Support (HANS)
- Hybrid/Hybrid PRO

2.1.1 The HANS device

Dr. Robert Hubbard, a biomechanical engineer at Michigan State University, and his brother-in-law Jim Downing, a race car driver, developed the concept for the Head and Neck Support (HANS®) device following the death of a mutual friend and race car driver, Patrick Jacquemart (1946–1981). [41]

The initial prototype of the HANS device was designed to fit elegantly over the driver's shoulders and attach to the helmet, allowing for increased resistance to flexion and distraction vectors during deceleration, deflecting translational head motion into the torso. The helmet did not significantly limit the driver's vision, because the driver's head could maintain some lateral and rotational movement due to the use of fixed-length sliding tethers on either side of the helmet. [41] To study the effectiveness of the device Hubbard used crash sled tests founding a significant reduction in neck loading. Following the death of Formula 1 driver Aryton Senna in 1994, DaimlerChrysler® investigated sled testing with the HANS device, concluding that the device was both efficacious and safe. [20, 21] With the cooperation of DaimlerChrysler®, the second-generation HANS device was created. [20]

Figure 2.2: Photograph of the HANS device coinventors: Dr. Robert Hubbard (left) with race car driver and brother-in-law Jim Downing (right). (copyright Richard Dole).

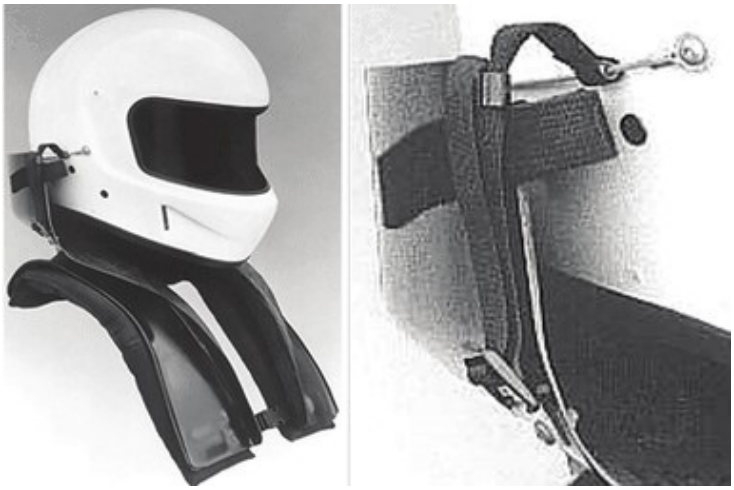

Figure 2.3: The first-generation HANS device (1990).

The adoption rate for the HANS device by race car drivers remained poor, however, because even with research and testing indicating their potential safety benefit, marketing and awareness of these devices lagged behind for nearly 5 years. [34] This delay continued until 2001 when, during his final lap of the Daytona 500, Dale Earnhardt Sr. was involved in a fatal collision. Root-cause analysis of his death determined that his car decelerated so rapidly that he suffered a fatal CVJ injury. Analyses of the crash component velocity vectors demonstrated that Earnhardt's car had an impact velocity in excess of 150 *mph* and experienced a total deceleration of 45–50 *g*. The final cause of death was found to be a fatal CVJ injury with an associated basilar ring fracture; however, the mechanism of fracture was heavily debated. The official NASCAR crash report explained that impact to the occipital scalp in conjunction with the tension and torsion stress to the base of the skull resulted in the fracture, and additional consultation by Dr. Barry Myers described a "whip" mechanism resulting from the differential restraint of the torso and head, leading to a lethal

flexion-distraction injury. [12] Earnhardt's crash marked a turning point for the adoption of head and neck restraint systems, with NASCAR mandating the use of these restraint systems in cars in 2001. In 2002, at the Italian Grand Prix, Felipe Massa became the first man to wear the HANS device during a Formula One race. The Fédération Internationale de l'Automobile (FIA) mandated the use of the third-generation HANS device for Formula One racing in 2003. Acceptance by drivers was helped by the addition of quick-release shackles developed and implemented by Ashley Tilling. They were sourced from the marine industry, being used on racing sailboat rigging. The shackles allowed the drivers a simple and quick pull to release the HANS device and exit their vehicle. The World Rally Championship and Australian V8 Supercar Series made the device compulsory for drivers in the 2005 season.

Figure 2.4: The third-generation HANS device.

2.1.2 The Hybrid FHR device

Initially the HANS was the only FHR device accepted by the FIA. However, from 2010 it approved an alternative frontal head restraint system for competitive racing, known as the Hybrid. The Hybrid device was added to the FIA Technical List and has become popular particularly for drivers and co-drivers who participate in rallying.

The Hybrid (and Hybrid Pro) was developed by Safety Solutions Inc® now owned by Simpson Motorsport®. Both use a combination of straps around the driver's body to maintain the position of a rigid collar, which provides a load path from the shoulder belts to the helmet using flexible tethers. As for the HANS, the Hybrid is designed to protect during both frontal collision and angled-frontal impacts. Some drivers find it more comfortable, particularly with upright seat types and it is used by a number of rally drivers or co-drivers, as it allows them to easily remove their helmet for road sections and keep the device attached

Figure 2.5: Simpson® Hybrid PRO device.

to their body. [10] The main difference from the HANS, is that the Hybrid has two tethers on each side, and this allows to not only protect drivers involved in a front-on collision but also angled-frontal impacts thanks to the innovative design.

2.2 Injury Criteria

In this section, the injury criteria used in the thesis are described. The first criterion is commonly used in sled test performed on ATD and was formulated by Mertz et al. [35] also making use of PMHS[1]. The other criteria are given by osteology scientific literature.

2.2.1 Nij Criterion

The N_{ij} criterion was developed by the *US National Highway Traffic Safety Administration* for the prevention of spinal injuries caused by frontal impacts [16]. It states that the linear combination of normalized neck axial load and normalized moment about the occipital condyle must not be higher than 1.0 at any point in time. The normalization is

[1] Post Mortem Human Subjects

done using force and moment limits defined for traction, compression (forces), extension and bending (moments). Indeed, the i and j of N_{ij} indicates the aforementioned loads, resulting in four possible loading conditions: tension-extension (N_{te}), tension-flexion (N_{tf}), compression-extension (N_{ce}), or compression-flexion (N_{cf}). At each point in time, only one of the four loading conditions occurs and the Nij value corresponding to that loading condition is computed and the three remaining loading modes shall be considered a value of zero. The criterion is expressed as:

$$N_{ij} = \frac{F_z}{F_{lim}} + \frac{M_y}{M_{lim}} \tag{2.1}$$

F_z is the axial load, M_y is the moment about the occipital condyle and F_{lim} and M_{lim} are the critical values of force and moment. The load limits depend on the dummy involved in the test and are listed in the table below [11, 16]:

Dummy	M_y (flexion / extension) ($N{\cdot}m$)	F_z (compression / tension) (N)
HIII 50%	310 / 135	6160 / 6806
HIII 5%	155 / 67	3880 / 4287
HIII 6-year-old	93 / 37	2800 / 2800
HIII 3-year-old	68 / 27	2120 / 2120

Table 2.1: Critical value of force and moment for different dummies

There are also limits on the single force peaks [38]:

- *Peak tension*. Tension force (F_z), measured at the upper neck load cell, shall not exceed 4170 N at any time.

- *Peak compression*. Compression force (F_z), measured at the upper neck load cell, shall not exceed 4000 N at any time.

The limits given by the combination of force and moment, and the ones given by the force peaks, are represented by an hexagon in Figure2.6. Graphically, the region inside the dashed lines shows the region for all four modes of loading which would pass the performance requirements for N_{ij}.

Since each specific dummy has a unique set of critical intercept values, for subsequent scaling this plot has been normalized by dividing each semi-axis by its critical intercept value, in our case the HIII 50% values showed in Table2.1. Graphically, the box inside the dashed lines designates the allowable values of loads and moments represented by the normalized calculation.

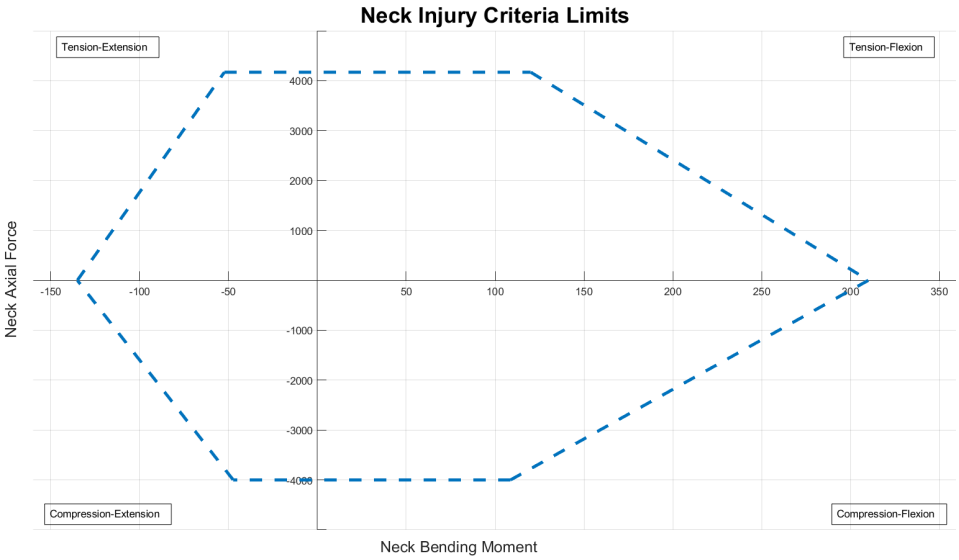

Figure 2.6: N_{ij} force and moment limits

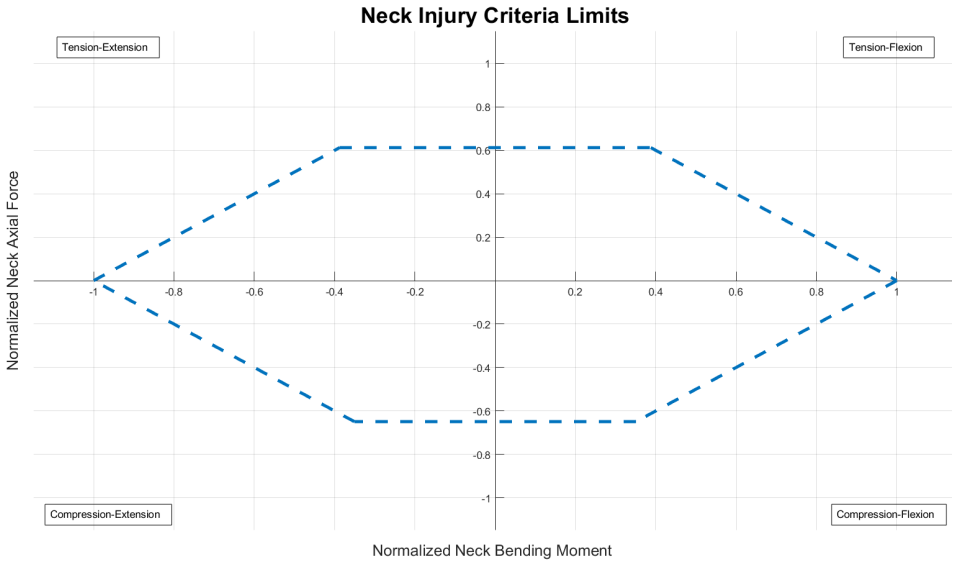

Figure 2.7: Normalized N_{ij} force and moment limits

Abbreviated Injury Scale for Nij criterion The *Abbreviated Injury Scale* also known as *AIS* is an injury scale that defines the severity of injuries. Table 2.2 shows the description of the six levels of AIS [42]. *AIS* can be applied to different injury criterion for creating the so called risk curves. In Figure 2.8 are reported the risk curves for N_{ij} criterion [13].

AIS	Level	Description
1	minor	Light lesion to the brain, headache, vertigo but no loss of consciousness; light cervical lesion, whiplash and contusions.
2	moderate	Contusions with or without cranium fractures, less than 15 minutes of loss of consciousness, little corneal crack, retina separation, nose fracture and face damages.
3	serious	Contusions with or without cranium fractures, more than 15 minutes of loss of consciousness without severe neurological damage, clean break of the cranium or compound break but no loss of consciousness; other damages as vision loss, fracture of face bones, cervical fracture with no marrow damage.
4	severe	Cranium fracture with severe neurological damages.
5	critical	Concussion with or without cranial fracture, more than 12 hours of unconsciousness, hemorrhage in the vicinity of the cranium and/or critical neurological damages.
6	fatal	Death, partial or total damages to the brainstem or to the upper part of the cervical zone, fracture and torsion of the cervical spine with marrow damages.

Table 2.2: AIS - Abbreviated Injury Scale

$$\text{Prob AIS2 } N_{ij} = 100 \cdot \left(1 + e^{2.0536 - 1.1955 \cdot N_{ij}}\right)^{-1}$$

$$\text{Prob AIS3 } N_{ij} = 100 \cdot \left(1 + e^{3.227 - 1.969 \cdot N_{ij}}\right)^{-1}$$

$$\text{Prob AIS4 } N_{ij} = 100 \cdot \left(1 + e^{2.693 - 1.196 \cdot N_{ij}}\right)^{-1}$$

$$\text{Prob AIS5 } N_{ij} = 100 \cdot \left(1 + e^{3.817 - 1.196 \cdot N_{ij}}\right)^{-1}$$

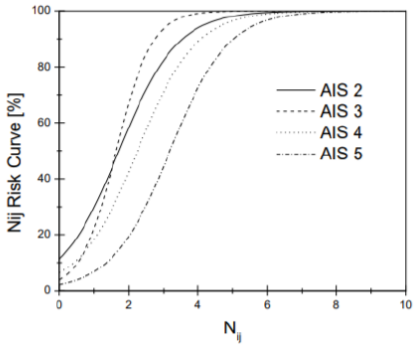

Figure 2.8: Neck injury risk curves corresponding to Nij criterion

2.2.2 Head-neck mobility

The neck contains seven cervical vertebrae that are linked with the occipital bone through the *atlanto-occipital joint*. The cervical segment itself is made of several joints. This structure allows the head to perform complex movements in the space. These movements are

basically a combination of four main rotations: flexion and extension in the sagittal plane, lateral flexion in frontal plane and axial rotation in transverse plane (shown in Figure 2.9).

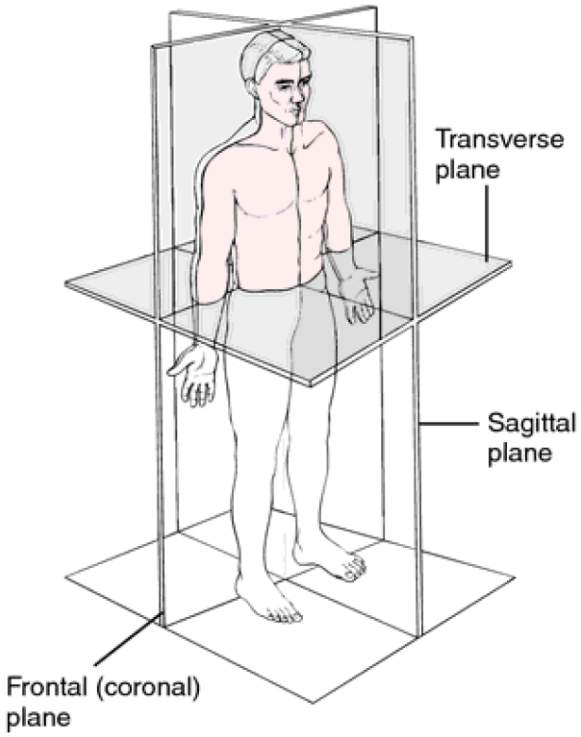

Figure 2.9: Body planes

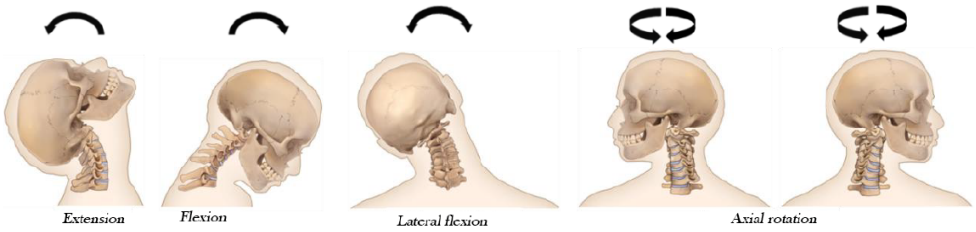

Figure 2.10: Head-neck kinematic movements

The mobility of the cervical spine has been widely studied in the recent years by using different methods; in vivo, by imaging or in vitro with cadaveric specimens. The kinematic of the cervical spine is studied by defining a *Funcional Spinal Unit (FSU)* that is composed of two vertebrae and a connecting element that usually is an intervertebral disc (IVD). The range of motion of different FSUs and of the segments of the cervical spine has been studied through cadavers' tests. In Table 2.3 are listed some RoM[2] for cervical FSU together with RoM for the upper cervical segment (C0[3]-C2) and for the lower segment (C2-C7). [8]

The cervical spine mobility can also be analyzed macroscopically, thus focusing on the

[2]Range of Motion
[3]Occipital condyle

Average Values (degrees)	C0-C1	C1-C2	C2-C3	C3-C4	C4-C5	C5-C6	C6-C7	C0-C7 (total)	C0-C2 (total)	C2-C7 (total)
Flexion/ Extension	26.9± 11.8	18.4± 8.8	11.2± 4.8	16.4± 6.1	17.1± 5.3	18.7± 6.7	15.9± 4.9	116.9 ±20.2	45.2± 14.8	85.1± 18.9
Lateral flexion	9.8± 2.3	12.2± 8.5	11.7± 7.0	11.9± 6.0	10.9± 4.8	10.1± 5.2	9.3± 4.7	79.5± 20.8	20.2± 7.6	60.1± 24.9
Axial rotation	6.7± 6.4	73.4± 16.3	11.6± 8.6	11.6± 6.6	10.0± 5.9	10.3± 4.3	7.5± 4.3	128.5 ±19.4	80.4± 16.8	59.5± 26.9

Table 2.3: Range of motion for cervical FSU, upper, lower and whole segments during the main movements

movement of the whole spine through a global evaluation, but in this work the mobility was analyzed microscopically. It has to be noted that the mobility of cervical spine articulations has been shown not to differ significantly between men and women. It is also true, that can be consistently compromised by aging and by several pathologies [47].

2.2.3 Bone failure due to plastic strain

Another way for evaluating bone fracture consist in evaluating plastic strain. The plastic strain failure of bones has been studied by Burstein et al.(1976) and Mc- Calden et al.(1993). These studies defined a fracture criterion of 3% strain [31], valid for cortical bone material. Later studies on vertebrae attested the limit at 1-2% [45]. In this work we used a plastic strain limit equal to 2% because it was previously used by FIA in other projects as it was a reasonable value.

2.3 Crash test dummies

A crash test dummy, or simply dummy, is a full-scale anthropomorphic test device (ATD) that simulates the dimensions, weight proportions and articulation of the human body during a traffic collision. Dummies are used by researchers, automobile and aircraft manufacturers to predict the injuries a person might sustain in a crash. On August 31, 1869, Mary Ward became the first recorded victim of an automobile accident [39], but until the 1950s little attention was given to safety measure for vehicle accidents. Only after the end of WorldWar II, aviation service personal began to understand the importance of comprehending the effects of deceleration on human body. Colonel John Paul Stapp[4] can be considered a pioneer in this field of study. Starting from 1947, Stapp run several rocket sled tests, sometimes even offering himself as volunteer, for studying the effect of high deceler-

[4]Colonel John Paul Stapp (July 11, 1910 – November 13, 1999), M.D., Ph.D., was an American career U.S. Air Force officer, flight surgeon, physician, biophysicist, and pioneer in studying the effects of acceleration and deceleration forces on humans. He became known as "the fastest man on earth" after he reached a speed of 632 mph (1,017 km/h) and stopped in 1.4 seconds, as a volunteer for a deceleration test and survived.

ation on human body [44]. Initially, the purpose of these studies was to increase the safety for aeronautic pilots during deceleration situation e.g. during ejection from the aircraft, but soon were applied to the automotive safety. Even if Stapp program was fundamental to set the starting point for passive safety development, it soon became clear that his methods were not feasible, so human volunteers were replaced with inanimate object, animals or PMHS.

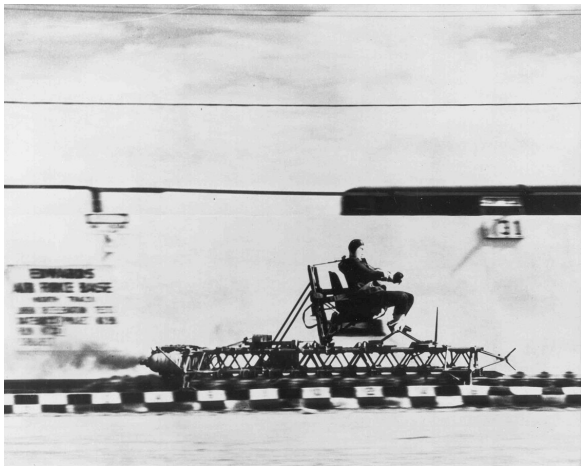

Figure 2.11: Colonel Stapp riding a rocket sled at Edwards Air Force Base

2.3.1 Cadaver testing

The use of human cadavers in crash test was introduced long before crash test dummies were conceived, being the closest available substitutes for the living human. Through cadavers it was possible to study the human body's ability to resist crushing and tearing forces in an accident, equipping them with accelerometers. But the use of cadavers involved limitation not only for ethical issues. During test people dead in accidents were not used, because the previous injuries would have compromised the measures. Instead, the candidates were old white people deceased without a violent death, but these didn't represent the average of population. Moreover it was wrong to compare data, because of all the cadavers were different and it was not possible to conduct the test more than once and they didn't provide information about accident survivability. However, Albert King's 1995 Journal of Trauma article, "Humanitarian Benefits of Cadaver Research on Injury Prevention", clearly states the value in human lives saved as a result of cadaver research. King's calculations indicate that as a result of design changes implemented up to 1987, cadaver research since saved 8,500 lives annually. He notes that for every cadaver used, each year 61 people survive due to wearing seat belts, 147 live due to air bags, and 68 survive windshield impact. [30]

2.3.2 Animal testing

The most common animal used during crash test was the pig, because of it's internal structure, similar to the human's one. Pigs can also be placed in a seated position in a good

approximation of a seated human. They were mainly used to study steering wheel impacts, but also for decapitation for example. [22] Also baboons and bears were used during test in order to measure injuries. Although it was easier to collect animal test data than cadaver data, often they were unrepeatable and some scientists argued that some injuries differences limited the usefulness of the results.

2.3.3 Dummy evolution

The first test mannequin, Sierra Sam, was created in 1949 by Samuel W. Alderson, at Alderson Research Labs, together with Sierra Engineering Co., the project supported by the United States Air Force (USAF). The dummy was involved in ejection seats, aviation helmets and pilot restraint harnesses tests. As it has to represent a member of aviation the mannequin was a 95th percentile male dummy (heavier and taller than 95% of human males) [49]. Regarding biofidelity, Sierra Sam had humanlike exterior shape, good weight and height reproduction and average accuracy of the ranges of motion for its articulated limb joints. The instrumentation installed was not particularly comprehensive: it was possible to measure only orthogonal linear head acceleration components. These defects encouraged the creation of other dummies.

Figure 2.12: Sierra Sam

General Motors (GM) engineers decided to combine the best features of two improvements of Sierra Sam, the VIP series (made by Alderson) and Sierra Stan (made by Sierra Engineering), and so in 1971 Hybrid I was born. [25] Hybrid I was what is known as a "50^{th} percentile male" dummy, so it modeled an average male in height, mass, and proportion.

Since then, considerable work has gone into creating more and more sophisticated dum-

mies. Hybrid II was introduced in 1972, with improved shoulders, spine, knee responses, and more rigorous documentation. Hybrid II became the first dummy to comply with the American Federal Motor Vehicle Safety Standard (FMVSS) for testing of automotive lap and shoulder belts. In 1973, a 50th percentile male dummy was released, and the National Highway Traffic Safety Administration (NHTSA) undertook an agreement with General Motors to produce a model exceeding Hybrid II's performance in a number of specific areas. [49]

Though a great improvement over cadavers for standardized testing purposes, Hybrid I and Hybrid II were still very crude, and their use was limited to developing and testing seat belt designs. A dummy was needed which would allow researchers to explore injury-reduction strategies. It was this need that pushed GM researchers to develop the current Hybrid line, the Hybrid III family of crash test dummies.

2.3.4 Hybrid III

The Hybrid III 50th Percentile Male Crash Test Dummy is the most widely used crash test dummy in the world for the evaluation of automotive safety restraint systems in frontal crash testing. Originally developed by General Motors, the Hybrid III 50th design is now maintained and developed by Humanetics in conjunction with the Society of Automotive Engineers' (SAE) Biomechanics Committees and the National Highway Transport and Safety Administration (NHTSA). The dummy is a regulated test device in the USA Code of Federal Regulations (Part 572, Subpart E) and also in the European ECE Regulations. It is considered to have excellent biofidelity and instrumentation capability. Recent revisions have improved the biofidelity in the femur range of motion and the ankle and foot. The dummy can also be used in many nonautomotive applications such as wheelchairs and medical and sport equipment. [24]

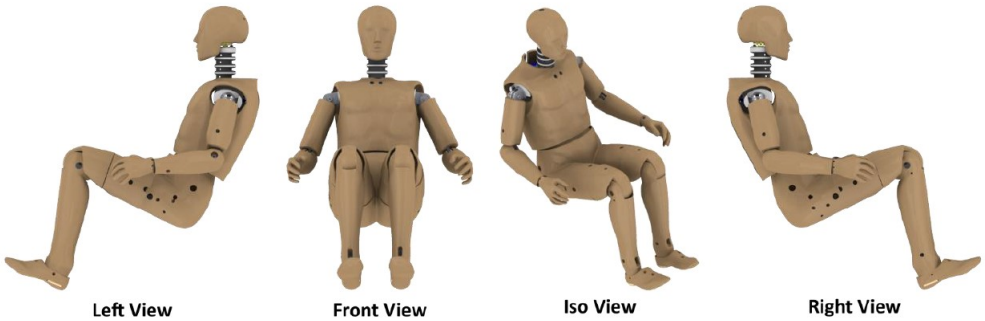

Figure 2.13: Hybrid III

The skull and skull cap are one piece cast aluminum parts with removable vinyl skins. The neck is a segmented rubber and aluminum construction with a center cable. It accurately simulates the human dynamic moment/rotation flexion and extension response.

The rib cage is represented by six high strength steel ribs with polymer based damping

material to simulate human chest force-deflection characteristics. Each rib unit comprises left and right anatomical ribs in one continuous part open at the sternum and anchored to the back of the thoracic spine. A sternum assembly connects to the front of the ribs and includes a slider for the chest deflection rotary potentiometer. The angle between the neck and upper torso is determined by the construction of the neck bracket which can incorporate a six-axis neck transducer. A two-piece aluminum clavicle and clavicle link assemblies have cast integral scapulae to interface with shoulder belts.

A curved cylindrical rubber lumbar spine mounts provides human-like slouch of a seated person and mounts to the pelvis through an optional three axis lumbar load cell. The pelvis is a vinyl skin/ urethane foam molded over an aluminum casting in the seated position. The ball-jointed femur attachments carry bump stops to reproduce the human leg to hip moment/rotation characteristics. The femur, tibia and ankle can be instrumented to predict bone fracture and the knee can evaluate tibia to femur ligament injury. The foot and ankle simulates heel compression and ankle range of motion.

Figure 2.14: Hybrid III Section

Key features that makes Hybrid III better than his predecessor Hybrid II:

- Improved biofidelity in the head, neck, thorax, pelvis, and knees
- Anatomically-improved head
- Neck has different flexion and extension response which is tested
- Thorax has improved biofidelic response to impact

- Lower torso uses the driver's slouch position with a curved lumbar spine, with two spine cables for better representation of dummy posture
- Tibia displacement measurement allowed for ACL[5] damage estimation
- Ankle bumpers minimize mechanical noise

Furthermore, the Hybrid III has a huge instrumentation capacity for accelerometers, load cells and displacement transducers. In Fig.2.15 all the instrumentation that can be mounted on the Hybrid III dummy is shown.

Location	Description	Channels
Head	3 Accelerometers in a Triax array, up to 15 Accelerometers	Ax, Ay, Az (used for HIC) 5X Ax, Ay, Az Head Rotation
Neck	Six-Axis Upper Neck Load Cell Six-Axis Lower Neck Load Cell	Fx, Fy, Fz, Mx, My, Mz Fx, Fy, Fz, Mx, My, Mz
Clavicle	Biaxial Load Cell (Left & Right)	Fx, Fz
Humerus	Four-Axis Load Cell (Left & Right)	Fx, Fy, Mx, My
Thorax	3 Accelerometers in a triaxial array Chest Displacement Transducer Four-Axis Rib/Spine Load Cell Five-Axis Thoracic Spine Load Cell	Ax, Ay, Az (Chest Accel) Dx (Std. Equipment) Fx, Fy, Fz, My Fx, Fy, Fz, Mx, My
Lumbar Spine	Three-Axis Lumbar Spine Load Cell	Fx, Fz, My
Pelvis	3 Accelerometers or Triax Pack Submarining Load Bolts	Ax, Ay, Az Fx (3 per side)
Femur	Uniaxial Femur Load Cell or Six-Axis Upper Femur Load Cell	Fx (per leg) Fx, Fy, Fz, Mx, My, Mz (per leg)
Knee	Knee Displacement	Dx (per knee)
Lower Legs*	Biaxial Knee Clevis Load Cells Four Axis Upper Tibia Load Cells Four Axis Lower Tibia Load Cells	Fz (per leg) Fx, Fz, Mx, My (per leg) Fx, Fy, Mx, My (per leg)
Ankle	Five-Axis Load Cell	Fx, Fy, Fz, Mx, My (per leg)
Toe	Toe Load Cell	Fz (per foot)

*Special four channel configurations are available in the upper & lower tibia load cells.

Figure 2.15: Hybrid III Instrumentation

In order to perform test on subjects with a different physique from the 50th percentile one, Humanetics created other dummies:

- 95^{th} percentile male dummy
- 5^{th} percentile female dummy
- ten, six and three year old dummies

Table 2.4 shows the anthropometric data of the mannequins previously listed.

[5] Anterior cruciate ligament

Hybrid Model	Anthropometric Data		
	Mass [kg]	Stature [m]	Total sitting height [m]
5^{th} percentil	49	1.4896	0.7874
50^{th} percentil	77.70	1.7458	0.8839
95^{th} percentil	101.15	1.8502	0.9347
3-year old	16.17	0.94488	0.5461
6-year old	23.4	1.1405	0.635
10-year old	35.2	1.2014	0.7239

Table 2.4: Anthropometric data for different Hybrid III models

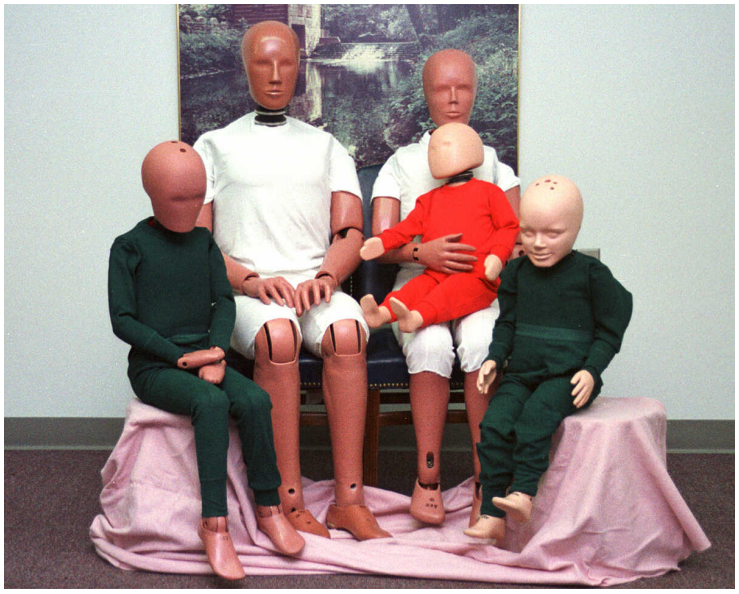

Figure 2.16: Hybrid III's family

In Fig.2.17 and in Fig.2.18 are represented the two most important assemblies exploded views for our work: the neck assembly and the head assembly.

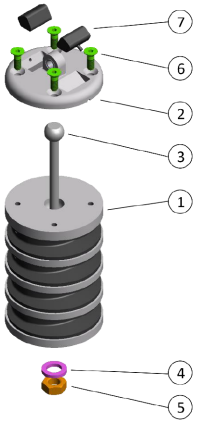

Item	Quantity	Part Number	Description
1	1	78051-336	Molded Neck Assembly
2	1	78051-297	Nodding Joint, Neck
3	1	78051-301	Cable - Neck
4	1	9008007	Washer, Flat 0.515 ID X 0.875 OD
5	1	9000018	Nut, Jam 12-20
6	4	9000447	Screw, FHCS 1/4-20 X 3/4
7	2	78051-351-8550	Nodding Blocks*

Figure 2.17: Neck assembly exploded view and parts list

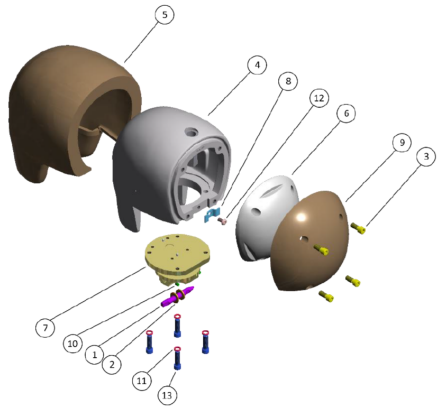

Item	Quantity	Part Number	Description
1	1	1717	Pivot Pin, Neck
2	2	78051-253	Washer, Nodding Joint
3	4	9000005	Screw, SHCS 1/4-20 x 5/8 LG. Nylok®
4	1	78051-77X	Skull, Machined, Six-Axis Neck
5	1	78051-228	Head Skin
6	1	78051-220	Skull Cap

Item	Quantity	Part Number	Description
7	1	78051-383X	Neck Transducer Assembly
8	1	83-5006-001	Skull Cable Clip
9	1	78051-229	Cap Skin, Molded
10	2	9000452	Screw, SSSCP #8-32 X 1/4 LG.
11	4	9000677	Shoulder Screw Shim, 1/4 X 1/16 Thick
12	1	9000538	Screw, BHCS #10-32 X 3/8 LG.
13	4	9000264	Screw, SHCS 1/4-28 X 7/8 LG.

Figure 2.18: Head assembly exploded view and parts list

2.3.5 Requirements for dummies

According to J.H.Marcus [29] that studied dummy and injury criteria for crashworthiness, ATDs must meet several requirements in order to be useful and convenient:

- *biofidelity*: ability to reproduce the behavior of the human body given different configurations, to estimate movements and forces involved and to provide compliant values, in terms of injury criteria.

- *repeatability*: ability to provide concordance between a series of measures, when the measurement conditions are left unchanged.

- *reproducibility*: ability to provide concordance between a series of measurements while varying one or more conditions (e.g. measuring instrument).

- *durability*: ability to survive test conditions without damage, opposite to what happens to human beings.

- *standard calibration*: as all measuring instruments, it is appropriate that the ATDs are subjected to periodic calibrations to ensure results accuracy. For many ATDs, calibration techniques are listed in the Code of Federal Regulations.

2.4 Finite Element Models

As we already said in Chapter1, experimental tests are expensive in term of both time and money because they are difficult to arrange and because they require expensive tools and instrumentation. Meanwhile, numerical simulation are becoming more and more fast and accurate thanks to the continuous improvement of calculators. The FE models themselves are more realistic and reliable than in the past and thus they allow to run less and less experimental tests in favor of the numerical ones. Moreover, they permit to analyze and visualize deformation, loads and energy in every node or element in the model during the entire simulation. On the other hand, it is necessary to use experimental tests as a reference for the validation of numerical models, especially when there are many components interacting with the dummy as in this work. In this study, two highly detailed FE models (provided by FIA) have been used: LSTC[6] Hybrid III DETAILED 50^{th} percentile and THUMS AM50v4.1 (50^{th} percentile).

2.4.1 Hybrid III: LSTC DETAILED model

In this thesis, the Hybrid III FE model that has been used was developed by LSTC and provided by FIA. The Model is distributed free of charge to licensees of LSTC's LS-DYNA software. It represents a male 50^{th} percentile occupant and it is 174 *cm* tall and weights 79 *kg*. The type of model is DETAILED, hence the model is very complex and detailed, indeed. It is formed by approximately 466000 elements and 280000 nodes, the articulation are modeled as joints and several contact card manage the contact between subsystems. The articulation allows limb movements with RoMs similar to the real ones and can be managed during the pre-processing phase (PRIMER has been used as pre-processor software for this work). Thus, it is possible to position the dummy without running simulations. To model all the different dummy's materials, more than 250 structural material cards are defined.

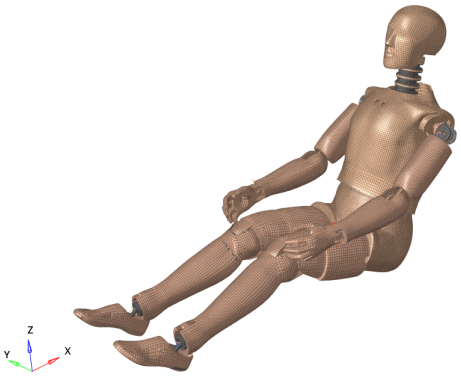

Figure 2.19: LSTC Hybrid III finite element model

[6]Livermore Software Technology Corporation

2.4.2 Total Human Model for Safety

Total Human Model for Safety (THUMS) is a human FE model jointly developed by Toyota Motor Corporation and Toyota Central R&D Labs., Inc. The model aims to simulate human body kinematics and injury responses in car crashes. The geometries of the human body parts are represented by FE meshes and their material properties are defined assuming constitutive laws. There are versions and variations in THUMS.

THUMS has been upgraded a few times. The models are (were) commercially available. The first version (Version 1) was completed in 2000. The major bones and ligaments were modeled in Version 1, but the brain and the internal organs were simplified as solid parts. Joint motions were simulated as relative motion between bones without using kinematic joint elements equipped in the FE code. The total number of elements was around 80,000 with an average mesh size of 15 mm. The model aimed to simulate bony fractures and ligament ruptures in car crashes. The second version (Version 2) was generated in 2004, modifying the facial bone parts to simulate fracture. The third version (Version 3) was available from 2008. A detailed brain model was newly introduced for simulating brain injury. The total number of elements was around 130,000. The forth version (Version 4) was completed in 2010. The model has internal organ parts to simulate their injuries. The total number of elements is around 2,000,000. The fifth version (Version 5) was completed in 2015. The model incorporated shoulders, thoracic and lumbar spines, internal organs, and the whole body muscles into the THUMS Version 3. The total number of elements is around 280,000. The sixth version (Version 6) is the latest model completed in 2019. The model incorporated the whole body muscles into the THUMS Version 4. The total number of elements is around 2,000,000. [46]

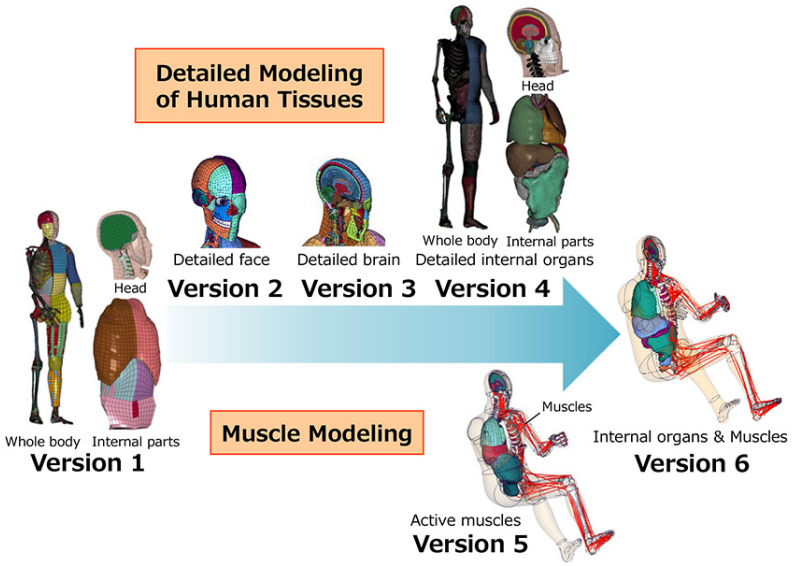

Figure 2.20: Evolution of THUMS.

THUMS was validated against loading tests both to body components and whole body. A total of 38 tests with postmortem human subjects (PMHS) were cited from the literature [9]. The aim was to create a tool that could go above and beyond what was possible with vehicle collision tests. Virtual HBM are indeed intrinsically more accurate than ATDs. The latter are limited in how accurately they can represent a human body because they are designed to be durable as seen in Section2.3.5. The concept is to precisely represent the human body without geometrical simplification. The internal torso structure was digitized in cooperation with the University of Michigan, which holds large quantities of data obtained using high-resolution CT scans. The data was utilized for FE modeling. A data-set of a 39-year old male with a height of 173 *cm*, a weight of 77.3 *kg*, and a BMI of 25.8 was selected for the AM50 model. The scanned data was converted into Standard Triangulated Language (STL) format polygons for each body and tissue part. Tissue parts were identified by applying a masking process to the CT scan images and adjusting the threshold value. The following organs were converted into polygon data: heart, lungs, liver, kidneys, spleen, pancreas, gall bladder, bladder, esophagus, stomach, duodenum, small intestine, and large intestine. The geometries of the major arteries, veins, and the membrane tissues surrounding the organs, such as the diaphragm, pleurae, peritoneum, and fascia, were also extracted. Separate polygon data was also generated for visceral fat. The scanned data only included the torso part. The geometries of the head and the extremities were defined based on Version 3 but were refined for finer mesh. Surfaces were created from the polygon data for meshing. [46]

For what concern the materials, skeletal parts were assumed to have elasto-plastic properties. Hyperelastic material was assumed for soft tissues. Ligaments and tendons generally have low stiffness for small elongation but show high stiffness for large elongation. Solid organs such as the liver and kidney have incompressive mechanical properties. The hyperelastic material model well simulates the mechanical behavior of such soft tissues. Skin and flesh parts are also represented by the hyperelastic materials. Hollow organs such as the lung and intestines have compressive mechanical properties. Low density foam materials were assumed for such parts. The heart is a hollow organ but has thick muscular walls and blood inside. The mechanical property of the heart is very incompressive. The property data input into each material model was selected from the literature data. [46]

The most important part for our work is the Thorax Model. It includes all the skeletal parts and the major soft tissues. Figure 2.21 shows the skeletal parts including the neck. The included hard tissues are; ribs, sternum, spine (vertebrae), clavicles, scapulas, sacrum and pelvis. The connective tissues such as costal cartilages, intervertebral discs, pubic symphysis and ligaments are also modeled. The cortical bones in the torso are modeled with shell elements as their thickness is around 1 *mm* or thinner, while the trabecular bones are modeled with solid elements. Solid elements are also used to model costal cartilages, intervertebral discs and pubic symphysis. Shell elements are used for the ligaments. Nodes at boundary surfaces between connective tissue are shared (e.g. cortical and trabecular bones,

rib cartilage and costal bones). All the parts are deformable. The bones are assumed to be elastic viscoplastic, while foam type materials are assumed for the intervertebral discs and the pubic symphysis.

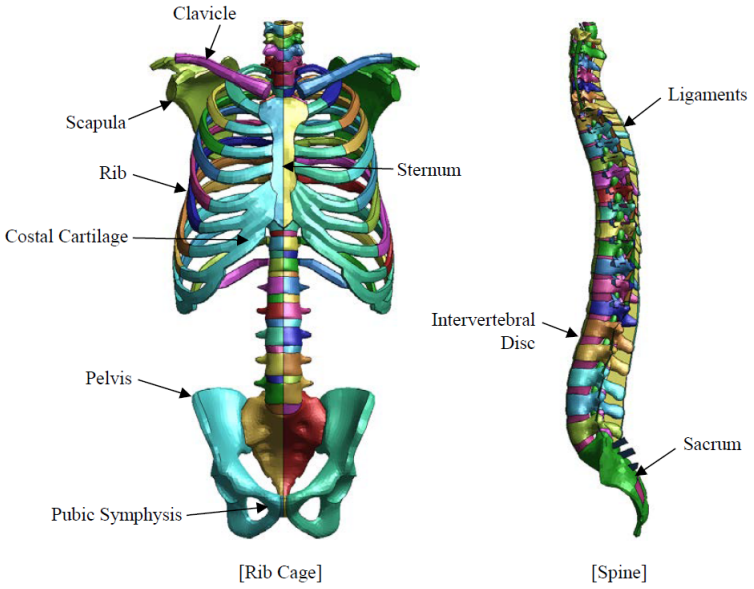

Figure 2.21: Skeletal Parts in Torso Model (with Neck Model).

Finally, the whole body model was generated by integrating all the component models (head/brain, neck, shoulder and upper extremity, thorax and spine, hip and lower extremity, and internal organs). Skeletal muscles of the whole body except the head and face were modeled with their corresponding tendons, and were attached to the whole body model (Figure 2.22). The muscle-tendon complex was modeled by using truss elements with a Hill type muscle material (LS-DYNA MAT156: MAT_MUSCLE) and seatbelt elements with a tension-only nonlinear elastic material (LS-DYNA MAT_B01: MAT_SEATBELT). Whole body includes 262 skeletal muscles. This muscle model consists of 808 parts for muscle elements and 80 parts for seatbelt elements. The number of elements was 3,336 (1,224 for beams, 2,066 for seatbelts, and 46 for shells). Mass of the whole muscle model was around 0.97 *kg*. *[46]*

The THUMS used in this work was provided by FIA and is a version 4.1. It is 177 *cm* high and it weighs 74 *kg*. As seen, this model is more complex than the Hybrid III: LSTC DETAILED model, hence it is easy to comprehend that the numerical simulations are heavier and require better calculators.

The positioning was performed in order to fit the THUMS into the seat. This process was more complex than Hybrid III positioning because THUMS has no tools for moving in the pre-processor environment. The positioning has been done though numerical analysis and is described later.

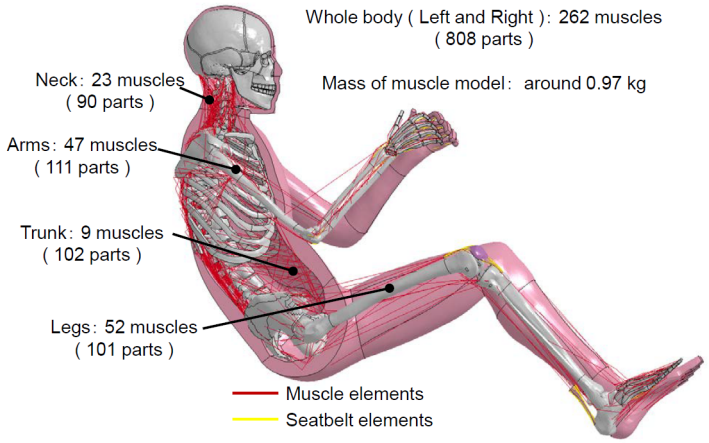

Figure 2.22: THUMS Muscle Lines.

2.5 Cervical spine anatomy

The vertebral column forms the central pillar of the human body and is divided into 24 mobile vertebrae (cervical, thoracic and lumbar) and a group of nine fused sacro-coccygeal vertebrae (pelvic). Its equilibrium is conditioned by the presence of vertebral curvatures which are similar to an S shape. In the sagittal plane, these curvatures are four in number: cervical curvature in lordosis, thoracic curvature in kyphosis, lumbar curvature in lordosis and sacrococcygeal curvature in kyphosis. According to the previous studies [36], these curves make it possible to absorb the mechanical stresses due to the movements of the body. The spine can support loads up to 6000 *N*. Regarding structure organization, the spine also has a protective function for the spinal cord and spinal nerves. The connection between the skull and the rest of the spine is made by the cervical spine which supports the head and allows its mobility. In the same way as the rest of the vertebral column, the cervical spine consists of vertebrae, ligaments, intervertebral discs and the nervous system.

2.5.1 Cervical spine bone structures

The cervical spine is the most superior portion of the vertebral column and it lies between the skull and the thoracic spine. It consists of seven distinct vertebrae (C1 to C7[7]).

Two of the cervical vertebrae have unique names: C1 is called *atlas* and C2 is called *axis* [1]. The atlas is the first cervical vertebra and articulates with the occiput of the head and the axis. It differs from the other cervical vertebrae in that it has no vertebral body and no spinous process. It's important to highlight the position of the occipital condyle, that is positioned on the occiput because it is essential for the definition of N_{ij} as seen in Section 2.2.1. It is shown in Figure 2.25.

The axis (C2) is easily identifiable due to its dens (odontoid process) which extends

[7]The name of the cervical vertebrae is given by the letter "C" that stand for "cervical" and by the number of their position starting from the one nearest to the cranium

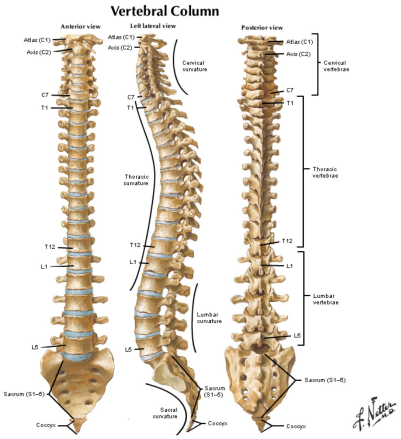

Figure 2.23: Human vertebral column with its curvatures in anterior view, left lateral and posterior view

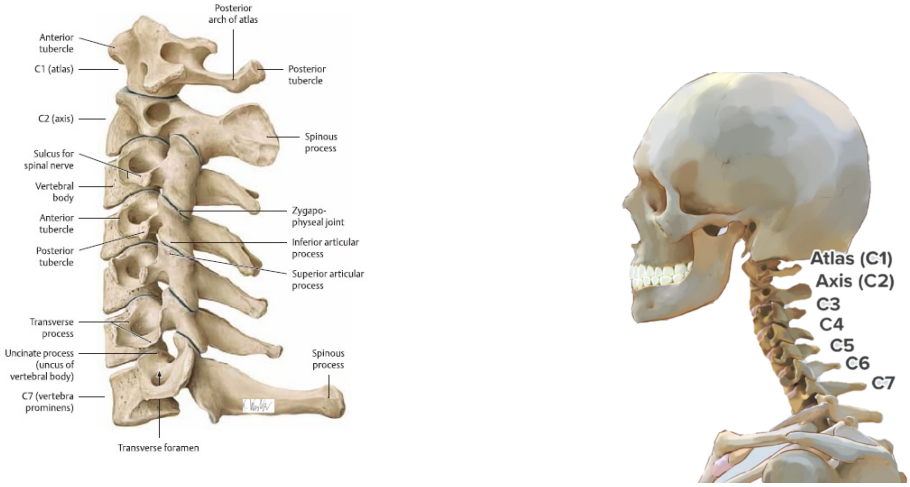

Figure 2.24: Anatomy of the cervical spine

upwards from the anterior portion of the vertebra. The dens articulates with the anterior arch of the atlas and it creates the medial atlanto-axial joint. This joint allow the rotation of the head independently from the torso.

The vertebrae C3 to C7 have similar geometry and composition. The vertebral body is made of cancellous bone covered with cortical bone. This composition allows to carry compression loads. The spinous process and the transverse processes serve as points of intersection and leverage for muscles and ligaments. The spinal cord is located in the spinal canal. The articular facets guide the movements between two consecutive vertebrae.

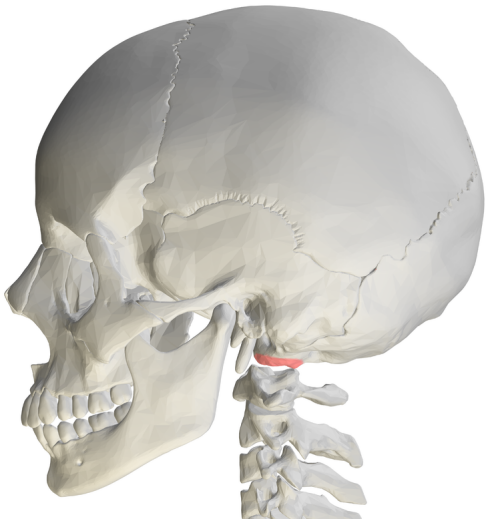

Figure 2.25: Occipital condyle highlighted in red

2.5.2 Ligaments

The mobility and stability of the spine are provided by the spinal ligaments made of bands of fibrous tissue [1]. The posterior longitudinal ligament (PLL) and the anterior longitudinal ligament (ALL) provide the connection between the vertebral bodies and limit movements in flexion and extension. The yellow ligaments or ligamentum flavum (LF), interspinous (ISL), nuchal (NL), which becomes the supraspinous ligament below the C7 level, and capsular (CL) protect the spinal cord and limit many movements (flexion, extension, tension, translation rotation). The transverse ligaments are linked to the inner part of the atlas (C1) and around the odontoid process of the axis (C2).

2.5.3 Intervertebral discs

The intervertebral discs, located between each of the vertebrae, allow the vertebrae to be held together. These discs also allow movement between each of the vertebrae as well as shock absorption and load transfer between two vertebrae. There are 23 intervertebral discs in total. Each disc consists of a ring of fibrous cartilage with a gelatinous nucleus (80% water) in the center. This core provides the disc with elasticity and compressibility while the ring limits movement and expansion of the core [15].

2.5.4 Spinal cord and nervous system

The spinal cord is an integral part of the central nervous system (CNS). Its shape is similar to a cylinder about 1 *cm* in diameter and 45 *cm* in length. Its main function is to transmit electrical signals between the central nervous system and the different parts of the body. The spinal cord passes through the spinal canal and is protected by the vertebral column. Its morphology is not constant on the transverse plane and shows the emergence

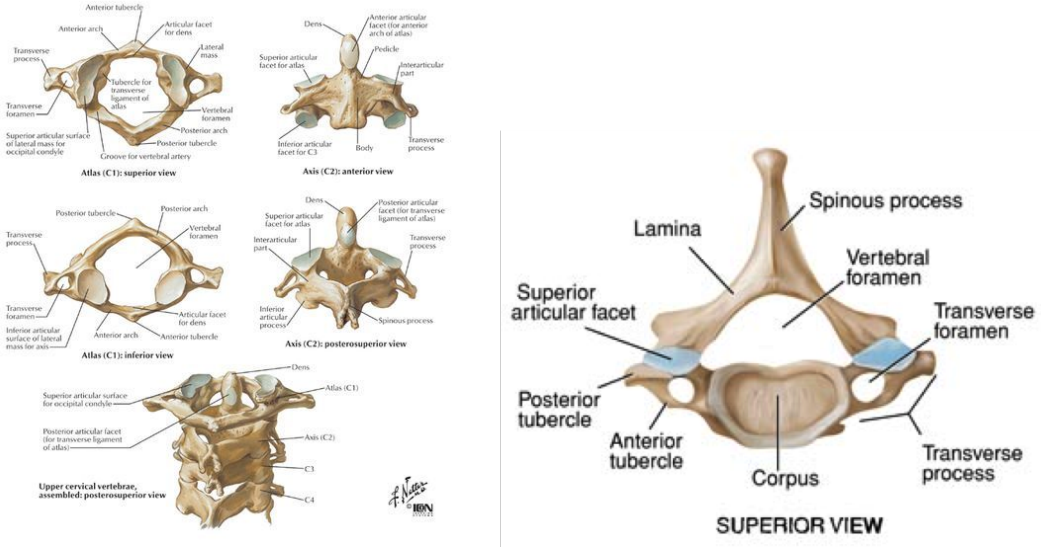

(a) C1 (atlas), C2 (axis) and upper segment C1-C4 (b) Top view of C7

Figure 2.26: Anatomy of cervical vertebra

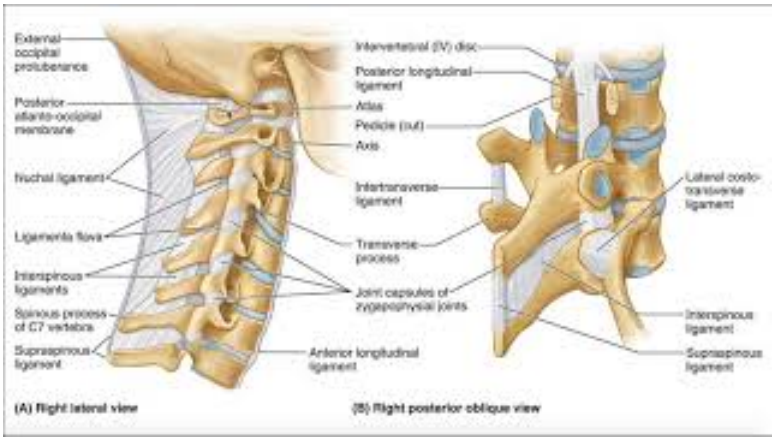

Figure 2.27: Principal ligaments of the cervical spine

of 31 pairs of spinal nerves which are subdivided into 8 cervical nerves, 12 dorsal nerves, 5 lumbar nerves, 5 sacral nerves and a coccygeal nerve. The vertebral levels are associated with different functions. For example, breathing and the movements of the head and neck are managed at levels C1-C4, the heartbeat and movement of the shoulders are provided by levels C4-C6 [15].

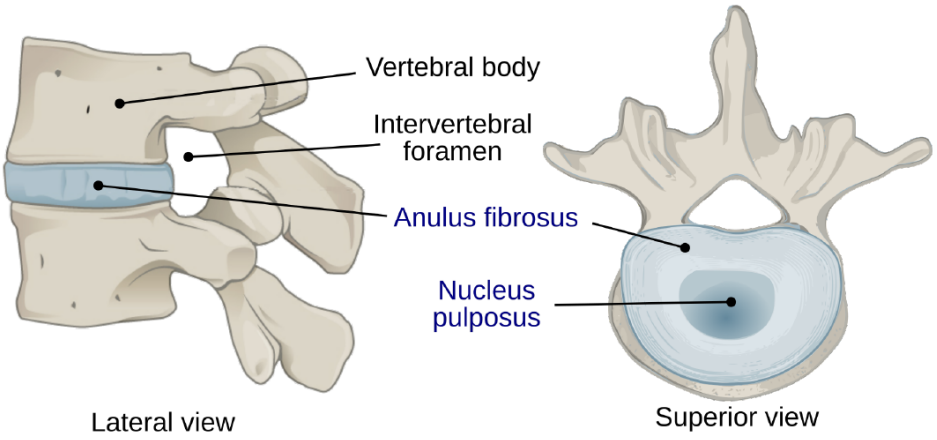

Figure 2.28: Lateral and superior views of IVDs

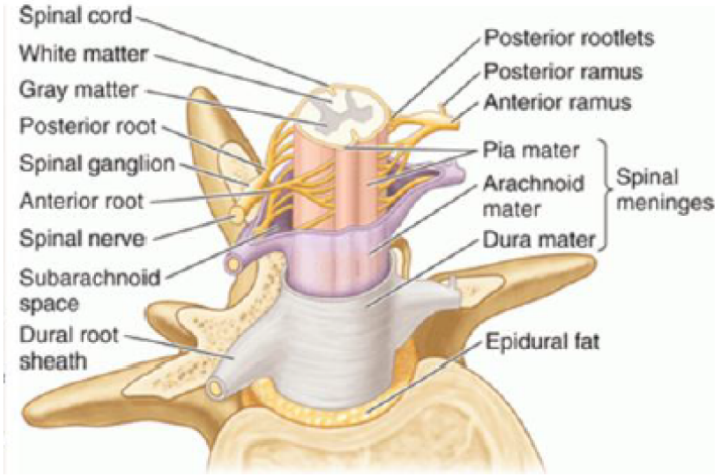

Figure 2.29: Spinal cord and nervous system

Chapter 3

Experimental tests

This chapter describes the planning and the results of the frontal impact experimental testing campaign with the Hybrid III ATD. In particular, the place, the sled seat manufacturing, the choice of the crash pulse, the instrumentation, devices and setups used are explained. Then the obtained experimental data are discussed and compared.

3.1 La.S.T - TRANSPORT SAFETY LABORATORY

In the La.S.T. - TRANSPORT SAFETY LAB of the Politecnico di Milano's Aerospace Science and Technology Department, we work on researching passive safety, which has to do with any engineering activities that can be implemented to reduce the risk of injury for the occupants of any kind of vehicle. Passive safety has been studied at the Politecnico since the late 1960s, starting with the activities of Professor Giavotto, the founder of this laboratory, which is undoubtedly a one-of-a-kind facility, not only in Italy but also internationally.

3.1.1 The laboratory sled

In order to perform our frontal impact experimental testing campaign, we used the horizontal sled available in the laboratory. This is typically used for tests aimed at assessing the energy absorption capabilities of the crushable components and the structural integrity of those which undergo the inertial loads due to the sled's deceleration.

The sled goes on two cylindrical rails with four wheels, towed by a pneumatic system whose pressure can be set by a compressor depending on the speed that we want to reach before the impact. In fact, the first part of the run is the acceleration phase in which the sled is towed, and then in the last 6 m the sled goes at constant velocity. The speed is measured at the entrance of the constant velocity phase using photocells. Finally it impacts on several tubes mounted on a big rigid wall, causing the deceleration. Depending on the material, size and number of tubes, together with the choice of the impact velocity, the crash pulse can be modified as described in Section 3.2 .

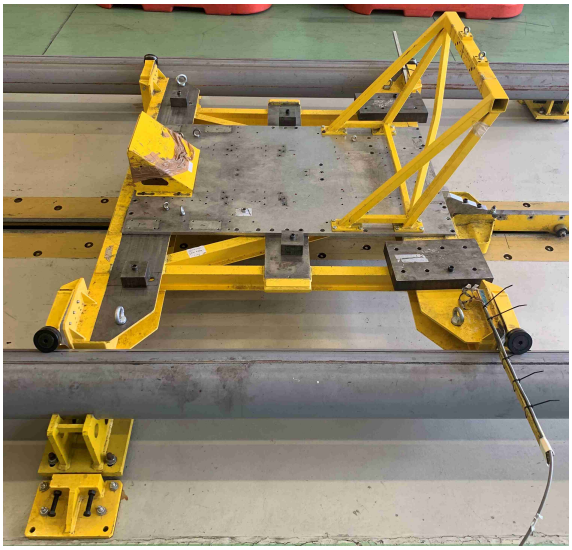

Figure 3.1: The sled mounted on the two cylindrical rails

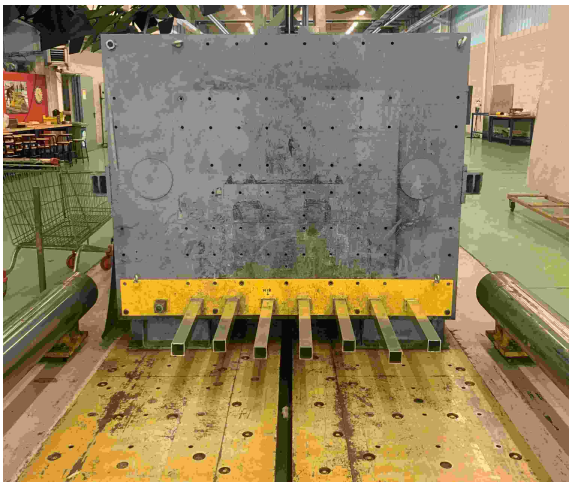

Figure 3.2: The crash tubes mounted on the rigid wall

The main feature of this setup is the big length of the cylindrical rails. In the past, the building used to be part of the 'Ceretti & Tanfani' facility, and it was the building where the cables were weaved, and that is why the vast size of the factory made it possible to set up this type of horizontal sled in the laboratory. The advantage of having this long run is that we can reach the chosen impact velocity without a big initial acceleration that can cause unwanted movements, for example of the dummy or of other components that must reach the impact in a particular position.

3.1.2 The sled seat

To correctly seat the dummy we had to find a sled seat that could satisfy these requirements:

- dimensions compatible with those of the Hybrid III and of the horizontal sled.

- reproduce a reclined seat (around 30°) or an extreme reclined seat (around 40°), that are the typically seats used in the categories where the FHR are used.

- easy to make the FE model.

- enough stiff to withstand multiple tests.

- that allows to make some changes.

In the laboratory we found an old sled seat, used few years ago for the same purpose.

Figure 3.3: The sled seat before any modification

Since it had already been used for the same purpose, the dimensions were perfectly compatible with both the dummy and the sled. We made some dummy positioning tests, to check that the dummy could reach a correct position and to take some measures and reference points to be as realistic as possible during the Hybrid III FE model positioning (Fig.3.5).

Figure 3.4: Dummy positioning tests

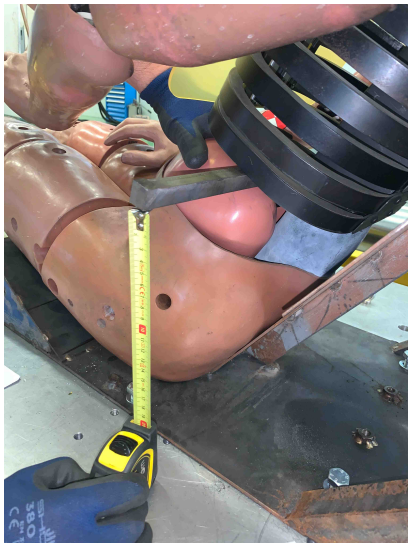

Figure 3.5: Dummy measurements and reference points

Also the attachments for the safety seatbelts were previously done, but they have been modified considering the FIA guidelines described in Section 3.4.2. All the welds have been verified, to make sure of its capacity to withstand high loads caused by the deceleration.
The inclination of the sled seat is 36°, so between the two allowable limits, and it weighs 36.5 *kg*.
Its geometry is really simple, so it was easy to make the FE model with shell elements as described in Chapter 4.1.1. To maintain this simplicity we decided not to use any seat foam and headrest. This thanks to the low acceleration that the dummy undergoes in the first phase of the tests, as described in Section 3.1.1, that can't get its head moving from the

initial position. In the end, the seat sled has been repainted.

3.2 Crash Pulse

Crash pulse is the acceleration curve measured in the car or in the sled during a crash test. The shape, time duration, and maximum acceleration of crash pulse affect the predicted motion of the occupants. We measured it through two accelerometers, to be sure of the measurement, mounted on the horizontal sled. After processing the data, the acceleration profiles have been used in the FEA to perfectly reproduce the experimental tests.
To choose the best crash pulse for our work, we considered three main factors:

1. the SFI SPECIFICATION 38.1
2. the FIA Frontal Crash Pulse Lower Limit
3. numerical errors of the THUMS model

Starting from the first, we decided to follow the SFI SPECIFICATION 38.1 [27] for what concern the crash pulse. This specification establishes uniform test procedures and minimum standards for evaluating and determining performance capabilities for Head and Neck Restraint Systems used by individuals engaged in competitive motorsports. It says that the system shall be tested using a 50^{th} percentile male Hybrid III ATD seated and restrained in a pan type seat assembly with an SFI Specification 16.1 six-point driver restraint system, mounted to a conventional race car style mounting frame without steering wheel and steering column. The test sled shall be capable of propelling the entire assembly in a manner to achieve a pulse contour as in Fig.3.6, producing a nominal 68 g peak.

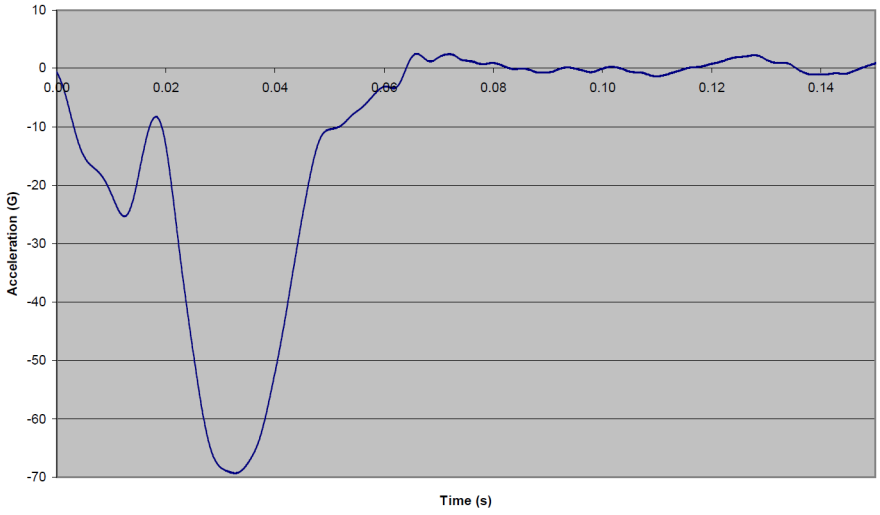

Figure 3.6: SFI SPECIFICATION 38.1 crash pulse

Following this specification, we were over the FIA Frontal Crash Pulse Lower Limit in Fig.3.7 , but we were not sure about the problems that the THUMS model could give at

this high value of deceleration. From our experience, due to the complexity of the THUMS model, we knew that with a crash pulse peak around 70 g the model gives numerical errors like LS-Dyna *Error 40509 - negative volume in solid element.*

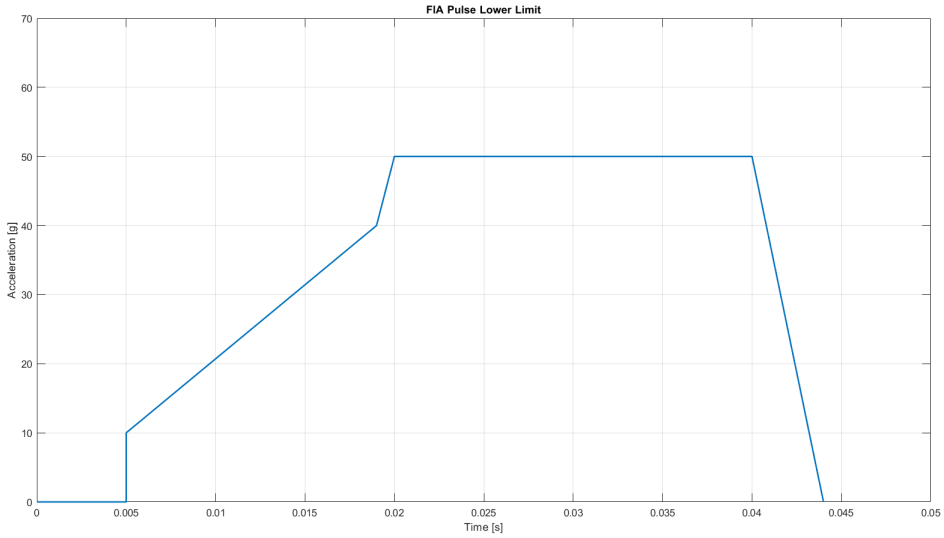

Figure 3.7: FIA Frontal Crash Pulse Lower Limit

To verify this problem, we made the decision to perform some simple frontal crash tests with only the horizontal sled and after having processed the accelerometers data, used them inside the THUMS model to see if it created numerical errors.

Since these tests were performed with only the horizontal sled, in Fig. 3.1, some mass was added to reproduce the real total weight of the sled with also the sled seat, the Hybrid III dummy and all the devices. So two masses of 48 kg and four masses of 4 kg have been added, to reach the final total weight of 717 kg.

The decision of the crash tube's number and properties were made by the laboratory's technicians. Given our deceleration peak target of 68 g and the total mass of the sled, based on experience and on a spreadsheet they could give us all the information about the tubes and the impact velocity.

3.2.1 First Crash Pulse Test

For the first crash pulse test, the technicians decided to use eight square tubes 60 x 60 mm and 3 mm thick, made of *6082 Aluminum alloy.* The length was not the same for all the crash tubes, in order to have a more gradual deceleration of the sled during the impact (Fig.3.8a). The longest tube was 640 mm and then for each tube the length decreased of 20 mm, so the shorter one was 500 mm long. Furthermore, in the front section of the tubes, four small cuts have been done to make the crash tubes deform in the correct way (Fig.3.8b)

The target impact velocity has been fixed at 50 $\frac{km}{h}$, and to reach it the compressor's pressure was 7.6 *bar.* The real measured impact velocity was 48.54 $\frac{km}{h}$. The row acceleration

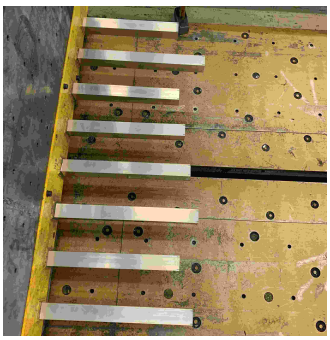

(a) The eight crash tubes with different lengths

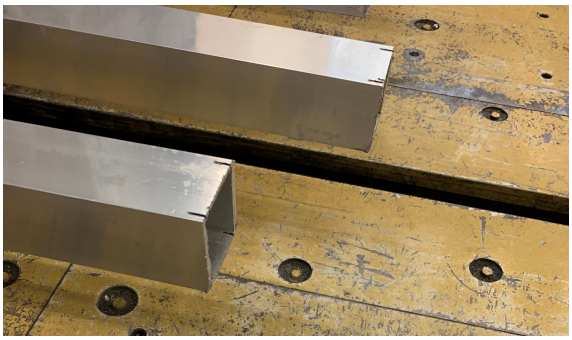

(b) Crash tubes front small cuts

Figure 3.8: The Aluminum crash tubes used in the First Crash Pulse Test

data have been filtered, as described in Appendix B, with a CFC60 filter and the results are reported in Fig.3.9.

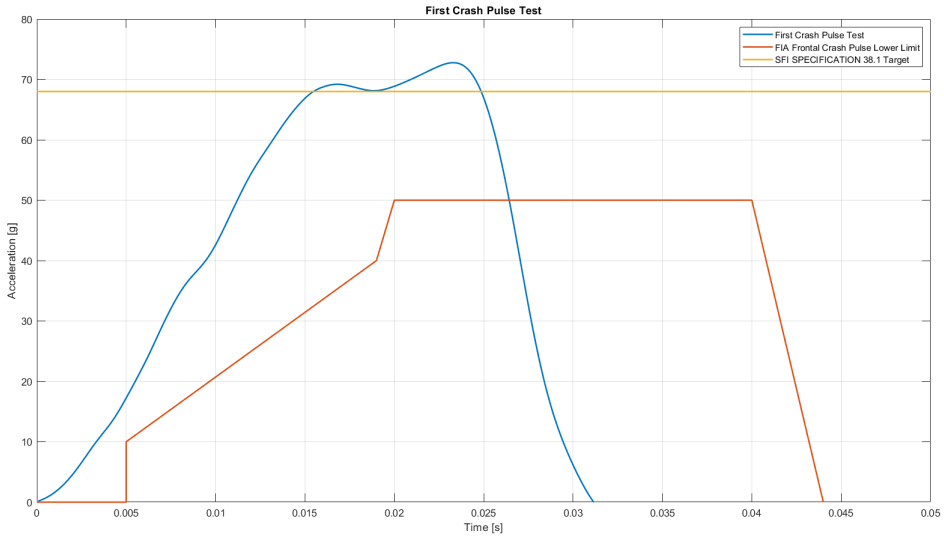

Figure 3.9: First Crash Pulse Test

Together with the experimental data of this first test, also the FIA Frontal Crash Pulse Lower Limit and the peak value of 68 g given by the SFI SPECIFICATION 38.1 have been plotted. We can see that our peak value is 73 g, so higher than the FIA Lower Limit and near the 68 g given by the SFI. The duration of the crash pulse is slightly smaller, but it is acceptable.

However, using this curve data as crash pulse inside the FEA of the THUMS model, it gave us the numerical problems that we mentioned in the previous Section3.2. So the goal of the Second Crash Pulse Test was to slightly decrease the peak, remaining in the range of 65 g - 70 g.

3.2.2 Second Crash Pulse Test

To reduce the deceleration peak, the technicians decided to reduce the number of tubes to seven, maintaining all the other tube's variables unchanged (Fig.3.2). The longest tube was again 640 *mm* but in this case the shorter one was 520 *mm* long. Since in the first test also the impact velocity was below the target, the compressor's pressure has been increased to 7.7 *bar.*

The real measured impact velocity in this case was 49.94 $\frac{km}{h}$. In Fig.3.10 the filtered acceleration data of the second test are showed, with always the FIA Frontal Crash Pulse Lower Limit and the peak value of 68 *g* given by the SFI SPECIFICATION 38.1.

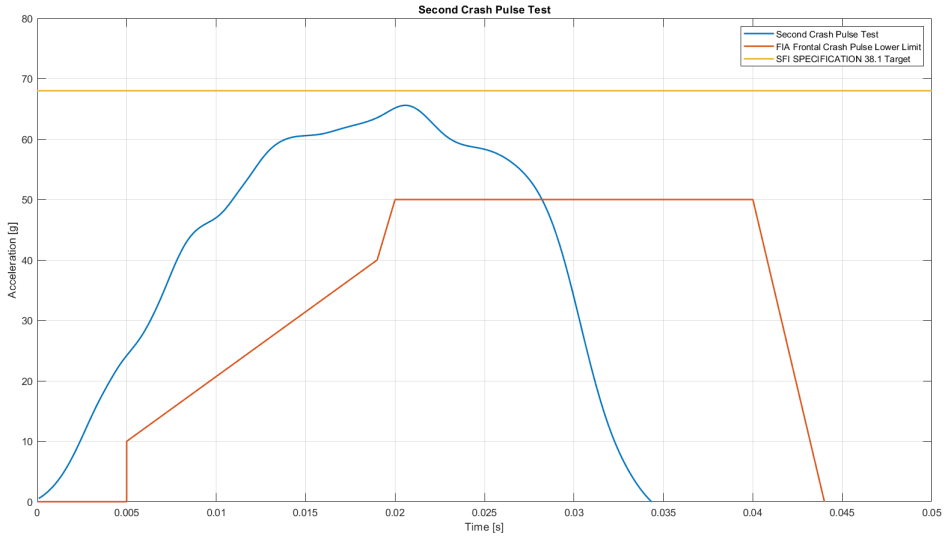

Figure 3.10: Second Crash Pulse Test

Compared to the first test, the peak decreased and the duration increased. We can see that the new peak is 66 *g*, so below the SFI's peak, but considering the variability of the experimental tests this result is acceptable. Using this crash pulse in the FEA of the THUMS model, the analysis finished without any problems. Due to this result, it was decided to use this setup for all the frontal impact experimental testing campaign with the Hybrid III ATD.

The final crash tubes setup was composed by seven square tubes 60 x 60 *mm* and 3 *mm* thick, made of *6082 Aluminum alloy* and with the length starting from 640 *mm* and then for each tube the length decreased of 20 *mm,* so the shorter one was 520 *mm* long. The final compressor pressure was set to 7.7 *bar.*

3.3 Hybrid III ATD and instrumentation

The Anthropomorphic Test Device used for this experimental testing campaign is the Hybrid III 50th Percentile Male Crash Test Dummy. The overall dimensions of the dummy are 782.2 x 429.3 x 1325.9 *mm,* with a seated height of 883.9 *mm* and a total weight of 77.7 *kg* [24].

Before the tests, all the verification guidelines and procedures given by the *Humanetics Hybrid III-50M User Manual [23]* have been followed. Particular attention was given to the joints of the Hybrid III dummies, that were adjusted to a "1 *g* suspended setting." This is defined as a torque level on the joint where the friction will allow an assembly to move toward the earth when a small force is applied to the unsupported end of the assembly. For example, when the dummy's arm is fully extended laterally so it is perpendicular to the body, the shoulder yoke clevis bolt should be tight enough to support the weight of the arm, but loose enough so when you tap the dummy's wrist, the whole arm will slowly fall towards the dummy.

During the crash tests the feet were constrained to the footrest with a ratcheting strap, to avoid or at least decrease the legs movement. In this way we also simplified the modeling of the feet-footrest interaction in the FEA. Also the arms have been constrained with a ratcheting strap to the dummy's torso, because due to the high level of deceleration peak we were afraid that the arms' joints could be damaged.

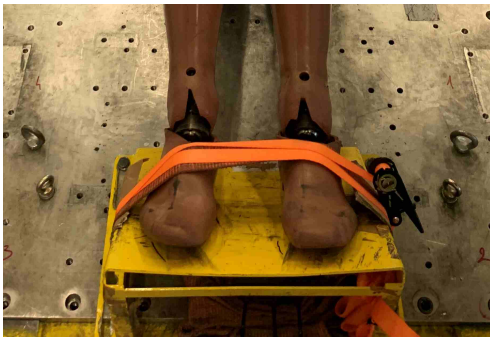

(a) Feet constrained to the footrest with a ratcheting strap

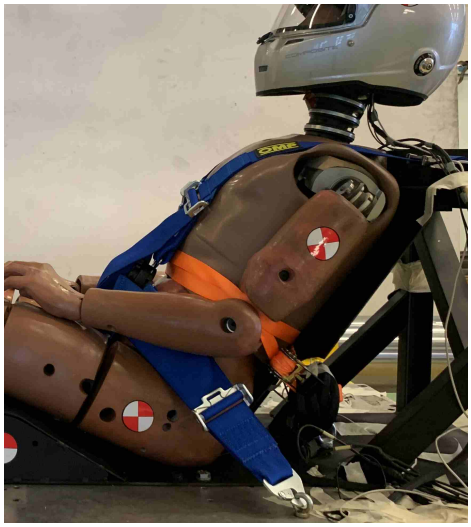

(b) Arms constrained with a ratcheting strap to the dummy's torso

Figure 3.11: Experimental tests dummy constraints

The measurements we were interested in were the neck forces and moments, and the head accelerations. So we installed a six channel neck loadcell and three accelerometers inside the head.

3.3.1 Neck loadcell

For the neck forces and moments we used the *First Technology Safety Systems® HYB. III, SIX CHANNEL UPPER NECK LOADCELL, IF-205.*

By definition, loadcell is a type of transducer, specifically a force transducer. It converts an input mechanical force such as load, moment, or pressure into another physical variable,

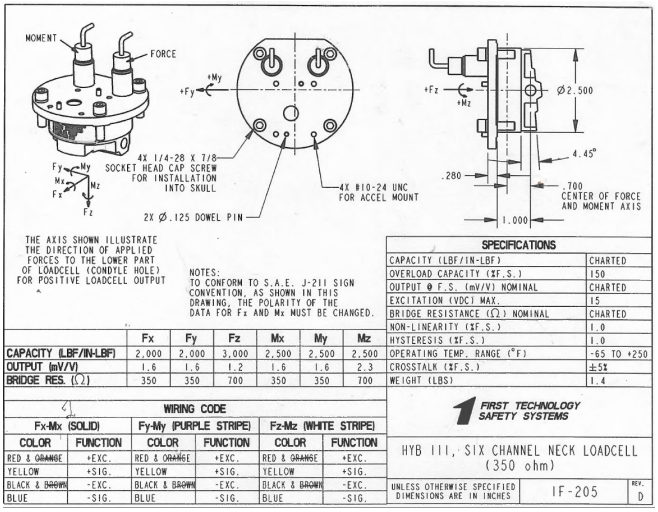

Figure 3.12: *First Technology Safety Systems® HYB. III, SIX CHANNEL UPPER NECK LOADCELL, IF-205*

in this case, into an electrical output signal that can be measured, converted and standardized. As the force applied to the force sensor increases, the electrical signal changes proportionally. The applied force causes compression or strain of the neck loadcell base body. This deformation is measured using strain gauges. Metal foil strain gauge is a material whose electrical resistance varies with applied force. In other words, it converts the applied neck forces and moments into a change in electrical resistance, which can then be measured.

Figure 3.13: The Neck Loadcell mounted

The neck forces and moments are calibrated with two rubber nodding blocks (N°7 in Fig.2.17), mounted on the top of the neck assembly, on the Nodding Joint (N°2 in Fig.2.17). The nodding blocks must not be worn out and must conform the installation angles showed in Fig.3.14a.

To perfectly calibrate the loadcell installation, we slowly increased the compression on the neck until the pivot pin (N°1 in Fig.2.18) can be pushed or lightly tapped in with a

minimum of effort (Fig.3.14b).

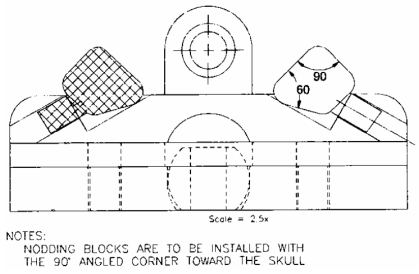

(a) Nodding blocks angles

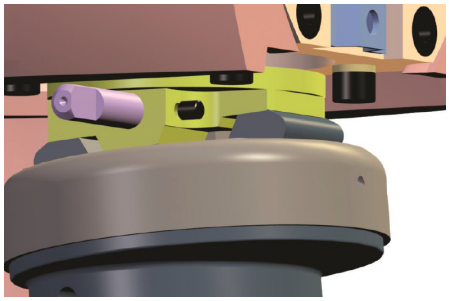

(b) Installing the neck pivot pin

Figure 3.14: Neck Loadcell details

Since the last Neck Loadcell Certification of Calibration was from 2008, we made some tests to check its correct functioning and the correct positive loadcell output directions. We applied loads in the three axis directions with a dynamometer, and we checked that the neck loadcell measurements were in the same magnitude of the dynamometer value.

To check the correct positive loadcell output for forces and moments, we simulated the positive and negative forces moving the dummy's head back and forth in all the three directions. Looking at the neck loadcell's resulting measurements in real time, we found the positive directions for forces and moments illustrated in Fig.3.15. For what concern the two most important data for us, so the neck axial force F_z and the M_y bending moment, we have considered positive the axial traction force and the flexion bending moment (Fig.2.10).

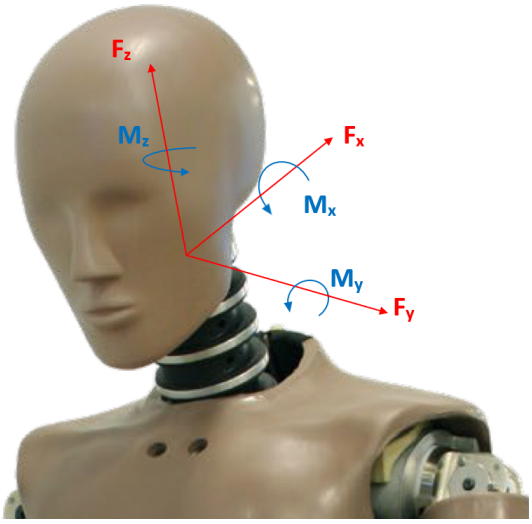

Figure 3.15: Positive directions for Hybrid III neck forces and moments

3.3.2 Head accelerometers

The head accelerations are another important data to evaluate the head injury. For example, the Head Injury Criterion One is one of the most adopted methods to measure the injury level in an impact. It has been introduced to measure the head injury from an impact in a crash situation, used to predict skull fractures and brain contusions and it is evaluated considering the accelerations along the three axis measured from the accelerometers in the center of mass of the dummy's head. Since in this work we don't have an head impact during the crash, we didn't evaluate this injury criterion, but the accelerations data have been sampled anyway to better understand the behavior of the dummy.

The three accelerometers were installed on the appropriate center mount cube, mounted on the top of the neck loadcell (Fig.3.16). Also in this case we checked the correct positive accelerometers output in the three directions and the results are showed in Fig.3.17.

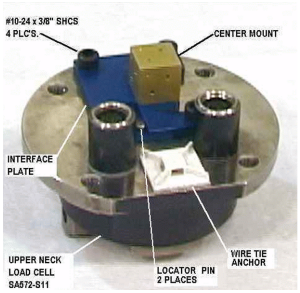

Figure 3.16: Head accelerometers center mount

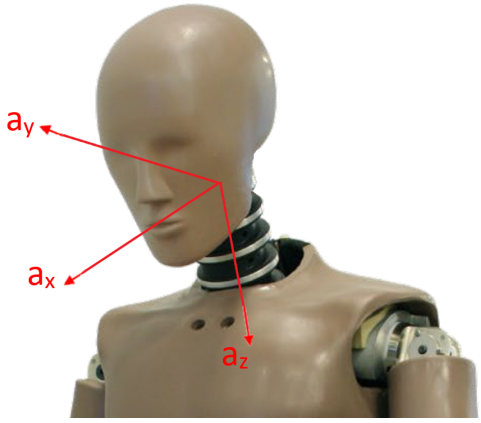

Figure 3.17: Positive directions for Hybrid III head accelerations

3.4 Safety equipment

In this section the safety devices used on the Hybrid III dummy during the experimental tests are described.

3.4.1 Helmet

The helmet used in the experimental tests was a Stilo® ST5FN COMPOSITE, homologated FIA 8859-2015 and conform to the HANS FIA 8858-10. Made of fiberglass – kevlar MSF (Multi Sandwich Fiber), it weighed 1556 *g*.

Figure 3.18: Helmet Stilo® ST5FN COMPOSITE

3.4.2 Safety harness

The safety harness was an OMP® six points safety harness, with 2"/3" shoulders straps, 3" lap straps and 2" crotch straps. Homologated FIA 8853-2016 for FHR use only.

Figure 3.19: OMP® six points safety harness

The safety harness' mounting points on the sled, have been done in order to respect the FIA installation angles (Fig.3.21). The mounting have been done with the threaded titanium eyebolts given by OMP®.

Other important data for our work, to check the correct modeling of the safety seatbelts in the FEA, were the seatbelt forces. The seatbelt loadcells available in the laboratory could fit only the 2" straps, so we decided to install a seatbelt loadcell on each shoulder strap. The loadcell is made of a metal body with two cylinders in which the belt is inserted. Also in

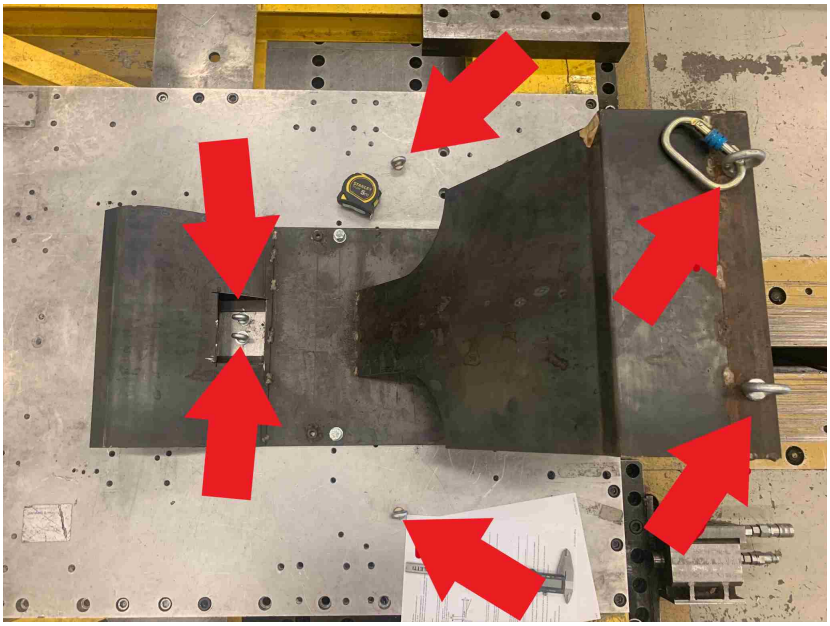

Figure 3.20: Safety harness' mounting points

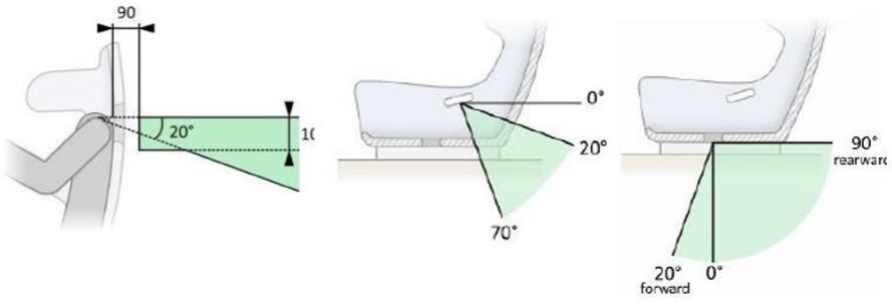

Figure 3.21: Safety harness FIA installation angles

this case, as for the neck loadcell (Section3.3.1), the operating principle is based on strain gauges. When the force is applied, the metal body acts as a "spring" and is slightly deformed, and unless it is overloaded, it returns to its original shape. As the body deforms, the strain gauge also changes its shape and consequently its electrical resistance, which creates a differential voltage variation through a Wheatstone Bridge circuit. Thus, the change in voltage is proportional to the physical force applied to the metal body by the seatbelt.

The safety harness were made of polyester fabric. To correctly model this material in the numerical models, displacement controlled tensile tests have been on any strap's type. The procedure and the results are showed in Appendix A.

3.4.3 HANS device

The Stand21® Ultimate FHR has been used as HANS device in our experimental tests. The all-carbon bodies of this model combine an exclusive resin-transfer technology (RTM

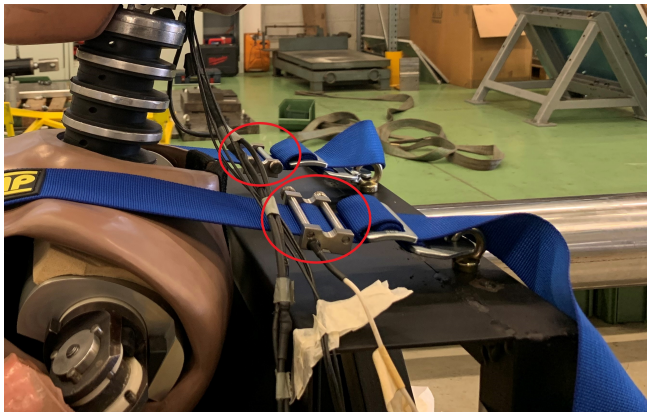

Figure 3.22: The seatbelt loadcells mounted

process) with a UD monolithic section. That refined monolithic technology has allowed a new design for the unit's arms. Their thickness is greatly reduced as well as their footprint to improve the fit between driver and harness. The arched top has been reengineered and redesigned in its whole, offering a reduction of its physical thickness to below 2 *mm*, allowing a reduction of helmet-to-seat (or headrest) space to improve safety. It is FIA 8858-2010 approved & SFI 38.1 certified [2]. The device has been supplied with the sliding tethers and padding. The surface of the HANS-yokes in contact with the harness belt has been provided by the manufacturer covered with a high friction rubber to grip the lower surface of the shoulder straps. The friction material has not been removed, and it has been monitored during the tests because no breakage, ripping, tears or other damage was acceptable.

Figure 3.23: Stand21® Ultimate FHR

Before the frontal crash test with the HANS device, we checked that that we were respecting all the guidelines on the aspects to take into account when using this FHR device for racing competitions given by the FIA document «*Guide and installation specification for HANS® devices in racing competition*» *[18].*

3.4.3.1 HANS® angles

The first one concerned about the HANS® angle. HANS® devices exist not only in different sizes but also with different angles between the yoke (part of the HANS® in contact with the driver's shoulders and chest) and collar (part of the HANS® located behind the driver's helmet). The specification says:

«When seated in racing position with its harnesses tightened, the HANS® collar angle must be between 60° and 90° from the horizontal (Fig.3.24a)».

In Fig.3.24b we can see the angle of our Stand21® Ultimate FHR, measured with a digital inclinometer, that is inside the allowed range.

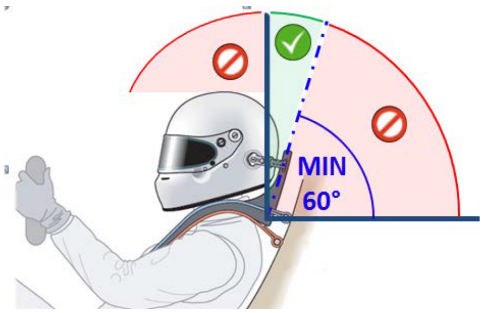

(a) Allowed collar angle

(b) Stand21® Ultimate FHR measured angle

Figure 3.24: Specification about the HANS® angle

There was not a rule that obliges the use of the padding between the device and the driver, so we decided to remove it to simplify the FE model of the HANS.

3.4.3.2 HANS tethers length

For what concern the tethers length, we did not have adjustable tethers but fixed length tethers. Therefore we had to make sure that the two tethers had the same length and then we measured the nominal length. The specification says:

«A nominal length is 150 mm. A tolerance of +/- 25 mm is acceptable. The nominal length shall be measured as following:

- *the driver shall be seated in the car in the normal driving position, wearing the HANS® and helmet and with the safety harness fastened;*
- *the driver should lean his/her body and head forward as far as possible - in this position the length must be measured from the leading edge of the HANS collar to the point of connection to the outside of the helmet.»*

Our measured nominal length was 164 *mm,* so inside the acceptable range.

3.4.3.3 HANS and Harness

The safetybelts to be used must be minimum 5 point harnesses homologated to FIA standard 8853/98 or 8853-2016. HANS® can be used with harness models that are homologated with the standard shoulder strap width of a minimum of 70 *mm*, as well as with models that are homologated with specific shoulder strap width of a minimum of 44 *mm* and that are marked "for FHR use only" or "for HANS use only", as in our case. (See our safety harness properties Sec.3.4.2).

If the length adjustment device of the shoulder belt is positioned on the HANS-yoke then the upper edge must be not more than 70 *mm* from the lower edge of the HANS-yoke as shown in Fig.3.25a. If the length adjustment device of the shoulder belt is positioned between the HANS-yoke and buckle, it must be lower than the HANS-yoke at least by 25 *mm*. This was our case, and the measured distance was 50 *mm* (Fig.*3.25b*).

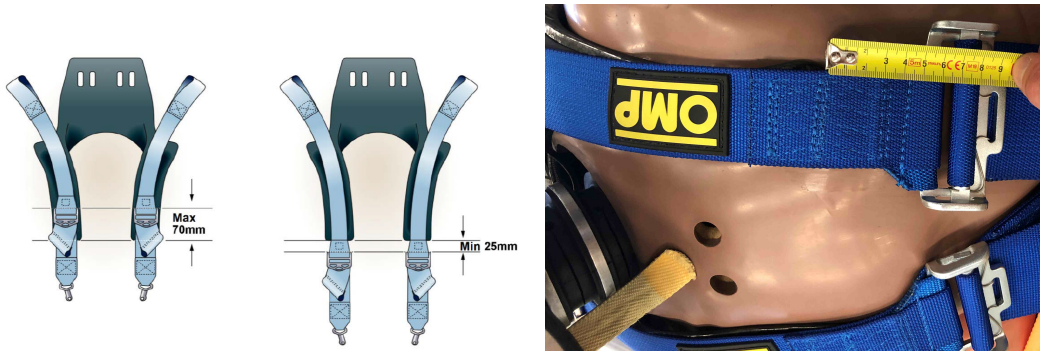

(a) Correct position of shoulder strap length adjustment device on HANS-yoke

(b) Measured distance of the length adjustment device from lower edge of the HANS-yoke

Figure 3.25: Safety harness requirements

3.4.4 Hybrid PRO device

For our work we used the Simpson Racing Hybrid Pro Lite®, that is SFI 38.1 certified & FIA 8858-2010 approved.

Also in this case, before the frontal crash test with the Hybrid PRO device, we checked that we were respecting all the guidelines on the aspects to take into account when using this FHR device for racing competitions given by the FIA document «*Guide and installation specification for Hybrid and Hybrid PRO devices in racing competition*» *[19].*

3.4.4.1 Hybrid PRO Tethers length Adjustment

The procedure given by the specification to adjust the tether assemblies is as follows:

«Once seated in racing position with the harnesses tightened, the rigid part of the Hybrid must be sitting on the shoulders between the driver's back and the seat and the shoulder belts should be on the belt bearing surface on the device. The rear tethers should adjusted

Figure 3.26: Simpson Racing Hybrid Pro Lite®

first. It is recommended to fit the tethers so that they will allow the wearer forward head movement in the range of 25 mm to 50 mm (Fig. 3.27), from the wearer's static or starting position. Always adjust the tethers on the right side of the restraint to the same length as the left side of the restraint. The front tethers should be adjusted next.»

To measure the head movement after having adjusted the rear tethers, we used a set square to have the initial head position and then we pushed forward the helmet measuring the distance from the set square. The distance was 28 *mm* so inside the allowed range (Fig. 3.27b).

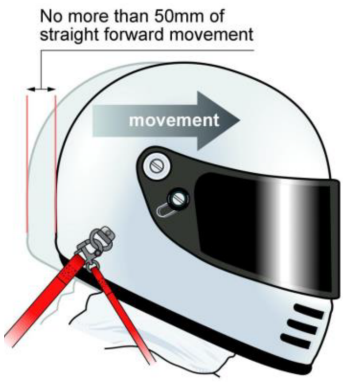

(a) Movement to define the tethers adjustment

(b) Measured head movement

Figure 3.27: Hybrid PRO Tethers length Adjustment

3.4.4.2 Hybrid PRO and Harness

The safety belts to be used must be minimum 5 point harnesses homologated to FIA standard 8853/98 or 8853-2016. Hybrid devices can be used with harness models that are homologated with the standard shoulder strap width of a minimum of 70 *mm*, as well as with models that are homologated with specific shoulder strap width of a minimum of 44 *mm* and that are marked "for FHR use only", or "for HANS® use only", as in our case. (See our safety harness properties Sec.3.4.2).

3.5 Experimental test results

In this section, we discuss the main features and the data obtained from the instrumentation of each frontal crash test. In all, we made five tests:

1. Dummy without helmet;
2. Dummy with open face helmet;
3. Dummy with full helmet;
4. Dummy with full helmet and HANS device;
5. Dummy with full helmet and Hybrid PRO device.

For all the tests, for what concern the crash pulse, it has been used the crash tubes setup and the impact velocity described in Sec.3.2.2.

The signs of the plotted dummy's data showed in this section, are all inherent with the positive directions for neck forces and moments and head accelerations illustrated in Fig.3.15 and Fig.3.17. In this Chapter, for each experimental test we show the plots of sled acceleration, F_x and F_z neck forces, M_y moment at the occipital condyle section, head accelerations and N_{ij} plots.

The detailed raw data filtering process is described in Appendix B. Here we want to explain only the type of filter and the frequency response classes used. A *SAE J221 Butterworth four-poles digital filter* has been used, choosing the correct frequency response class for each output. This because the selection of a frequency response class is dependent upon many considerations, some of which may be unique to a particular test. The ultimate usage of the data and good engineering judgment will determine what portions of the frequency spectrum are significant or useful. We followed the recommendation of SAE J211 for the use of appropriate CFC classes and those used are listed in the Table3.1.

During the definition of Nij in Section2.2.1, we specified that the forces and moments have to be calculated on the occipital condyle section. But in the Hybrid III the neck loadcell is not installed on the section equivalent to the occipital condyle, but is installed above for technical reasons. This positioning of the loadcell, force us to apply a correction to the

Test measurement	Channel Frequency Class (CFC)
Sled acceleration	60
Neck forces	600
Neck moments	600
Head Accelerations	1000
Seatbelt force	600

Table 3.1: Filter frequency response classes used

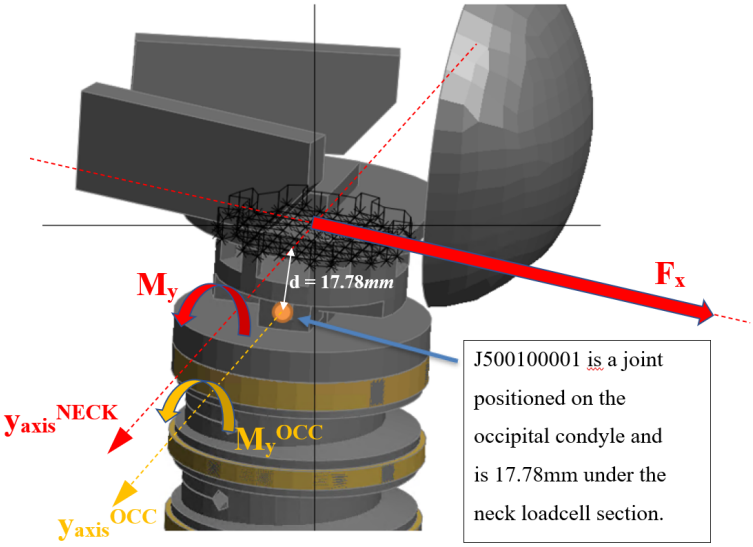

Figure 3.28: Position of the occipital condyle in the Hybrid III FE model

bending moment along the y axis. M_y hence is substituted M_y^{OCC}, where OCC stands for occipital condyle:

$$M_y^{OCC} = M_y - F_x \cdot d \tag{3.1}$$

where F_x is the shear force and d is the distance between the neck loadcell section and the occipital condyle, namely 17.78 mm. We can understand better looking at the position of the occipital condyle and of the neck loadcell section, in the Hybrid III FE model in Fig.3.28. In the neck loadcell section, called UNeck section in the FE model, the only contribution to the bending moment on its y_{axis}^{NECK} is given by M_y which is the moment measured by the neck loadcell. But if we are interested in the M_y^{OCC}, so the bending moment on the occipital condyle section along y_{axis}^{OCC}, we have to consider also the contribution of F_x because respect to the occipital condyle section it has an arm, that is d, and so it creates a moment along the y_{axis}^{OCC}. For our sign convention the M_y is positive when the section is subjected to flexion, while F_x is positive when it points backward. So F_x creates extension respect the y_{axis}^{OCC}, and this is the reason why it is subtracted from M_y. So all the plots that are in this work, experimental and numerical, regarding the bending moment, represent the M_y^{OCC}.

Always regarding the M_y, we had some problems during all the experimental tests re-

garding the acquisition of this moment through the loadcell. As said in Section3.3.1, before the tests we checked the correct functioning of all the loadcell output imposing forces and moments to the head in all the directions with our hands, and even the M_y output was correct. But during the experimental tests, with bigger applied moment, it lost the M_y signal without any explanation. We tried to change the loadcell's connector and cable, we checked if the nodding blocks were worn out, but the problem remained. For this reason the M_y data from experimental tests are not perfect, however we managed to extract some important information for our work.

3.5.1 Dummy without helmet (Dummy-No Helmet)

The more the devices, the more complicated the FE validation becomes. For this reason, the first test have been done with only the dummy, the sled seat and the seatbelts, that are the essential components. Using these data we could validate the basic FE model in the best way.

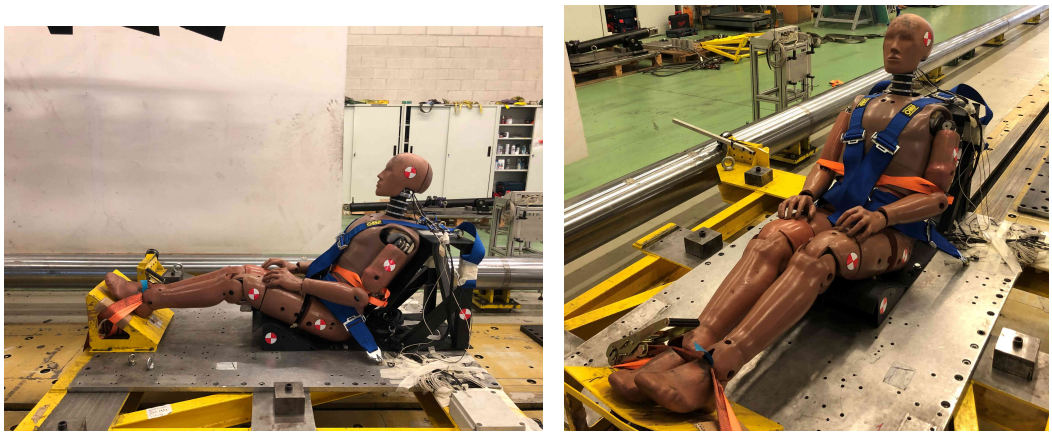

Figure 3.29: Dummy-No Helmet Test initial configuration

It has been registered a sled deceleration peak of 72.12 g. This caused an initial F_z compression peak of 1761 N at 0.03 s, and at 0.03328 s a F_z traction peak of 4840 N. In this test, the problem related to M_y had a small contribution, but we can see that the two bending moment peaks are not perfectly recorded. At 0.034 s we had the registered extension peak of 74.4 $N{\cdot}m$, and then at 0.05024 s the flexion peak of 94.5 $N{\cdot}m$.

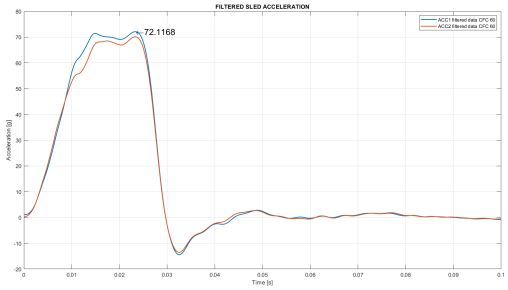
FILTERED SLED ACCELERATION
72.1168
Acceleration [g]
Time [s]

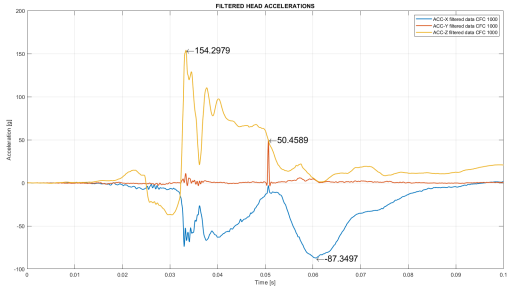
FILTERED HEAD ACCELERATIONS
154.2979
50.4589
-87.3497
Acceleration [g]
Time [s]

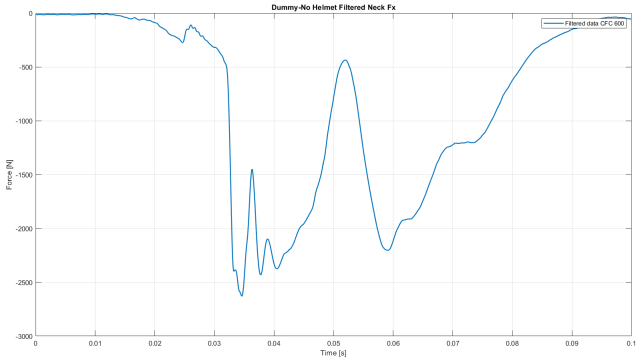
Dummy-No Helmet Filtered Neck Fx
Filtered data CFC 600
Force [N]
Time [s]

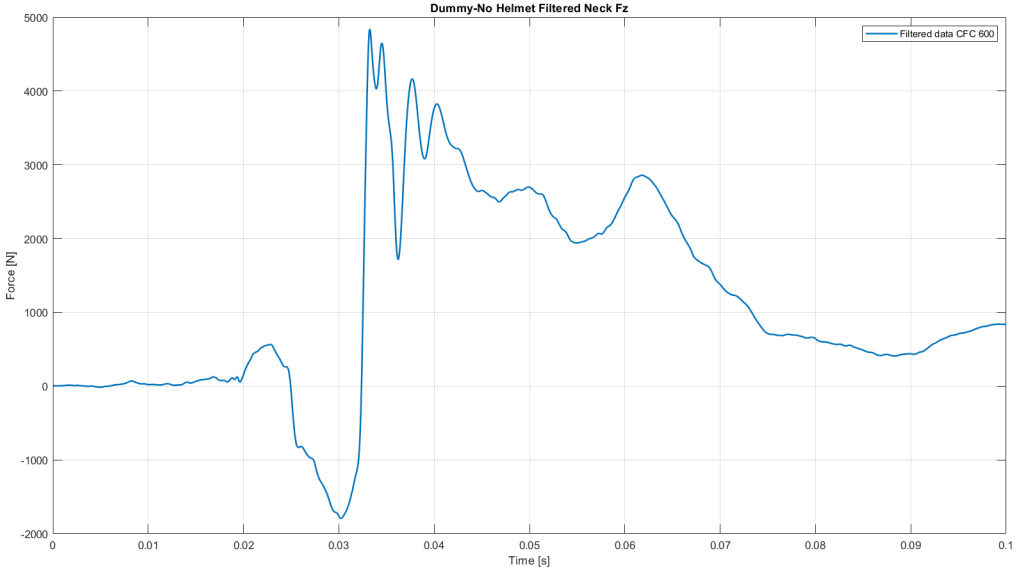
Dummy-No Helmet Filtered Neck Fz
Filtered data CFC 600
Force [N]
Time [s]

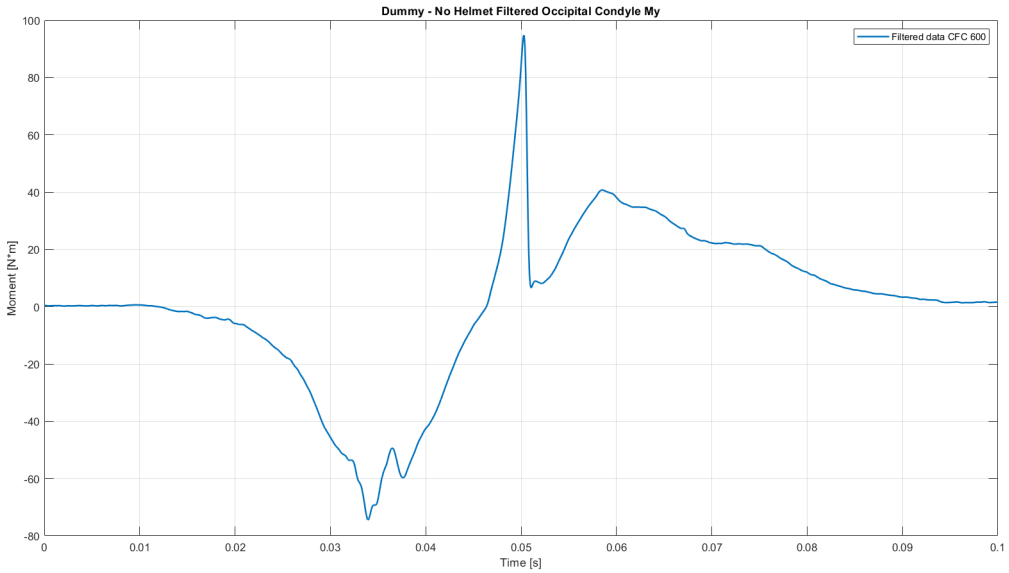

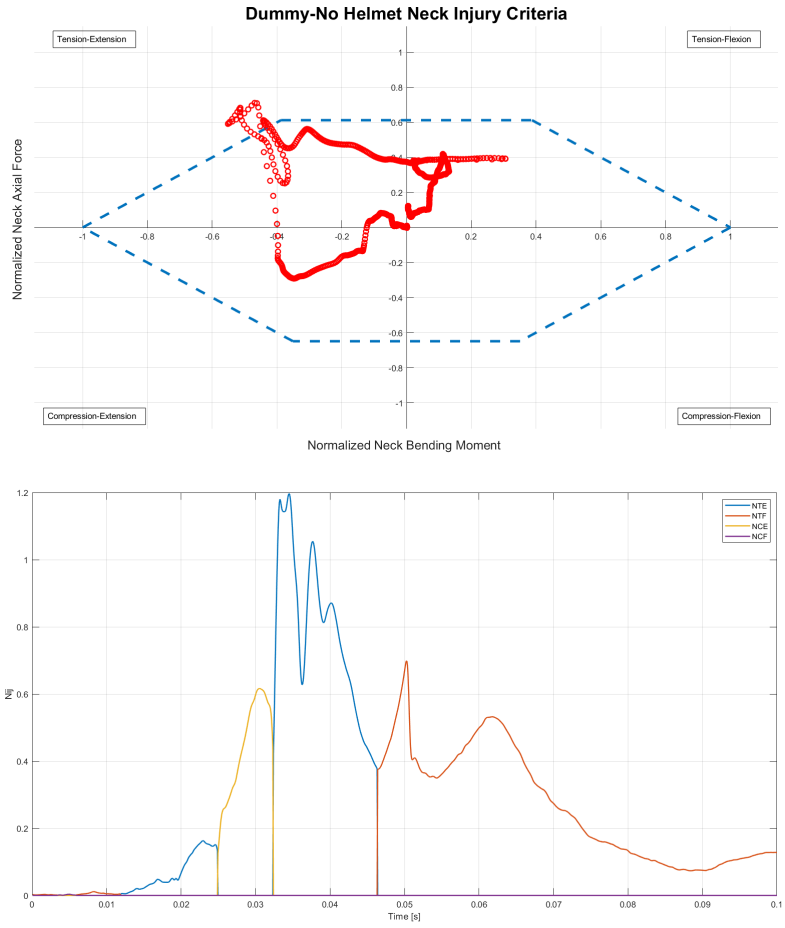

Figure 3.30: Dummy-No Helmet Test Output Data

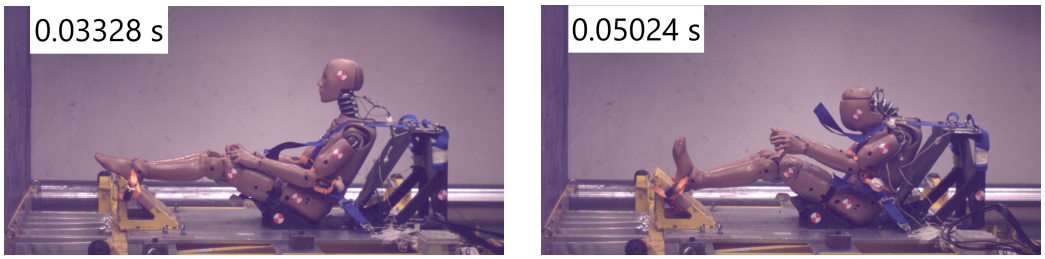

(a) F_z traction peak (b) M_y flexion peak

Figure 3.31: Dummy-No Helmet Test Video Frame

3.5.2 Dummy with open face helmet test (Dummy-001)

This was the first experimental test done. Since on that day the helmet presented in Section3.4.1 was not available, we used another one. It was a Stilo® CARBON PIUMA open face helmet, homologated FIA 8859-2015 and conform to the HANS FIA 8858-10. During the crash test the open face helmet could not withstand the big deceleration peak of 68.96 g and it slipped out of the dummy's head. We have therefore decided to repeat this type of test using the full helmet described in Section3.4.1, but we had the acquisition problem of M_y. Instead the M_y in the test with the open face helmet was perfectly acquired and watching the slow motion video we saw that the helmet slipped out after the flexion moment peak, so the extension and flexion peaks have been only slightly affected by this problem. So we decided not to discard these data, though the helmet slipped out of the head, but to use also them as results for the *dummy with helmet* test.

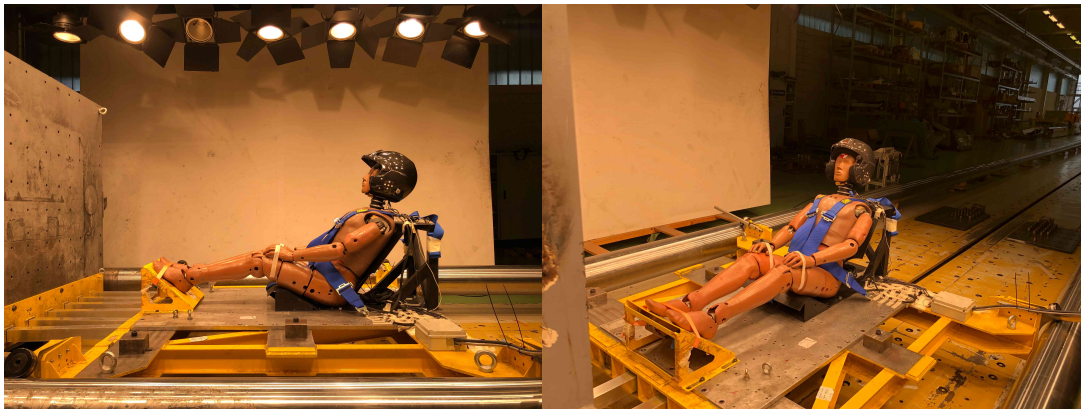

Figure 3.32: Dummy-001 Test initial configuration

The deceleration peak in this case was 68.96 g. The initial F_z compression peak was 3052 N at 0.02832 s, and at 0.04208 s the F_z traction peak of 3949 N. The maximum extension bending moment was 109 $N{\cdot}m$ at 0.04192 s, and the maximum flexion bending moment was 137 $N{\cdot}m$ at 0.0597 s.

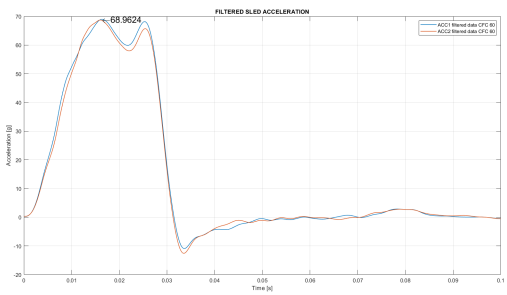

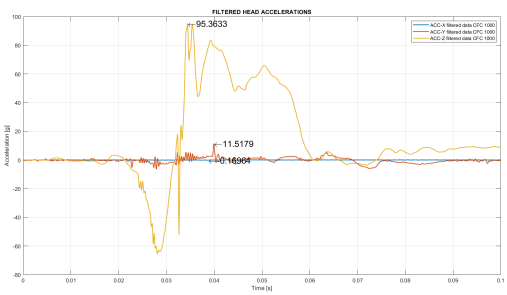

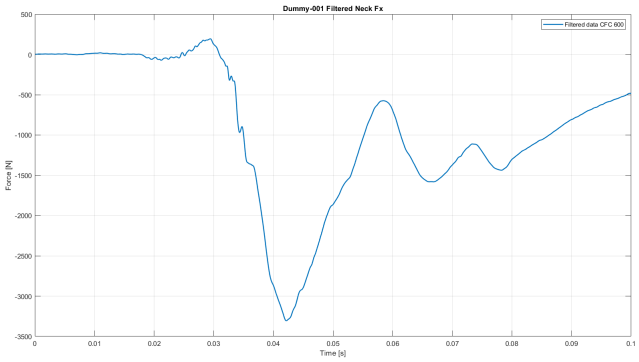
Dummy-001 Filtered Neck Fx
Filtered data CFC 600
Force [N]
Time [s]

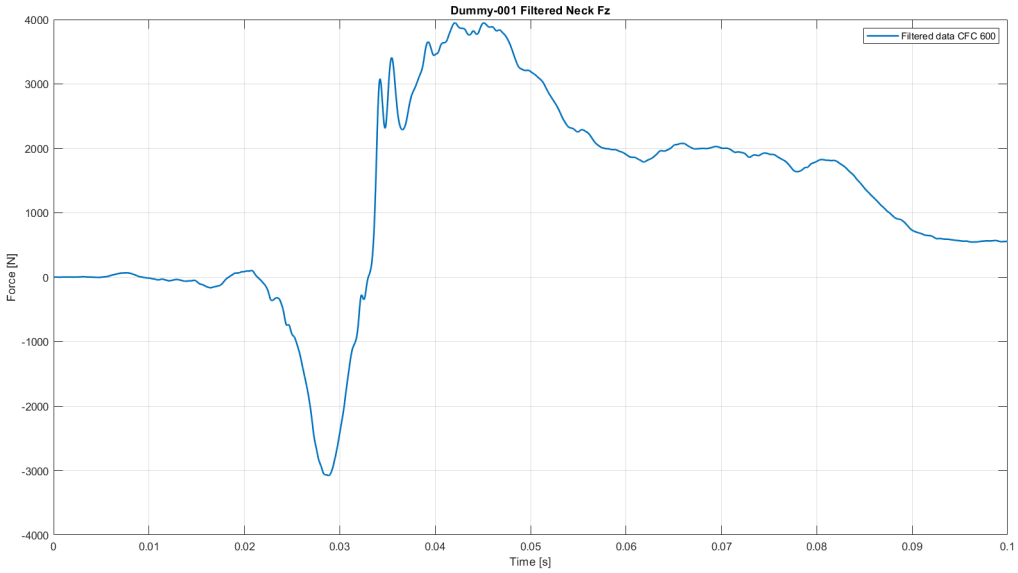
Dummy-001 Filtered Neck Fz
Filtered data CFC 600
Force [N]
Time [s]

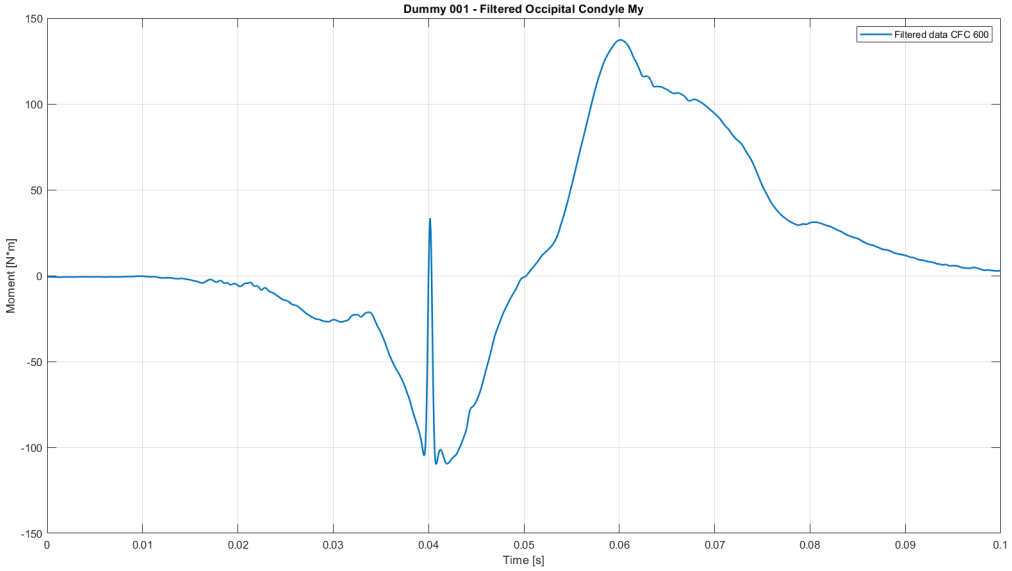
Dummy 001 - Filtered Occipital Condyle My
Filtered data CFC 600
Moment [N*m]
Time [s]

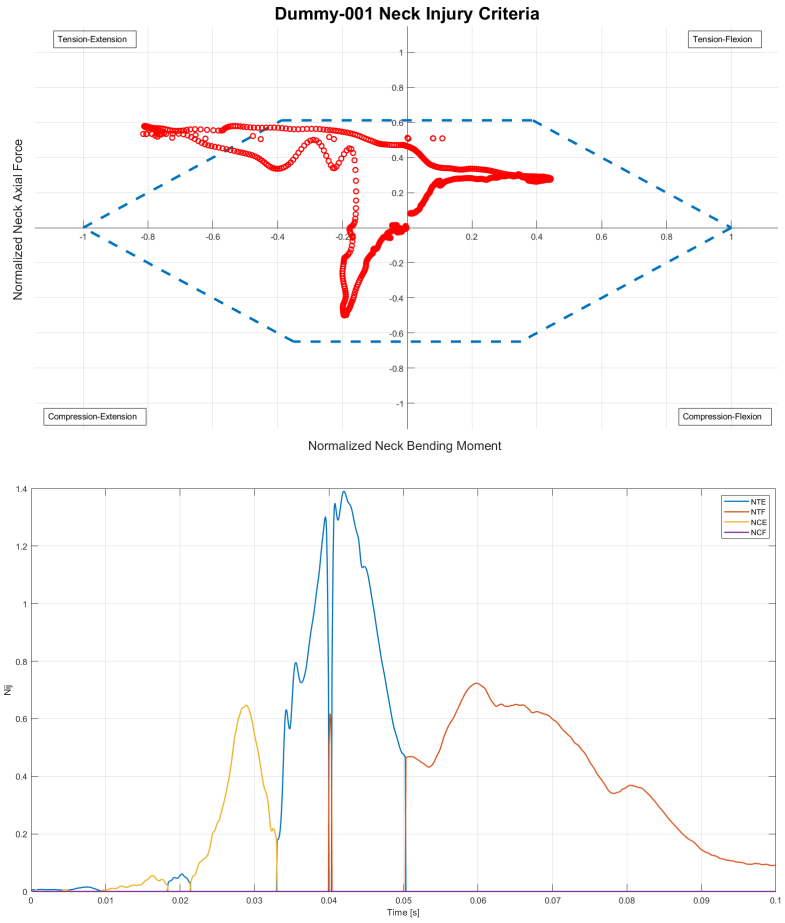

Figure 3.33: Dummy-001 Test Output Data

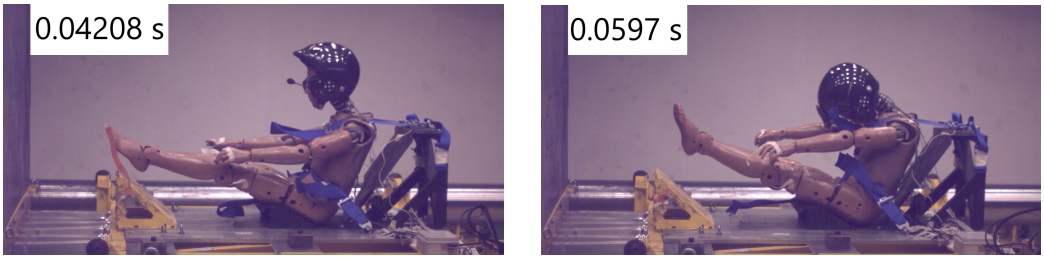

(a) F_z traction peak (b) M_y flexion peak

Figure 3.34: Dummy-001 Helmet Test Video Frame

3.5.3 Dummy with full helmet test (Dummy-002)

As said in the previous Section, the *dummy with helmet* test has been repeated using the full helmet to avoid the slipping out during the crash.

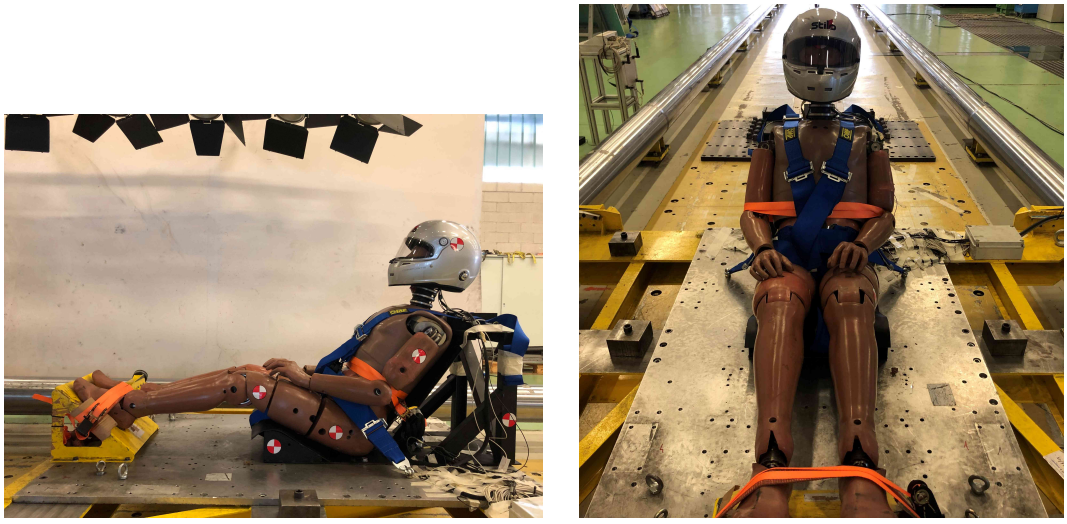

Figure 3.35: Dummy-002 Test initial configuration

The F_z compression peak of 2658 N at 0.02736 s and the F_z traction peak of 5807 N at 0.03864 s, caused by a sled deceleration peak of 72.63 g, have been acquired. At 0.03848 s we had the registered the extension peak of 120 $N{\cdot}m$, and then at 0.05144 s the flexion peak of 60 $N{\cdot}m$.

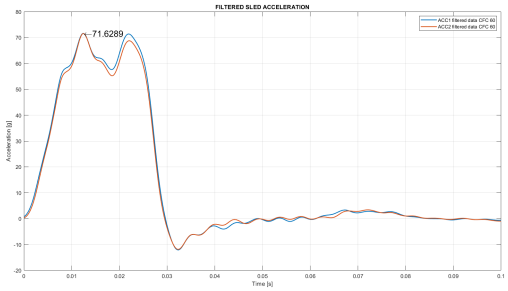

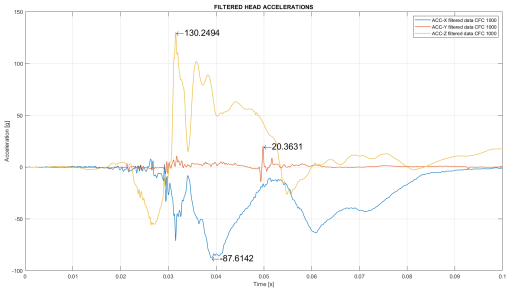

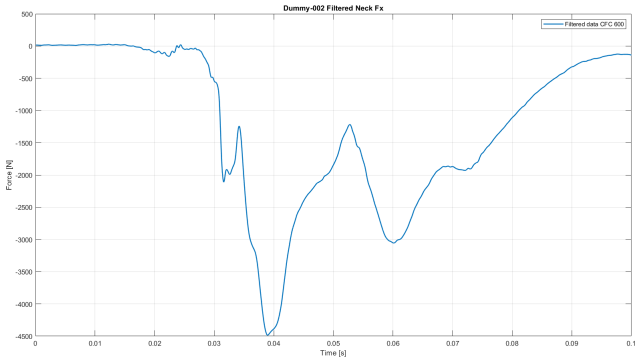
Dummy-002 Filtered Neck Fx
Filtered data CFC 600
Force [N]
Time [s]

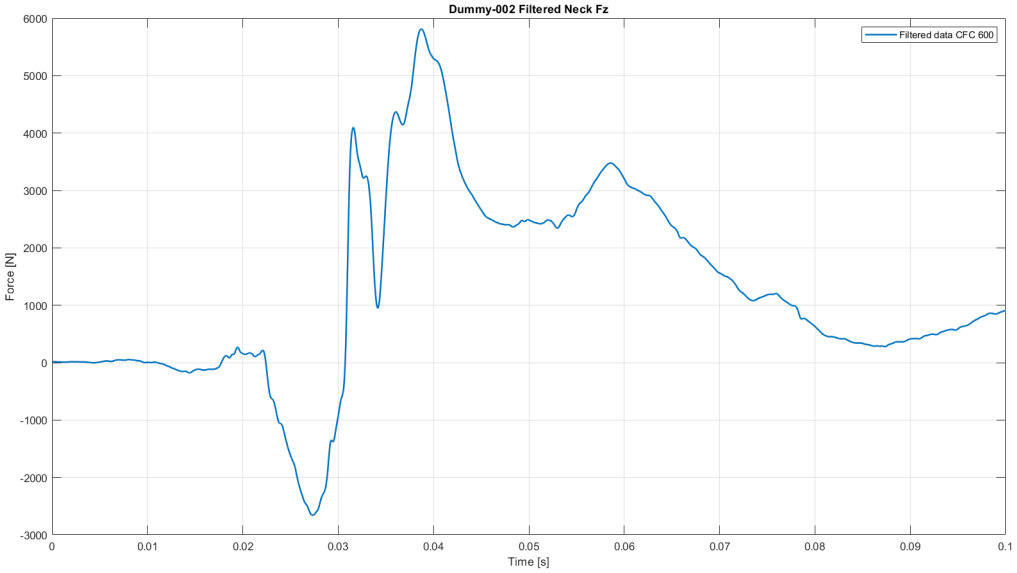
Dummy-002 Filtered Neck Fz
Filtered data CFC 600
Force [N]
Time [s]

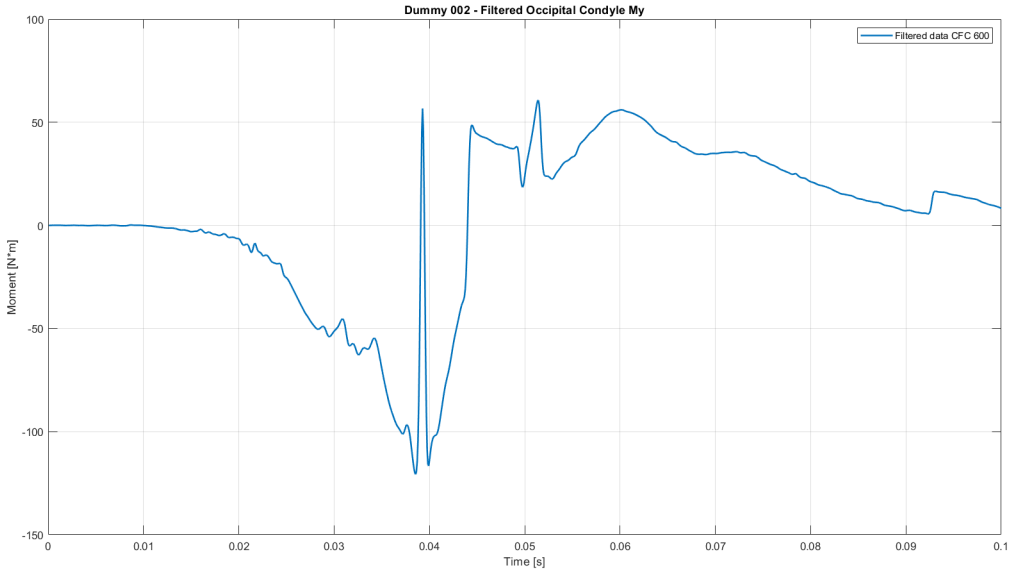
Dummy 002 - Filtered Occipital Condyle My
Filtered data CFC 600
Moment [N*m]
Time [s]

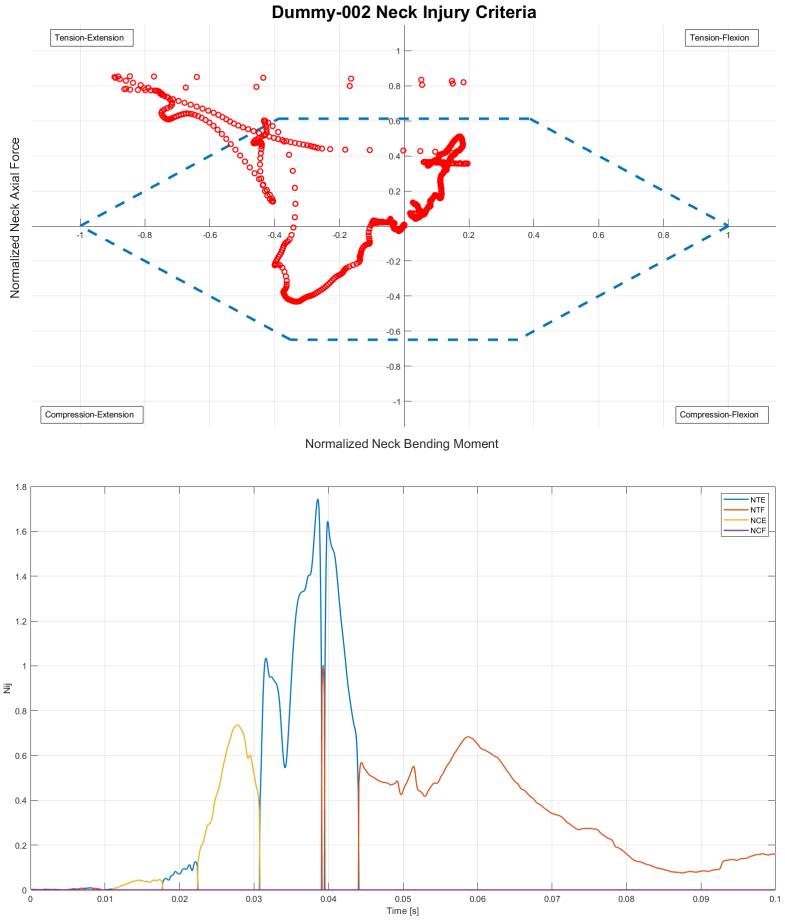

Figure 3.36: Dummy-002 Test Output Data

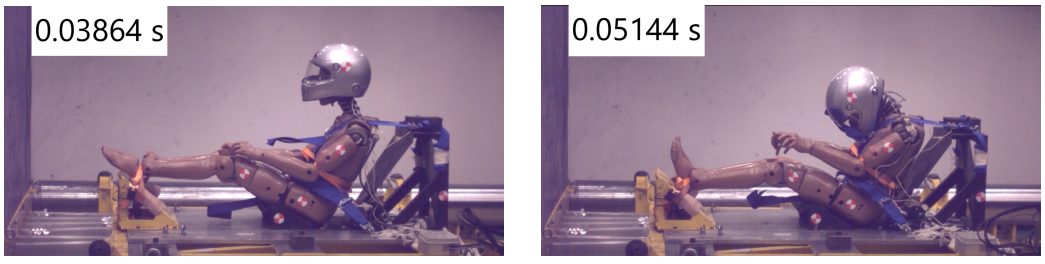

(a) F_z traction peak (b) M_y flexion peak

Figure 3.37: Dummy-002 Test Video Frame

3.5.4 Dummy with full helmet test and HANS device (HANS)

Before the frontal crash test with the HANS device, we checked that that we were respecting all the guidelines on the aspects to take into account when using this FHR device for racing competitions given by the FIA document «*Guide and installation specification for HANS® devices in racing competition» [18].* All the respected guidelines are showed in Section3.4.3.

Figure 3.38: HANS Test initial configuration

It has been acquired a sled deceleration peak of 73.48 *g*. This caused an initial F_z compression peak of 3326 *N* at 0.02864 *s,* and at 0.03656 *s* a F_z traction peak of 1971 *N*. At 0.0396 *s* we had the extension peak of 83.5 *N·m,* and then at 0.0744 *s* the flexion peak of 91.5 *N·m.*

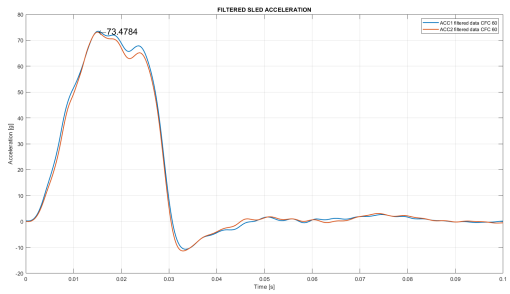

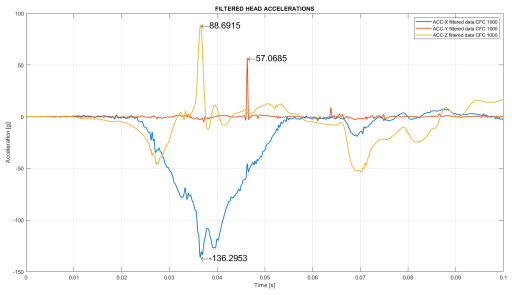

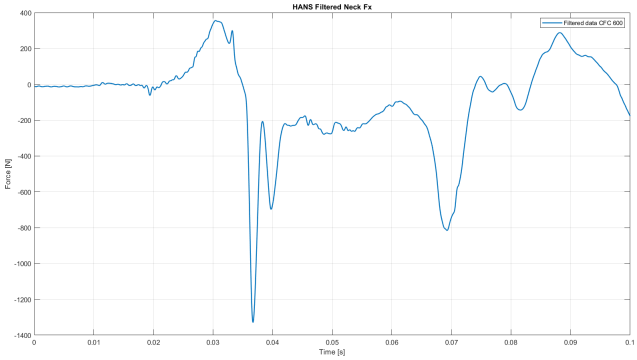
HANS Filtered Neck Fx
Filtered data CFC 600
Force [N]
Time [s]

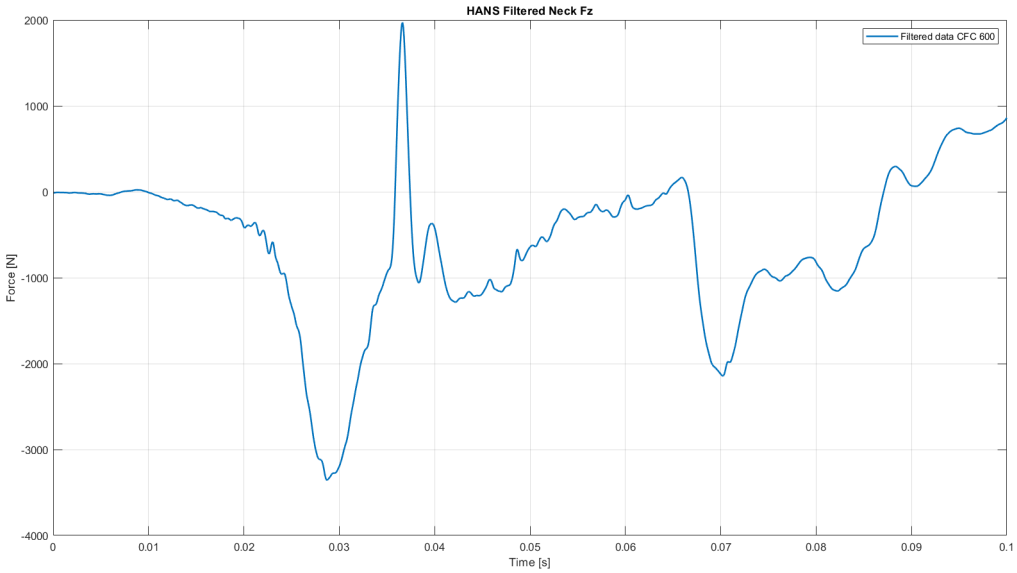
HANS Filtered Neck Fz
Filtered data CFC 600
Force [N]
Time [s]

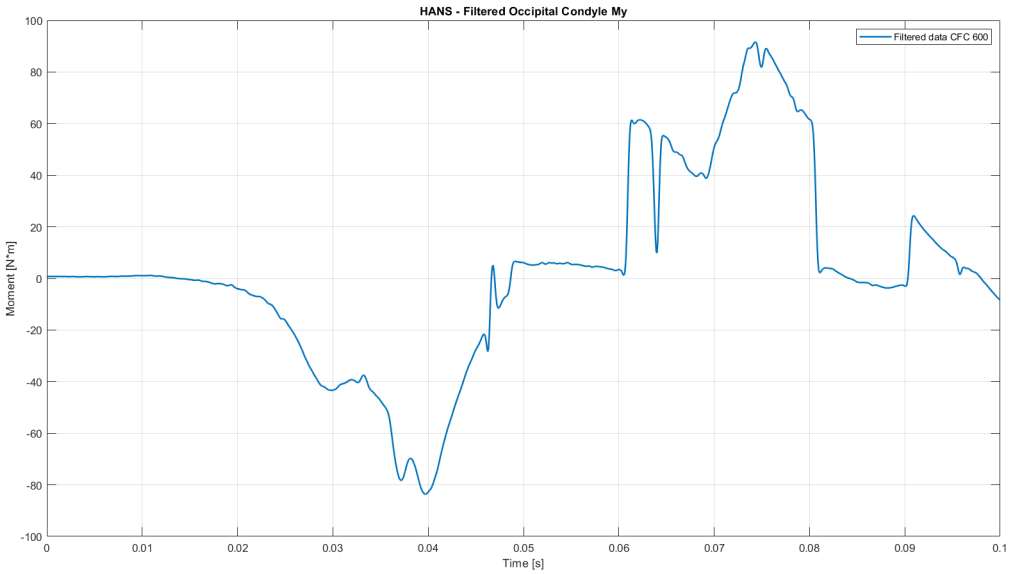
HANS - Filtered Occipital Condyle My
Filtered data CFC 600
Moment [N*m]
Time [s]

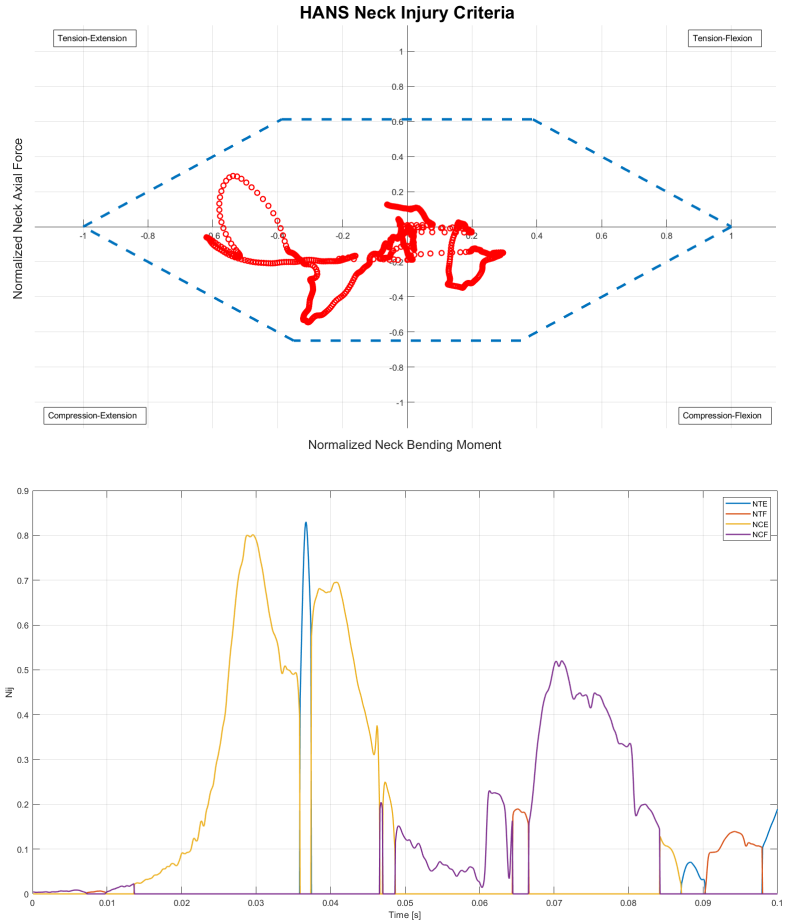

Figure 3.39: HANS Test Output Data

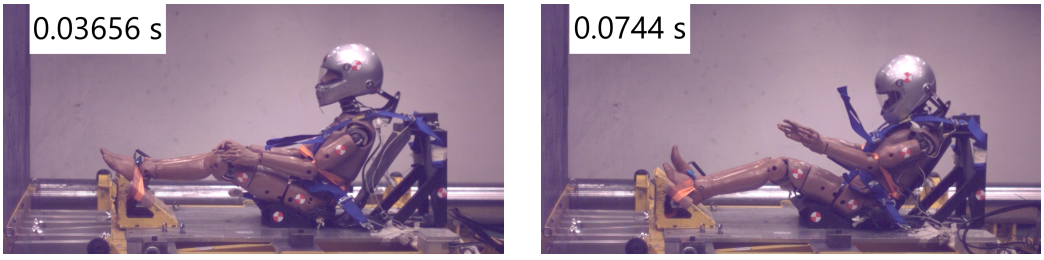

(a) F_z traction peak (b) M_y flexion peak

Figure 3.40: HANS Test Video Frame

3.5.5 Dummy with full helmet test and Hybrid PRO device (Hybrid PRO)

Also in this case, before the frontal crash test with the Hybrid PRO device, we checked that that we were respecting all the guidelines on the aspects to take into account when using this FHR device for racing competitions given by the FIA document «*Guide and installation specification for Hybrid and Hybrid PRO devices in racing competition*» *[19].* All the respected guidelines are showed in Section3.4.4.

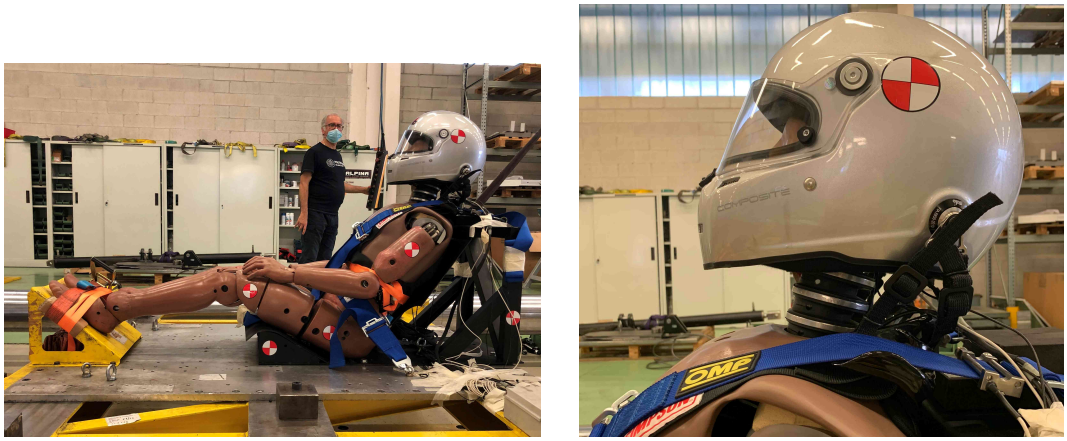

Figure 3.41: Hybrid PRO Test initial configuration

The deceleration peak in this case was 69.94 *g*. The initial F_z compression peak was 2574 *N* at 0.02624 *s,* and at 0.03328 *s* the F_z traction peak of 3803 *N*. This was the worst case for the M_y acquisition, in fact it is not easy to visualize the extension and flexion peaks. The maximum extension bending moment acquired was 70.63 *N·m* at 0.05816 *s,* and the maximum flexion bending moment was 112.7 *N·m* at 0.04136 *s*.

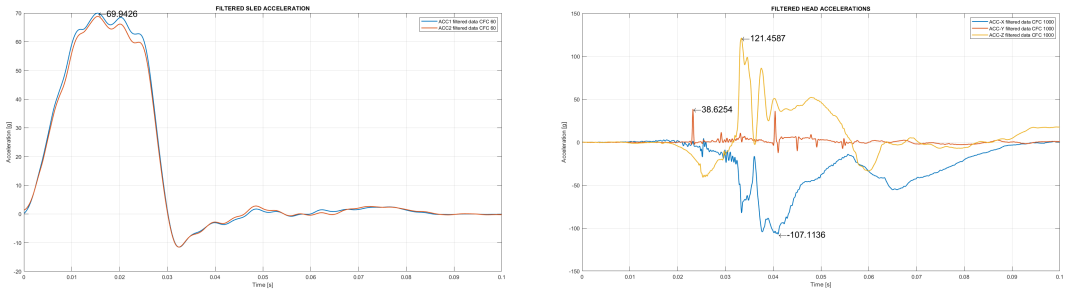

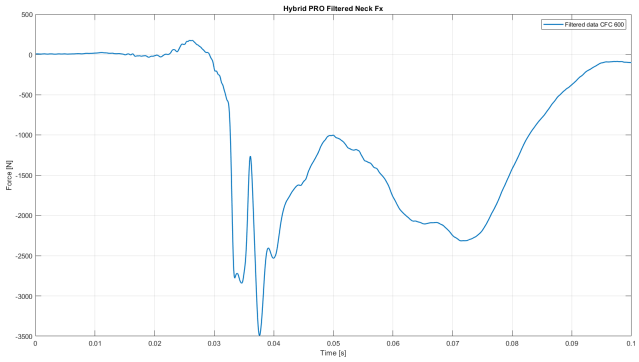
Hybrid PRO Filtered Neck Fx
Filtered data CFC 600
Force [N]
Time [s]

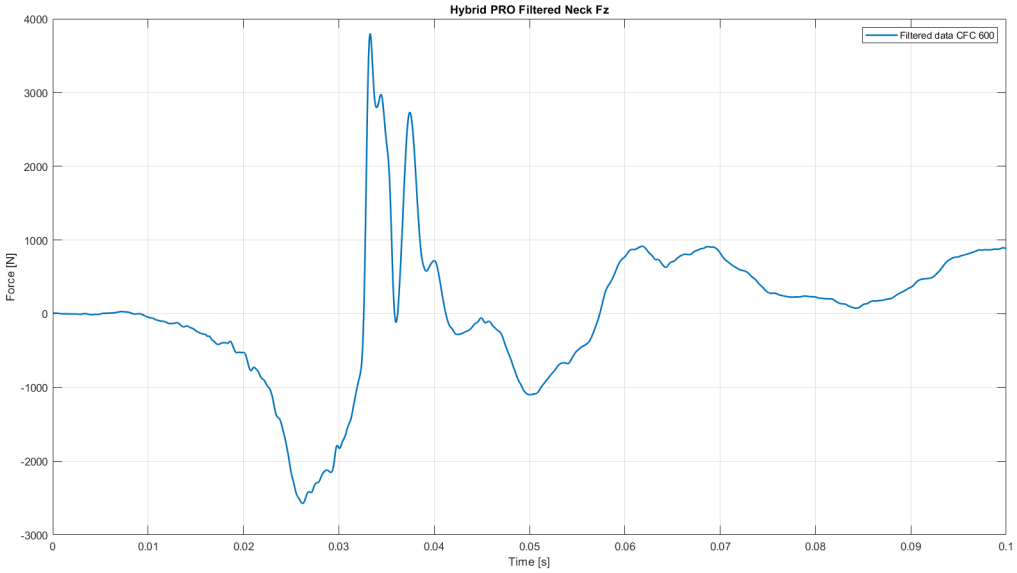
Hybrid PRO Filtered Neck Fz
Filtered data CFC 600
Force [N]
Time [s]

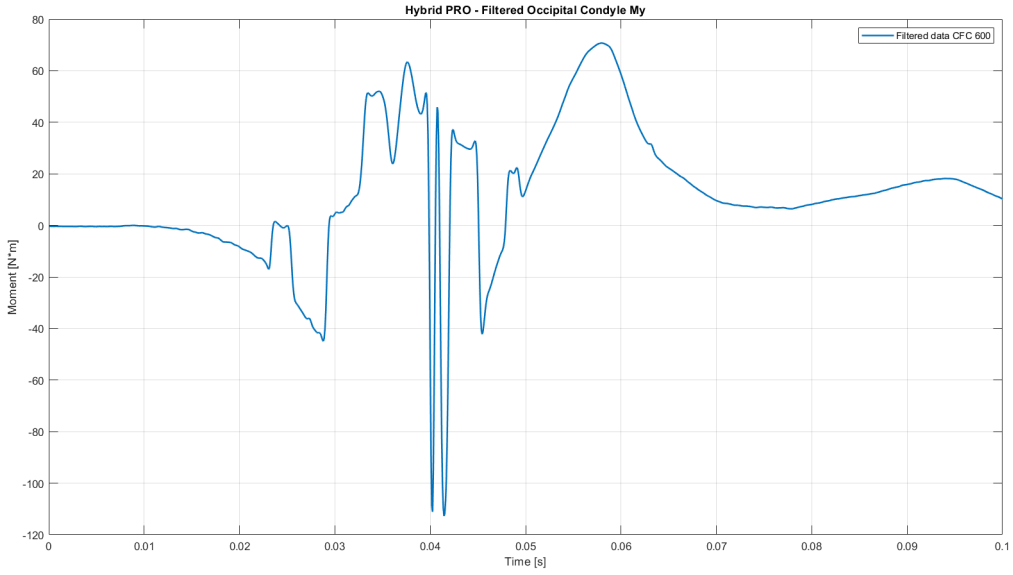
Hybrid PRO - Filtered Occipital Condyle My
Filtered data CFC 600
Moment [N*m]
Time [s]

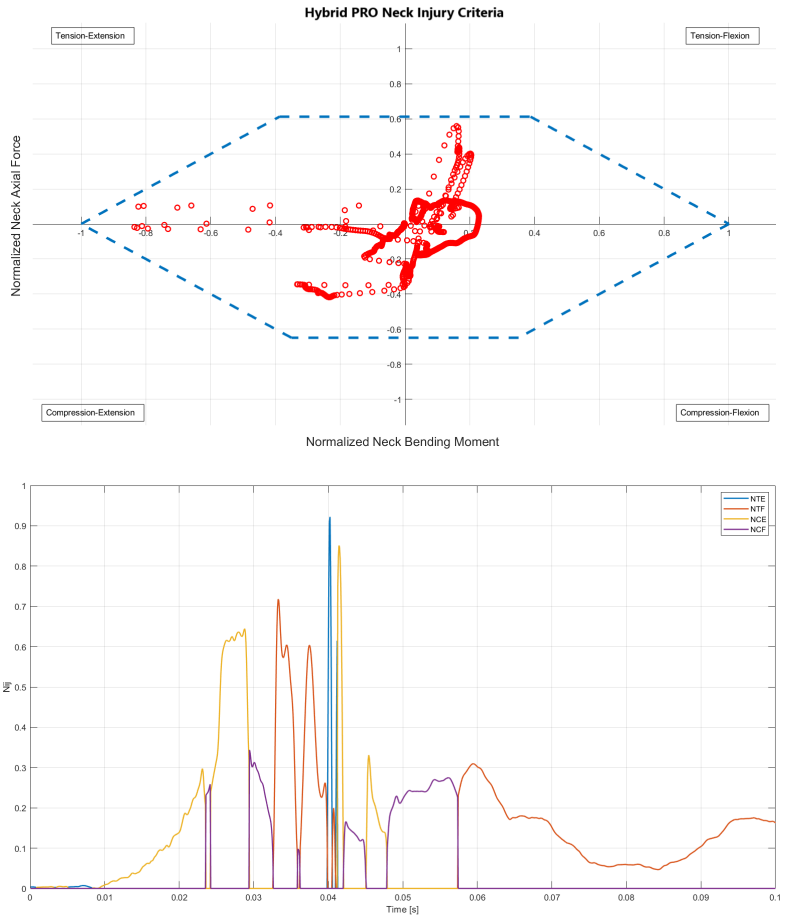

Figure 3.42: Hybrid PRO Test Output Data

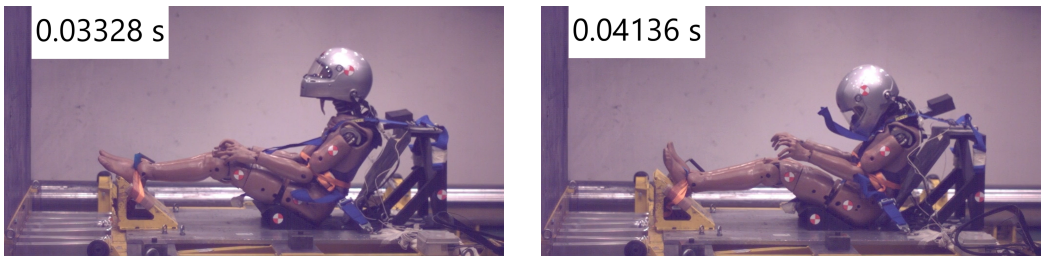

(a) F_z traction peak (b) M_y flexion peak

Figure 3.43: Hybrid PRO Test Video Frame

3.5.6 Experimental tests comparison

In this Section we want to compare the results of the experimental tests with and without the FHR devices, focusing on the F_z neck axial force, the M_y at the occipital condyle section and the resulting N_{ij}.

Starting from the F_z force, we can see that the major benefit of the FHR devices is to decrease the tension neck load. With the FHR devices, in particular the HANS device, we've a strong decrease in the tension peak; taking into account the *Dummy-002* as reference test3.5.3 we had a tension peak of 5807 *N,* while with the HANS device 1971 *N* and with the Hybrid PRO device 3803 *N.* So with the HANS device we had a 66% decrease in the tension peak and with the Hybrid PRO device a 34.5% decrease. Beyond this, looking at Figure3.44 also the average neck load after the peak decreased with the FHR devices. To have these benefits regarding the traction neck load, the compression neck load slightly increased (about 25% with the HANS device respect the *Dummy-002* test3.5.3), caused by the FHR's tethers. But the decrease we had in tension neck load is much greater than the increase we had in compression neck load.

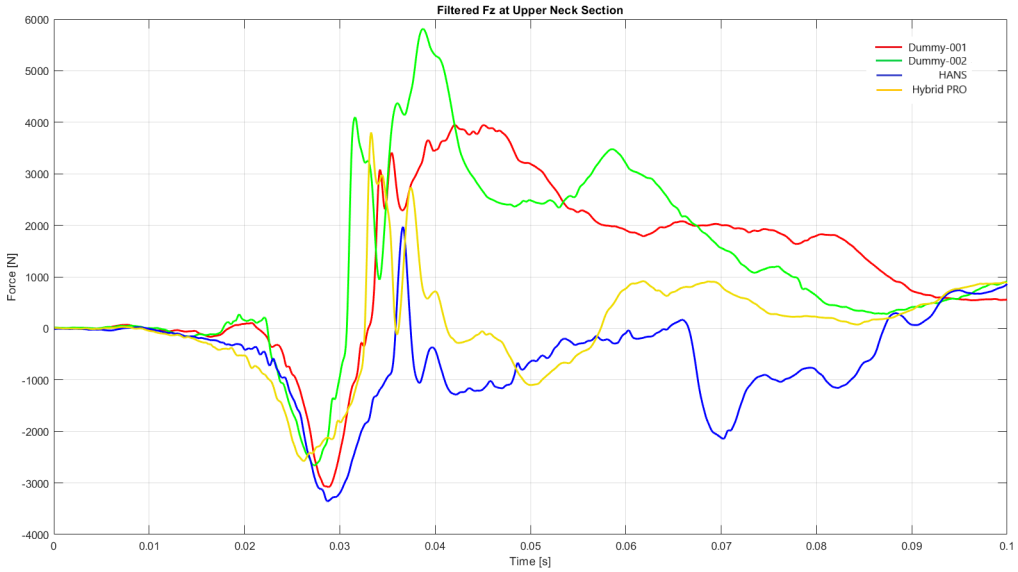

Figure 3.44: Upper neck section F_z comparison

Regarding the M_y at the occipital condyle section it is more difficult to draw conclusions, because of the channel acquisition problem. The best comparison we could do was between the *Dummy-001* test3.5.2, and the *HANS* test. Even if the M_y signal with the HANS device was not perfectly acquired in the flexion part, we could say that both the extension and flexion peaks with the HANS device were smaller than those in the *Dummy-001* test. From Figure 3.45 we can see a 23.5% decrease in the extension peak, and a 33% decrease in the flexion peak.

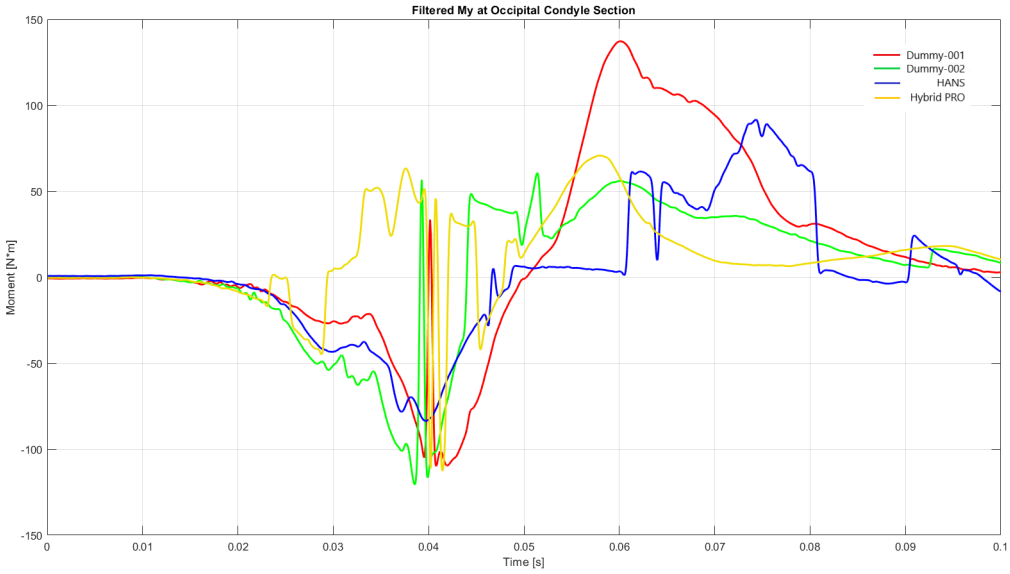

Figure 3.45: Occipital condyle section M_y comparison

All these benefits given by FHR devices, lead to a decrease in the risk of neck injury. This can be visualized with the N_{ij} injury criterion comparison. In Figure 3.46 we can see the box inside the dashed lines that designates the allowable values of F_z loads and M_y moments represented by the normalized calculation, as describe in Chapter2.2.1; instead the colored circles are the combination of measured normalized neck bending moment and normalized neck axial force, moment by moment during the experimental tests. We can see that in the two tests without the FHR devices, *Dummy-001* and *Dummy-002,* the red and green circles go out from the box inside the dashed lines. This means that the N_{ij} criterion is not satisfied in those points. This would be caused by a tension-extension combination around 0.04 *s,* so when we had the tension peaks combined with the extension moment peaks. But, from Figure 3.46 we can see that this injury can be avoided using the FHR devices. In fact the colored circles of the HANS and Hybrid PRO tests never go out from the hexagon box. This mainly thanks to the big decreasing in the tension peak that in these cases failed to exceed the N_{ij} limits in the tension-extension phase.

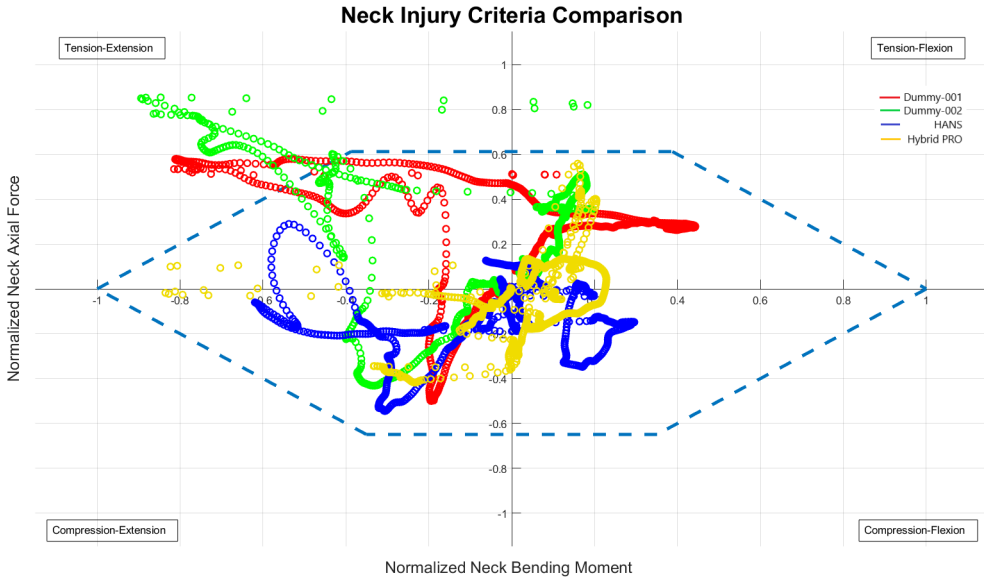

Figure 3.46: N_{ij} comparison

Chapter 4

Hybrid III model validation

In this chapter, we discuss the validation of the Hybrid III FE model. The first step was to reproduce the setup of the sled tests described in Chapter3. Then different numerical simulations for each test were run and the results were compared with the experimental results. A special attention was given to the seatbelt modeling, with a material characterization. Later the same model's setup and features will be used for studying the behavior of the THUMS neck, using a neck injury criterion valid for the latter model. The preprocessors used are Altair HyperMesh® and Oasys PRIMER®

4.1 Sled tests configurations modeling

The reproduction of the experimental tests setups is described in this section, in particular that of the sled seat geometry, of the crash pulse, of the FHR devices, of the seatbelts and of the Hybrid III behavior and instrumentation. The preprocessors used are Altair HyperMesh® and Oasys PRIMER®.

4.1.1 Sled seat

All the dimensions of the sled seat described in Chapter3.1.2 have been measured after having mounted it on the horizontal sled. With them, we could create the exact FE model of the sled seat used during the experimental tests. In Figure 4.1 are shown the numerical test configuration and the experimental one. The four components that create the assembly are constrained together with RIGID_BODIES constraints, so that they move together as a single component.

Several AUTOMATIC_SURFACE_TO_SURFACE [33] contacts have been used to model the contact between the dummy and the sled seat. By controlling the contact force between the Hybrid III and the seat kick is possible to assess if the dummy is correctly seated on the sled seat at the beginning of the crash pulse. At 50 *ms,* that is when the crash pulse begins, the reaction force between the dummy and the seat reaches a value of approximately 700 *N*, that is coherent with the dummy weight.

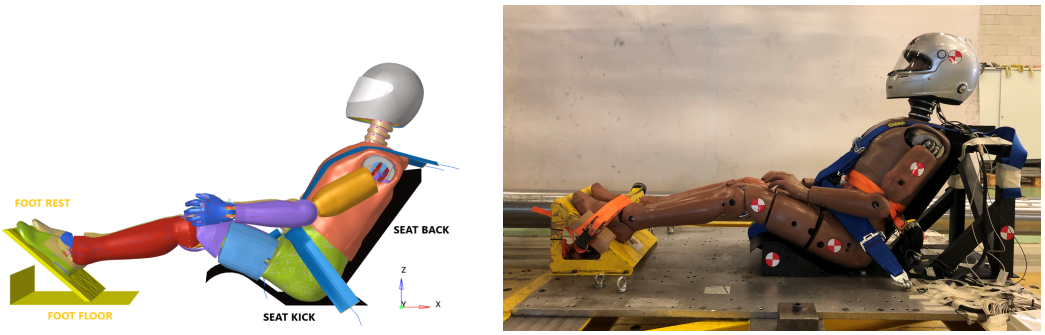

Figure 4.1: Hybrid III numerical and experimental configuration

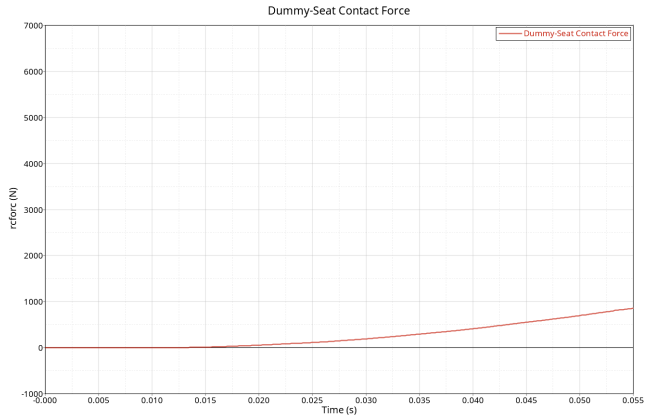

Figure 4.2: Hybrid III-seat contact force

4.1.2 Crash pulse

Since during all the experimental tests we have measured the crash pulses in x-direction (Figure 4.1 shows the global reference system) with the sled accelerometers, we could perfectly reproduce them in all the FE models using the acquired data. It has to be noted that the experimental and numerical tests use different approach for simulating the crash. In fact, the former simulate the crash deceleration by stopping the sled while it is moving at high speed. Thus the observer is not concurrent with the sled itself. This approach correctly emulate the crash and is commonly used in crashworthiness. On the other hand, the latter tests use another approach, namely the observer in concurrent with the sled that is perceived as stationary in the initial instant of the simulation. Then a deceleration equal to the experimental one is applied and the sled starts to move. This is done to decrease the heaviness of the calculations that have to be performed by the calculator, hence the time needed to finish the simulation. Obviously, both the approach are physically correct and should provide the same results. This can be seen in Appendix C, where we discuss a numerical model that we made with the first approach, using the crash tubes.

The crash pulse is provided by prescribing for each test the correct acquired acceleration profile on the sled's foot floor, by using the LS-DYNA card PRESCRIBED_MOTION [33].

Prior to the pulse, a period of adjustment was set so that the dummy could correctly lean against the seat (namely 50 *ms*) thanks to the gravitational Z_LOAD_BODY applied to the model. This because the dummy at the beginning of the simulation is not in contact with the seat to avoid compenetration errors. It has to be noted that in experimental tests results the crash pulse starts at 0 *ms*, so from now on the experimental graphs will be shifted of 50 *ms* in order to match the numerical data. After the pulse, the simulation continued until the total time left was 150 *ms* (hence the CONTROL_TERMINATION [33] card was set to 0.15).

4.1.3 FHR devices

The HANS and Hybrid PRO's CAD models were provided by FIA. The FE models have been created with an internal solid part and an outer shell skin. Since the FHR devices are made of very stiff all-carbon bodies, at the internal solid part has been assigned a MAT_020:RIGID [33]. Instead, the outer skin is made of 2D-Shell elements with nodes corresponding to the solid part's external nodes. To this skin has been assigned a MAT_009:NULL [33] and has been used to simplify the contact between the FHR devices and the dummy. The meshes have been created taking advantage of the symmetrical geometry of the FHRs. So initially only half of the model have been meshed and then it has been mirrored along the symmetry axis, in this way we obtained perfectly symmetrical meshes.

The correct fitting of the FHR devices to the Hybrid III model has been made with fitting numerical simulations. This because the FHR's shape is optimized for a real human body, so the Hybrid III needed fitting analysis. These consisted in putting the FHR devices in the good position, even if there were compenetrations with the Hybrid III. Then the FHR devices have been moved away from the dummy by a predetermined amount. A PRESCRIBED_MOTION towards the dummy has been assigned to the FHRs of the same amount that they had previously been moved away. In this way, assigning also the contact, the devices reached the initial correct positions deforming the Hybrid III external jacket.

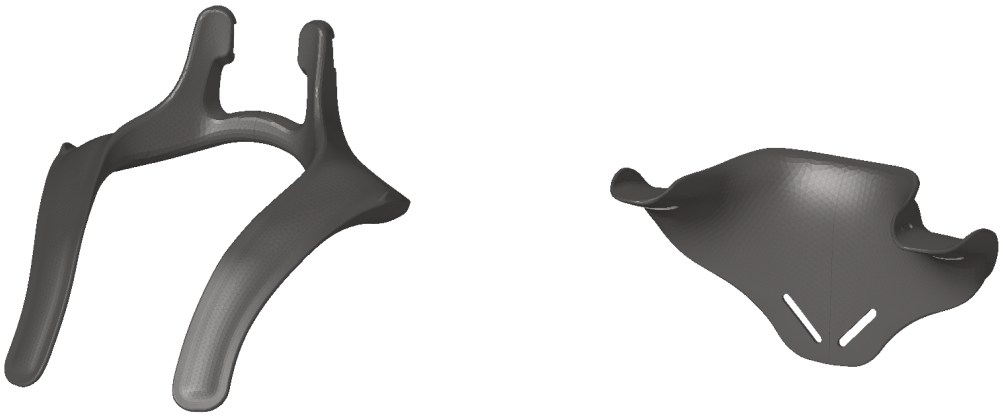

Figure 4.3: FHR's FE meshes

4.1.3.1 HANS FE model

To model the tethers, 1D ELEMENT_SEATBELTs have been used. The material and section's properties were provided by FIA. In Figure 3.23, is possible to see that in reality the HANS tethers are made in one piece that can slide through the arched top. To allow this also in the FE model, two simple sliprings have been added (colored in green in Figure 4.4).

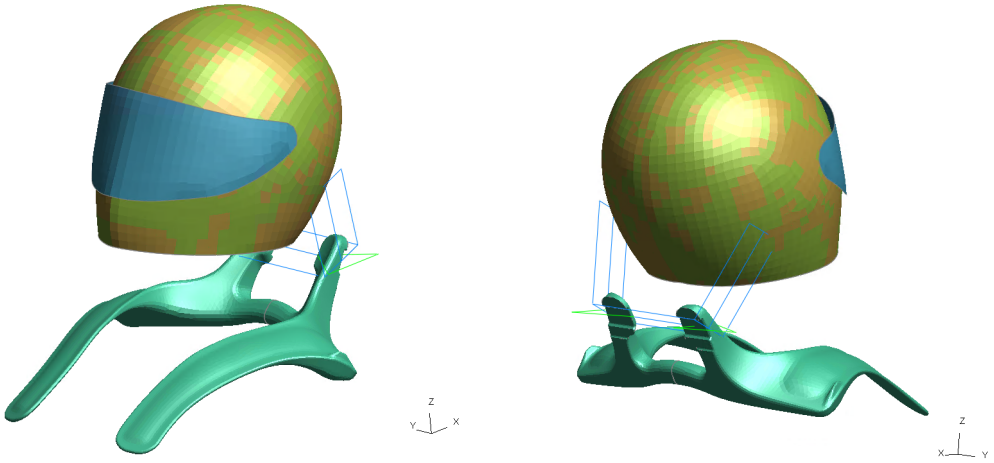

Figure 4.4: HANS FE model

Since the tethers when mounted must not be in tension but they must have a slack length, as described in Section 3.4.3.2, before the HANS experimental test (3.5.4), we measured the total tethers length and then the tethers length when mounted. In this way we could calculate the real slack length to give to each tether in the FE model. But the CAD model of the real helmet used in the experimental tests was not available, so we used another helmet CAD model provided by FIA. This was smaller than the real one, so we could not perfectly reproduce both the real position of the helmet's connection point and the real tether's length. Different numerical simulations were run to understand the behavior of the neck axial force F_z and the bending moment M_y changing the position of the helmet's connection point and the tether's slack length.

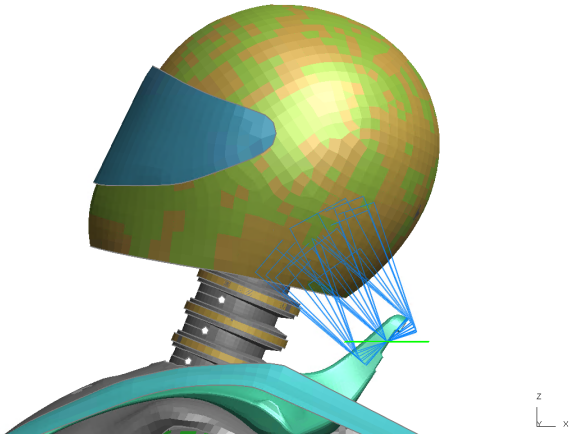

Figure 4.5: All the different helmet's connection point positions tested

From the results of the analysis we could understand that the helmet's connection point position influences more the bending moment M_y, instead the tether's slack length influences more the neck axial force F_z. In particular, the more the helmet's connection point is positioned towards the back of the helmet the more it tends to slightly increase the extension part of M_y, and the more it is positioned towards the front of the helmet the more it tends to increase a lot the flexion part of M_y. Regarding the tether's slack length, the more the slack length increased the more the F_z tension peak increased. This because increasing the slack we delayed the point at which the tethers began to work, so the F_z tension peak increased like no FHR device was being used. With these conclusions, firstly we found the best helmet's connection point position that gave good results about the bending moment M_y, and then we set the tether's slack length that gave the right F_z tension peak. The chosen nominal length and slack length were 107 *mm* and 80 *mm*.

Also in the FE model we checked the geometrical guidelines listed in Section 3.4.3.1.

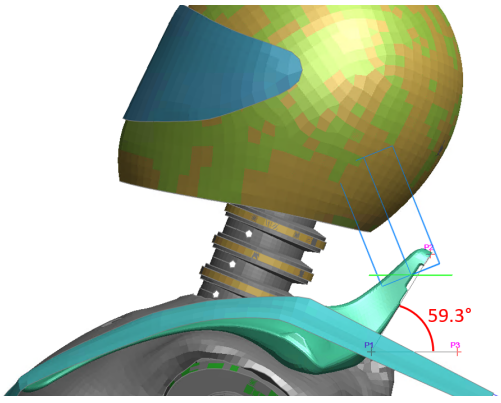

Figure 4.6: HANS FE model measured angle

4.1.3.2 Hybrid PRO FE model

To be consistent, also in this model it has been set the same helmet's connection point position used in the HANS FE model. The Hybrid PRO device, as described in Chapter 3.4.4, has front and rear tethers; both of them have been modeled with 1D ELEMENT SEATBELTs as for the HANS' tethers. The front ones are independent of each other, while the rear tethers in reality are made in one piece that can slide through the rear part of the device. Four simple sliprings have been added in the path of the rear tethers to allow this movement. Also in this case we couldn't respect the real tethers' slack lengths measured before the experimental test, due to different dimensions of the helmet model used. So we run several numerical simulations with different slack lengths, for both front and rear tethers, and we found the best combination to reproduce the experimental neck axial force F_z and bending moment M_y.

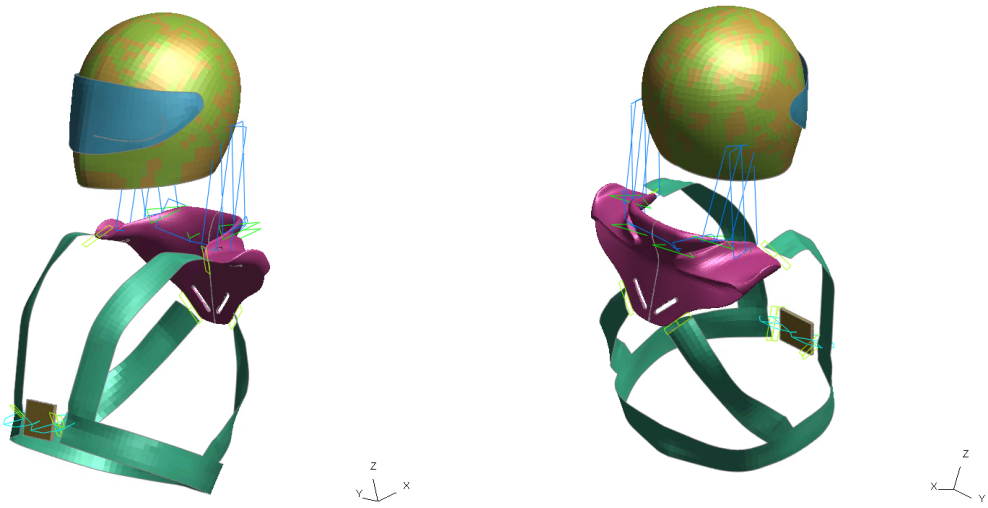

Figure 4.7: Hybrid PRO FE model

The Hybrid PRO's body belts have been modeled by using the safety seatbelt tool of PRIMER, as for the safety harness modeling (Section 4.1.4). Since it was impossible to reproduce all the body belts with only one path, five independent seatbelts paths have been defined, one for each body belt portion. The connections between the body belts and the Hybrid PRO model have been done with one 1D ELEMENT_SEATBELT to avoid instability problems during the belt fitting. Then the four upper belts have have been combined with the lower belt creating manually 2D ELEMENT_SHELL, thus forming a single part. From the first simulations, we saw that during the crash pulse the body belts had loose-fitting so we decided to put two retractors on lower belt buckle to pull the belts before the crash pulse started. For this reason two 1D ELEMENT_SEATBELTs have been added on each side of the buckle.

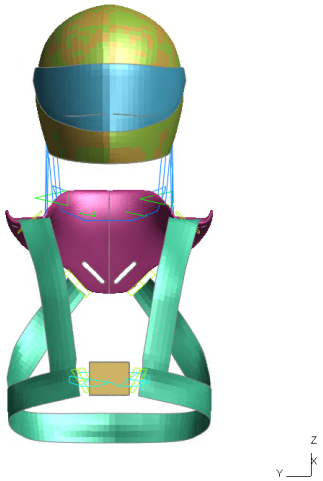

Figure 4.8: Hybrid PRO body belts and buckle's retractors

4.1.4 Seatbelts

The seatbelts were modeled by using the safety seatbelt tool of PRIMER. The real seatbelts mounting points of the sled seat (Figure 3.20) have been measured and then exactly reproduced in the FE model creating nodes corresponding to those points. To make these nodes move together with the sled, CONSTRAINED_EXTRA_NODES [33] between the rigid sled's foot floor and the nodes have been created. The safety harness FIA installation angles (Figure 3.21) have been respected also in the FE models. This was simple for all the configurations since the sled seat had the same shapes and dimensions of the real one, the dummy has been positioned following some measures taken during the experimental tests and the seatbelts mounting points had the same positions of the real ones. As you can see in Figure 4.9, the seatebelts FE model perfectly fits the real configuration.

Figure 4.9: Seatbelts comparison

The whole real safety harness have been modeled, so six seatbelts were modeled and linked to a central buckle in the FE model. Only the shoulders have been simplified, considering them all with a width of 2". Each seatbelt is made of three part: the central part is modeled with 2D ELEMENT_SHELL, meanwhile the ends are modeled as 1D ELEMENT_SEATBELT. The shoulders and crotch straps had five elements in the width direction, with an element size equal to 10x10 *mm,* so a total belt width of 50 *mm.* Instead, the lap strap had eight elements in the width direction, with an element size equal to 10x9.375 *mm,* so a total belt width of 75 *mm.* The shell elements material for each strap is defined by the card MAT_001_ELASTIC [33] (see Appendix A for the seatbelts' material characterization). The thickness of each seatbelt was 1.8 *mm.*

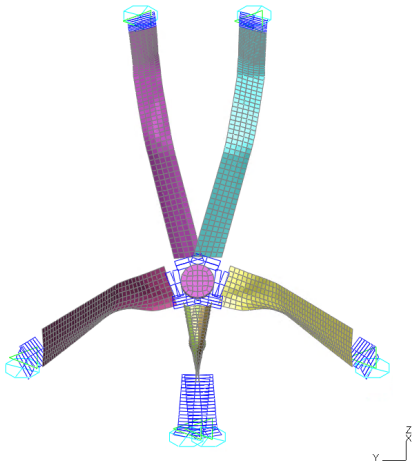

Figure 4.10: Seatbelts FE model

In motorsport there are no type of retractors, so once the seatbelts are tighten they do not loosen up like civilian vehicles seatbelts. In order to reproduce this behavior, five retractors and five sliprings were implemented. In the analysis, the retractors are left able to tighten the seatbelts during the adjustment phase (until 50 *ms*) then the sliprings block the seatbelt so that the retractor is not able to loosen the seatbelts up. Because of the retractors, the 1D elements enter in the slipring and "disappear", thus it is important to add enough 1D elements to the ends near the sliprings.

For each simulation, the *sbtout_belt_force* have been studied, in particular the ones of the shoulders straps to compare them with the experimental ones measured by the seatbelt's load cell (Section 3.4.2).

4.1.5 Hybrid III FE model

Firstly, the positioning of the dummy have been done. This has been done easily with the dummy positioning tool of PRIMER. With this tool we could move and rotate each dummy's sub-assembly, positioning them following the measures taken during the dummy

positioning on the real sled seat (Figure 3.5). The result is very satisfying as you can see in Figure 4.11, the comparison between the dummy positions in the Dummy-002 test (Section 3.5.3).

Figure 4.11: Dummy position comparison

Then, the Hybrid III FE model was equipped with all the database card necessary for the calculation of the important quantities for us. In particular, in Figure 4.12 is shown the cross-section on the upper neck that operates as a load cell. In LS-DYNA there are two categories of cross-sections:

- SET cross-sections: if the SET option is used, just one card is needed which identifies a node set and at least one element set. In this case the node set(s) defines the cross section, and the forces from the elements belonging to the element set(s) are summed up to calculate the section forces. Thus the element set(s) should include elements on only one side (not both sides) of the cross section. [33]
- PLANE cross-sections: a PLANE is defined and a set part is selected. Based on this cutting plane, a node set and element set(s) which comprise the cross section are internally generated.. If no set part is selected LS-DYNA will include all the part of the model; a reference system is requested for the output. [33]

The upper neck cross-section is a set cross-section for the calculation of neck forces and moments. In the model provided by FIA there were already some modifications on the neck FE model, performed by using the MSc thesis *"Optimization of head and neck behavior in Hybrid III FEM models and validation through sperimentation"* by S.Motta, former Politecnico di Milano student, as a reference [37]. This to improve the accuracy of the neck outputs, in particular of the neck moment.

As already said in Section 3.5, we were not interested in the bending moment M_y in the UNeck section, but in the occipital condyle section. In the numerical simulations this

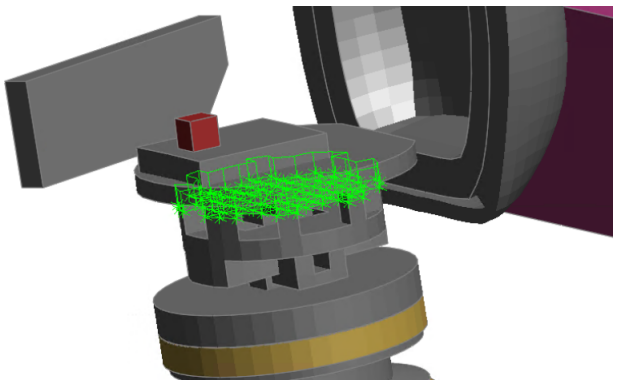

Figure 4.12: Hybrid III UNeck section

correction was done automatically by the software, that calculated the M_y in the occipital condyle section represented by the Joint ID 50100001 (Figure 3.28). So from the *jntforce* output, *Joint Stiffness, U_Neck_CorrMoment_INJURY, theta_moment_total,* we could obtain automatically the M_y at the occipital condyle. A check have been done to be sure that these LS-DYNA automatic output values corresponded to the values found with the Equation 3.1. In Figure 4.13 this comparison is represented, and we can see that the difference between the moment in the joint and the calculated one, is small enough to allow us to use the *U_Neck_CorrMoment_INJURY* as output.

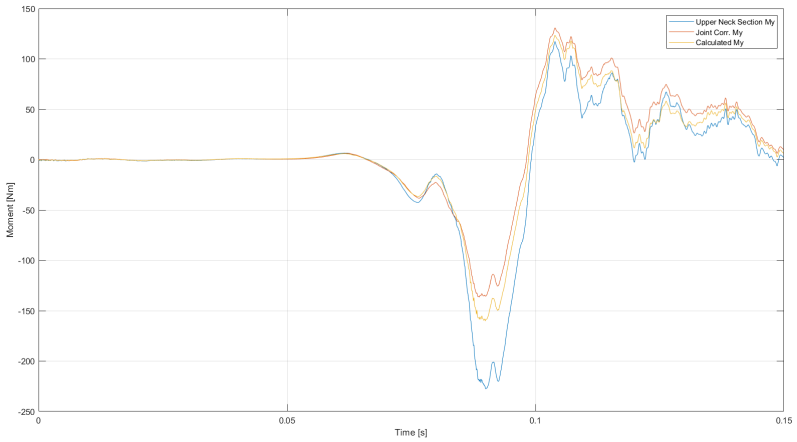

Figure 4.13: M_y corrections comparison

From the experimental graphs showed in Chapter 3.5, we can see that initially F_z had a compression peak in all the tests. This were due to the dummy seating position and the constraint of the feet to the footrest with a ratcheting strap (Section 3.3). To model this constraint, and so to reproduce the initial F_z compression peak, we gave to rigid parts of the feet a PRESCRIBED_MOTION [33] with the same acceleration crash pulse given to the sled's foot floor for each test. In this way the feet moved with the same acceleration profile of the footrest, as they were constrained on it. But in reality the ratcheting strap couldn't totally constrain the feet, because the high forces during the crashes widened the strap giving some

freedom to the feet. For this reason, a *death_time* to the feet's PRESCRIBED_MOTION has been set, different for each numerical model since in every experimental test the ratcheting strap behaved differently. For each numerical model, several simulations with different *death_time* were run to better reproduce the initial F_z compression peak.

4.2 Hybrid III numerical simulations results

In this section, we discuss the comparison between the numerical simulation results and the experimental tests results. The signs of the plotted dummy's data showed in this section, are all inherent with the positive directions of neck forces and moments and head accelerations illustrated in Fig.3.15 and Fig.3.17. All the numerical raw data results have been filtered with the same type of filter and the frequency response classes used for the experimental tests, showed in Chapter 3.5. To have the numerical animations, BINARY_D3PLOTs [33] with a DT = 0.005 *s* have been set as output.

For each numerical simulation, we show the comparison plots with the experimental tests results of *x* and *z* head accelerations, F_x and F_z neck forces, M_y moment at the occipital condyle section, N_{ij} plots and seatbelt's shoulders strap forces. To avoid confusion, only the numerical N_{ij} *vs time* plot is shown. For completeness, there are also tables that show in detail the most important results in term of peak values and peak time together with their error with respect to the each experimental test data. The error for the peak value are calculated in percentage with respect to the experimental peak value, while the peak time error is represented by the time difference.

$$err_{\%} = \frac{|| \, val_{num} \, | - | \, val_{exp} \, ||}{| \, val_{exp} \, |} \cdot 100$$

Where val_{num} is the value given by the numerical simulation data and val_{exp} is the value given by the experimental data.

4.2.1 Dummy without helmet

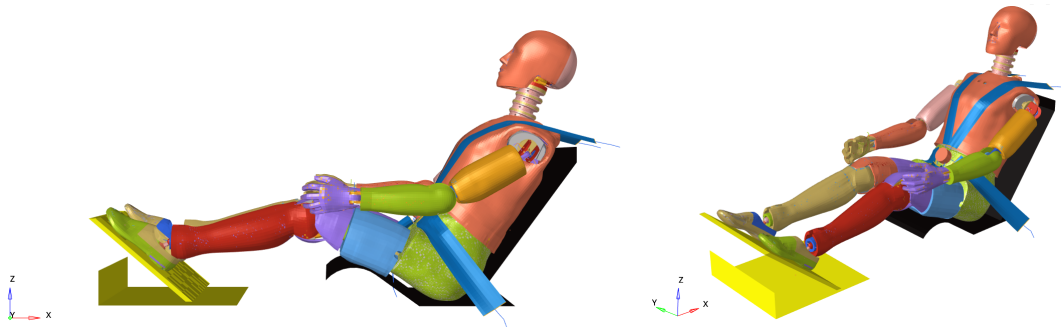

Figure 4.14: Dummy-No Helmet simulation initial configuration

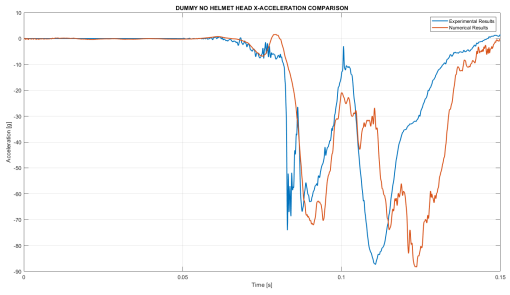

(a) Head x-acceleration

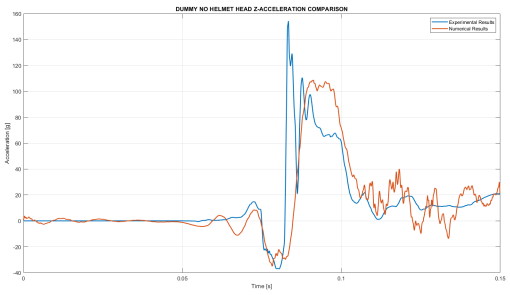

(b) Head z-acceleration

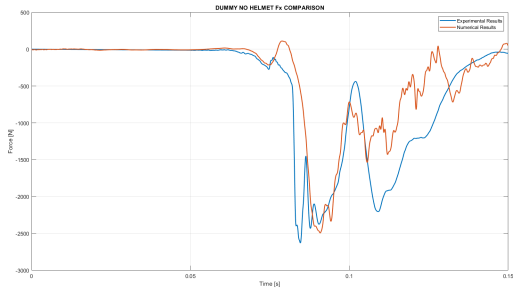

(c) F_x

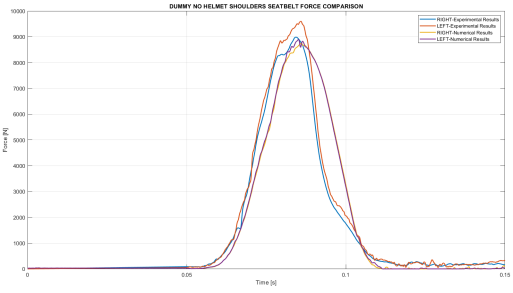

(d) Seatbelt force

Figure 4.15: Dummy-No Helmet simulation output data comparison

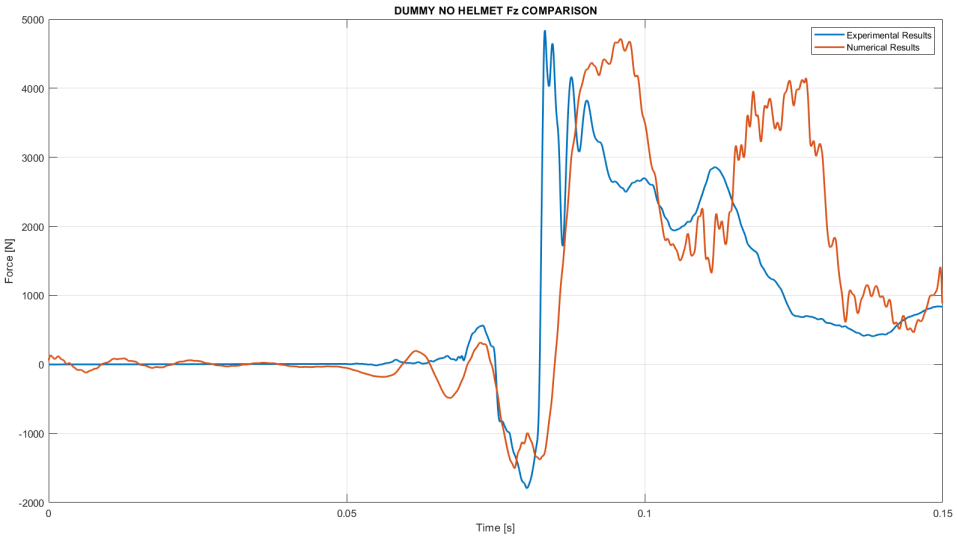

Figure 4.16: Dummy-No Helmet F_z comparison

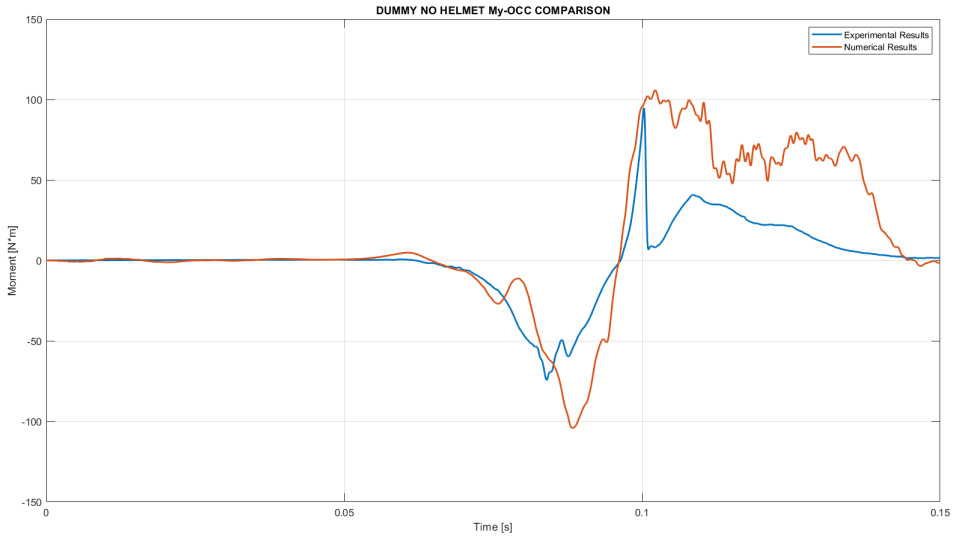

Figure 4.17: Dummy-No Helmet M_y comparison

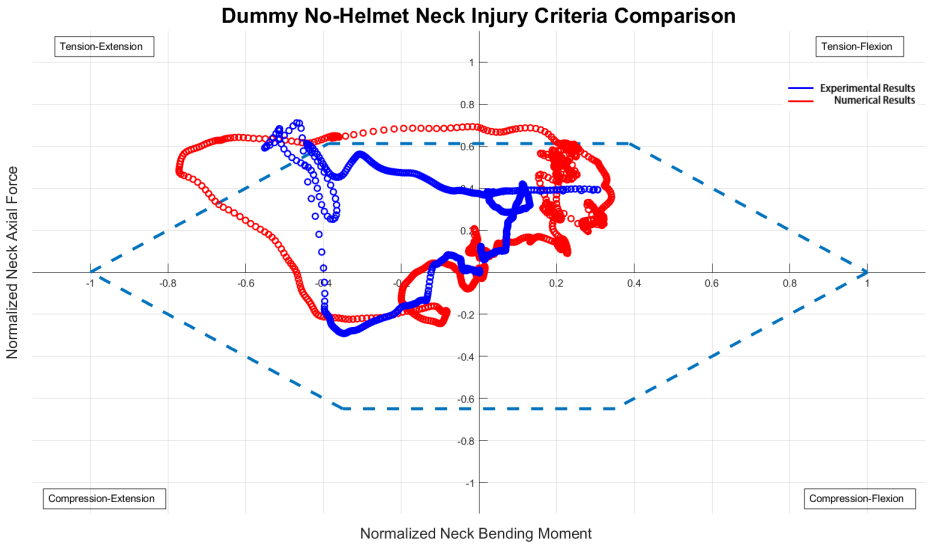

Figure 4.18: Dummy-No Helmet N_{ij} comparison

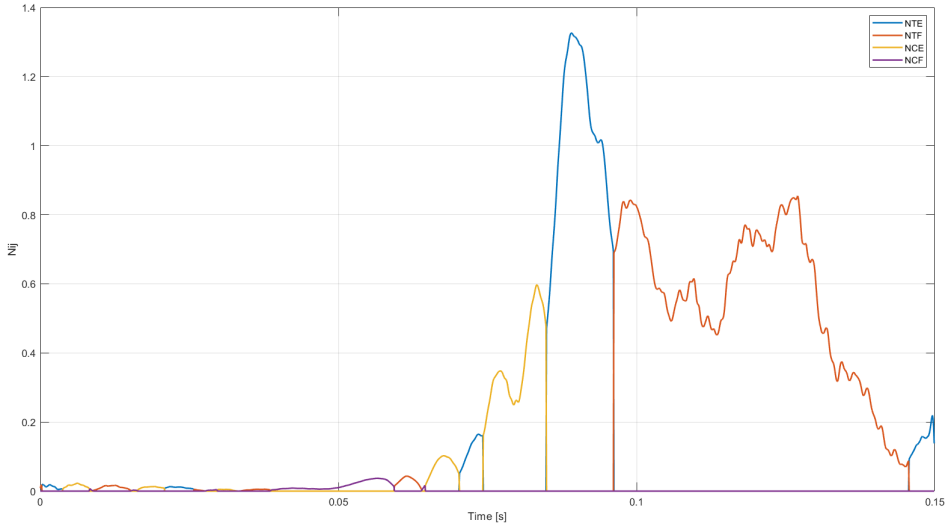

Figure 4.19: Dummy-No Helmet N_{ij} vs. time

Graph		Peak value	$err_{\%}$	Peak time (s)	Δerr (s)
Head acceleration (g)	acc_x^{EXP}	87.35		0.11072	
	acc_x^{NUM}	88.22	0.99%	0.12361	0.01289
	$acc_z^{EXP}+$	154.30		0.08336	
	$acc_z^{NUM}+$	108.76	29.51%	0.09110	0.00774
	$acc_z^{EXP}-$	36.87		0.08024	
	$acc_z^{NUM}-$	35.00	5.07%	0.07830	-0.00194
UpperNeck Force (N)	F_x^{EXP}	2628.51		0.08464	
	F_x^{NUM}	2491.77	5.20%	0.09090	0.00626
	$F_z^{EXP}+$	4828.41		0.08320	
	$F_z^{NUM}+$	4714.09	2.37%	0.09590	0.01270
	$F_z^{EXP}-$	1795.17		0.08024	
	$F_z^{NUM}-$	1504.33	16.21%	0.07820	-0.00204
Neck $M_{y,OCC}$ ($N{\cdot}m$)	$M_{y,OCC}^{EXP}+$	94.74		0.10032	
	$M_{y,OCC}^{NUM}+$	105.79	11.66%	0.10220	0.00188
	$M_{y,OCC}^{EXP}-$	74.42		0.08392	
	$M_{y,OCC}^{NUM}-$	104.20	40.02%	0.08830	0.00438
Seatbelt Force (N)	$F_{S_{right}}^{EXP}$	8986.70		0.08408	
	$F_{S_{right}}^{NUM}$	8753.89	2.59%	0.08609	0.00201
	$F_{S_{left}}^{EXP}$	9602.12		0.08592	
	$F_{S_{left}}^{NUM}$	8896.49	7.35%	0.08512	0.00080
Neck Injury Criteria	N_{ij}^{EXP}	1.19		0.08456	
	N_{ij}^{NUM}	1.31	10.08%	0.08910	0.00454

Table 4.1: Dummy-No Helmet Simulation $err_{\%}$

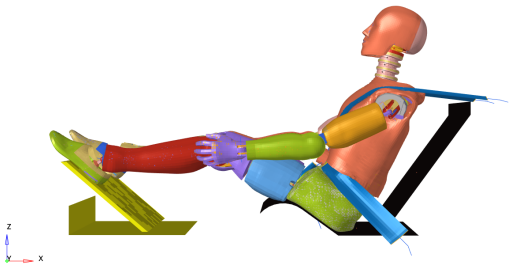

(a) t = 0.080 s

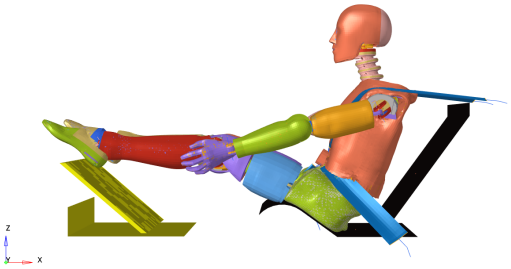

(b) t = 0.090 s

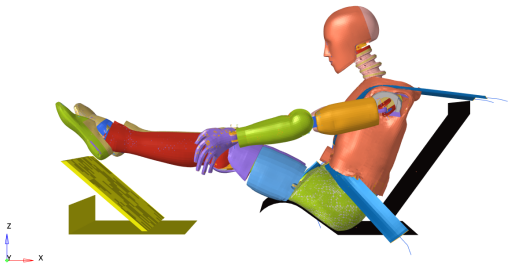

(c) t = 0.095 s

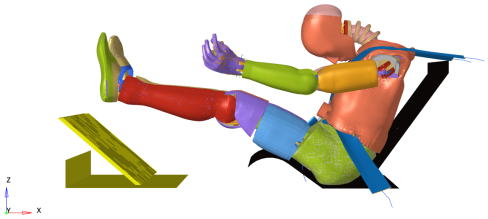

(d) t = 0.105 s

Figure 4.20: Dummy-No Helmet Simulation Peak Frames

4.2.2 Dummy with helmet

The comparison, in particular of M_y, for the *Dummy with helmet* test has been done with both the *Dummy-001* (3.5.2) and *Dummy-002* (3.5.3) experimental tests, as mentioned in Chapter 3.5.2.

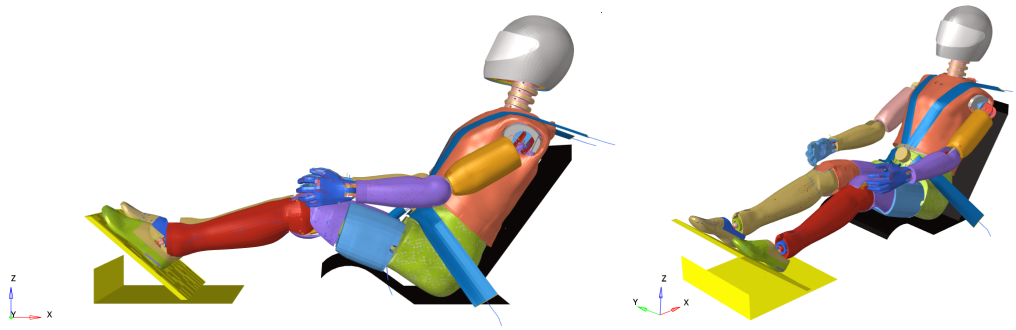

Figure 4.21: Dummy - Helmet simulation initial configuration

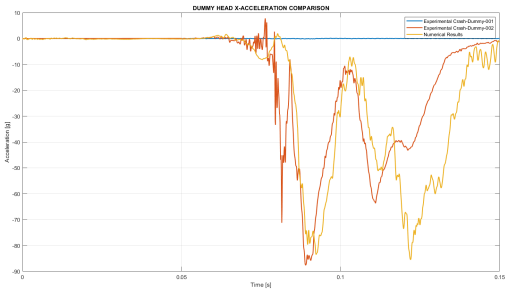

(a) Head x-acceleration

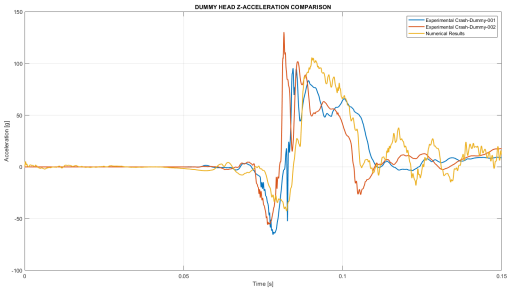

(b) Head z-acceleration

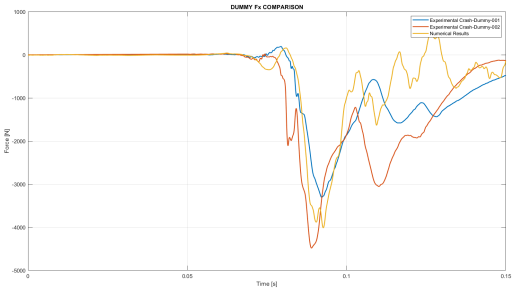

(c) F_x

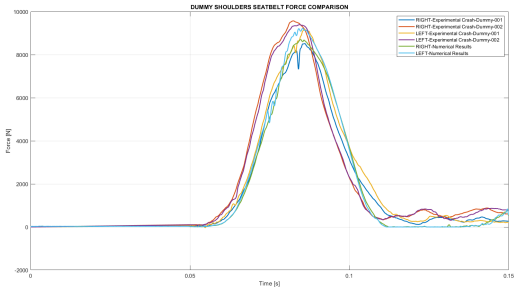

(d) Seatbelt force

Figure 4.22: Dummy - Helmet simulation output data comparison

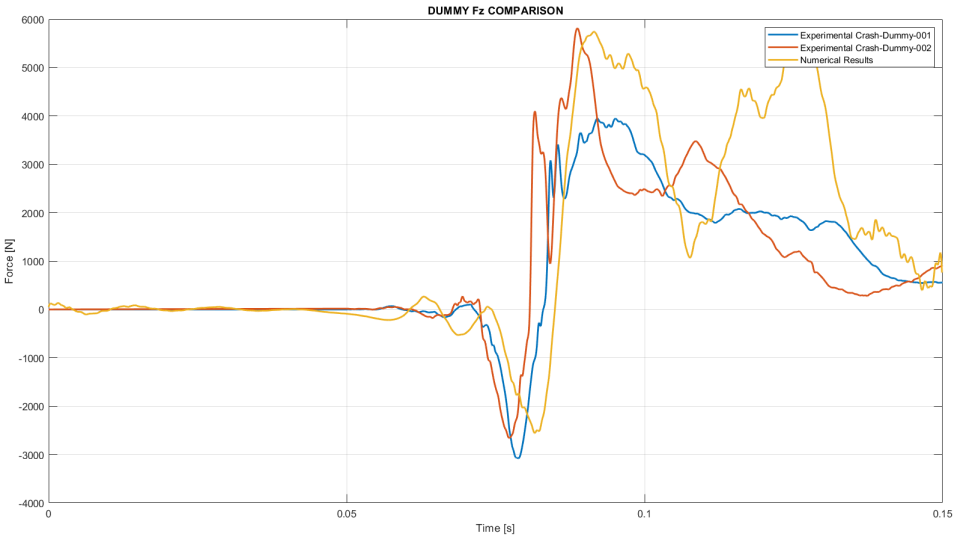

Figure 4.23: Dummy - Helmet F_z comparison

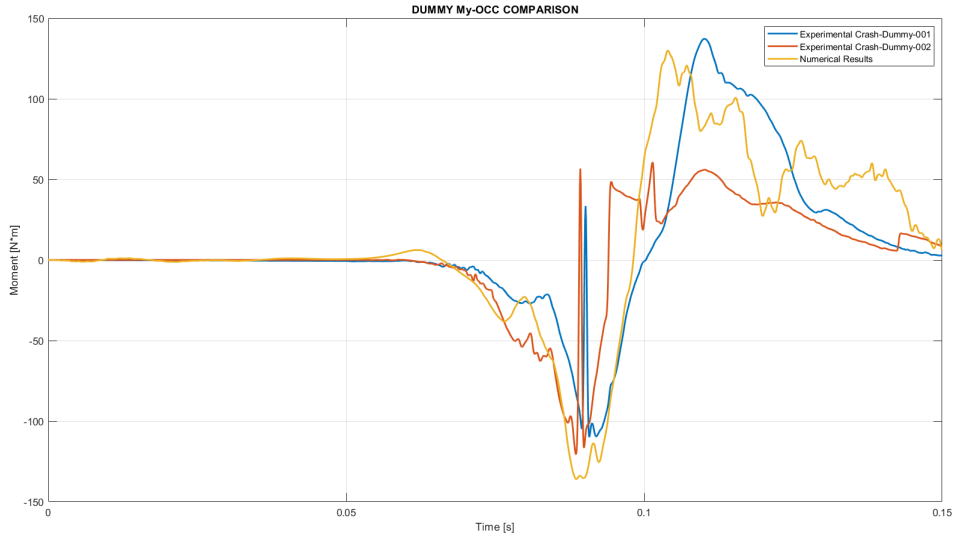

Figure 4.24: Dummy - Helmet M_y comparison

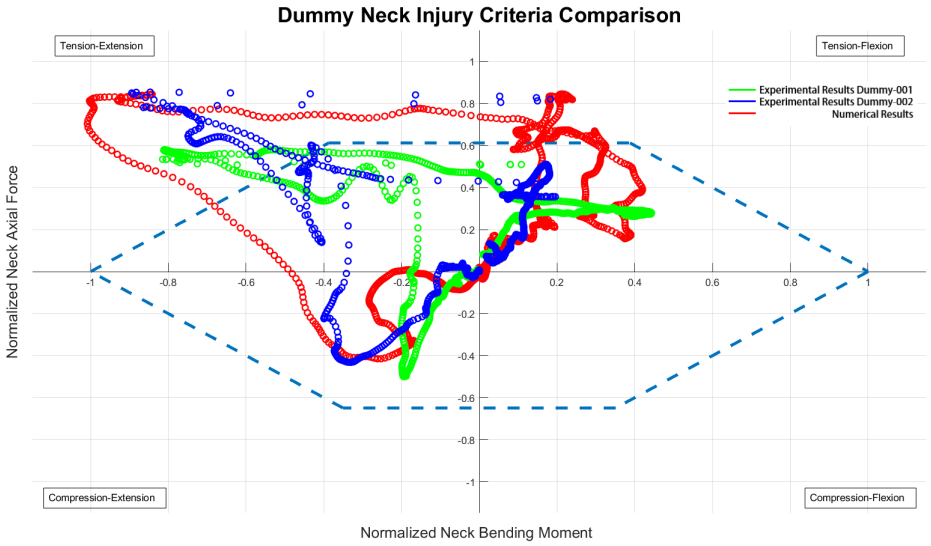

Figure 4.25: Dummy - Helmet N_{ij} comparison

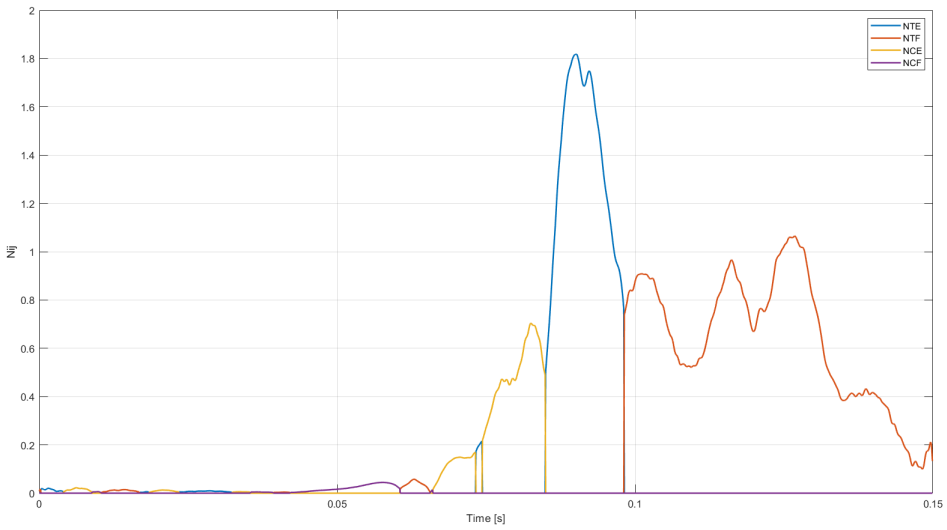

Figure 4.26: Dummy - Helmet N_{ij} vs. time

Graph		Peak value	$err_{\%}$	Peak time (s)	Δerr (s)
Head acceleration (g)	acc_x^{EXP}	/		/	
	acc_x^{NUM}	85.52	/	0.12200	/
	$acc_z^{EXP}+$	95.36		0.08440	
	$acc_z^{NUM}+$	105.75	10.89%	0.09031	0.00591
	$acc_z^{EXP}-$	65.53		0.07808	
	$acc_z^{NUM}-$	42.67	34.88%	0.08240	0.00432
UpperNeck Force (N)	F_x^{EXP}	3305.40		0.09224	
	F_x^{NUM}	4016.10	21.05%	0.09270	0.00046
	$F_z^{EXP}+$	3949.72		0.09208	
	$F_z^{NUM}+$	5745.62	45.47%	0.09150	0.00058
	$F_z^{EXP}-$	3078.33		0.07888	
	$F_z^{NUM}-$	2556.87	16.94%	0.08160	0.00272
Neck $M_{y,OCC}$ ($N{\cdot}m$)	$M_{y,OCC}^{EXP}+$	137.25		0.11024	
	$M_{y,OCC}^{NUM}+$	130.08	5.22%	0.10400	0.00624
	$M_{y,OCC}^{EXP}-$	109.97		0.09080	
	$M_{y,OCC}^{NUM}-$	136.10	23.76%	0.08860	0.00220
Seatbelt Force (N)	$F_{S_{right}}^{EXP}$	8521.82		0.08608	
	$F_{S_{right}}^{NUM}$	8706.46	2.17%	0.08469	0.00139
	$F_{S_{left}}^{EXP}$	9187.59		0.08600	
	$F_{S_{left}}^{NUM}$	9231.56	0.48%	0.08539	0.00061
Neck Injury Criteria	N_{ij}^{EXP}	1.39		0.09200	
	N_{ij}^{NUM}	1.82	30.94%	0.09010	0.00190

Table 4.2: Dummy - Helmet Simulation $err_{\%}$ compared to Dummy - 001 test (3.5.2)

Graph		Peak value	$err_{\%}$	Peak time (s)	Δerr (s)
Head acceleration (g)	acc_x^{EXP}	87.61		0.08896	
	acc_x^{NUM}	85.52	2.39%	0.12200	0.03304
	$acc_z^{EXP}+$	130.25		0.08152	
	$acc_z^{NUM}+$	105.75	18.81%	0.09031	0.00879
	$acc_z^{EXP}-$	55.84		0.076400	
	$acc_z^{NUM}-$	42.67	23.59%	0.08240	0.00600
UpperNeck Force (N)	F_x^{EXP}	4481.86		0.08888	
	F_x^{NUM}	4016.10	10.39%	0.09270	0.00382
	$F_z^{EXP}+$	5814.12		0.08872	
	$F_z^{NUM}+$	5745.62	1.18%	0.09150	0.00278
	$F_z^{EXP}-$	2658.15		0.07728	
	$F_z^{NUM}-$	2556.87	3.81%	0.08160	0.00432
Neck $M_{y,OCC}$ ($N{\cdot}m$)	$M_{y,OCC}^{EXP}+$	60.60		0.10144	
	$M_{y,OCC}^{NUM}+$	130.08	114.65%	0.10400	0.00256
	$M_{y,OCC}^{EXP}-$	120.70		0.08856	
	$M_{y,OCC}^{NUM}-$	136.10	12.76%	0.08860	0.00004
Seatbelt Force (N)	$F_{S_{right}}^{EXP}$	9572.50		0.08232	
	$F_{S_{right}}^{NUM}$	8706.46	9.05%	0.08469	0.00237
	$F_{S_{left}}^{EXP}$	9404.07		0.08448	
	$F_{S_{left}}^{NUM}$	9231.56	1.83%	0.08539	0.00091
Neck Injury Criteria	N_{ij}^{EXP}	1.75		0.08856	
	N_{ij}^{NUM}	1.82	4%	0.09010	0.00154

Table 4.3: Dummy - Helmet Simulation $err_{\%}$ compared to Dummy - 002 test (3.5.2)

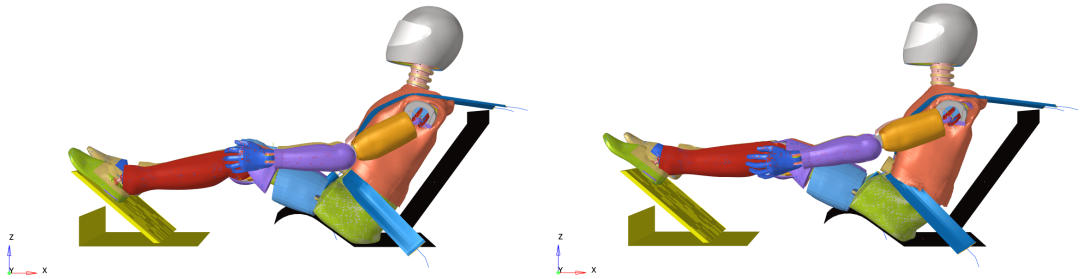

(a) t = 0.080 s (b) t = 0.085 s

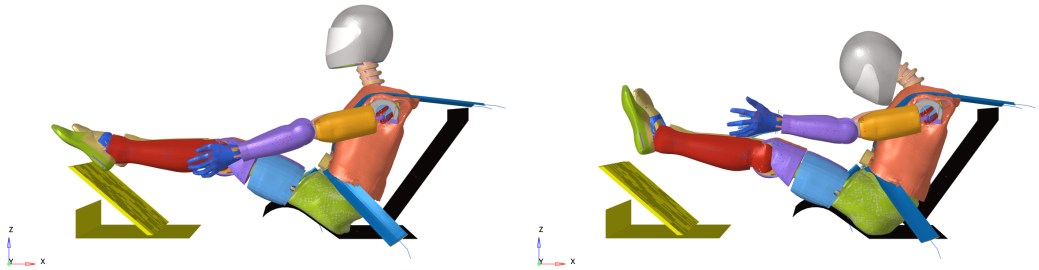

(c) t = 0.090 s (d) t = 0.100 s

Figure 4.27: Dummy - Helmet Simulation Peak Frames

4.2.3 Dummy with HANS device

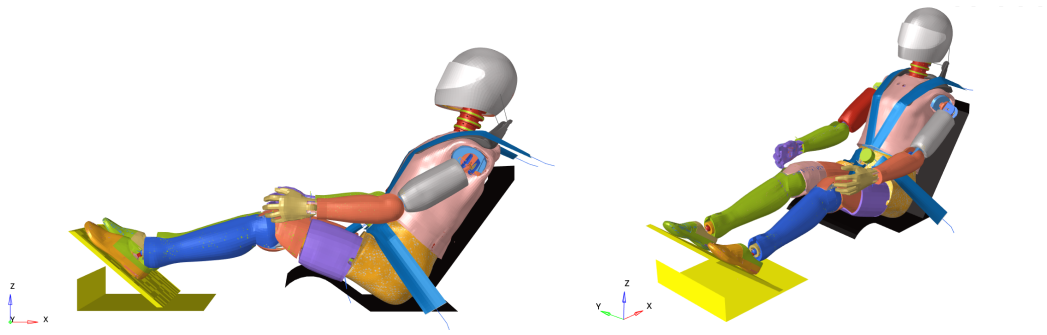

Figure 4.28: Dummy with HANS simulation initial configuration

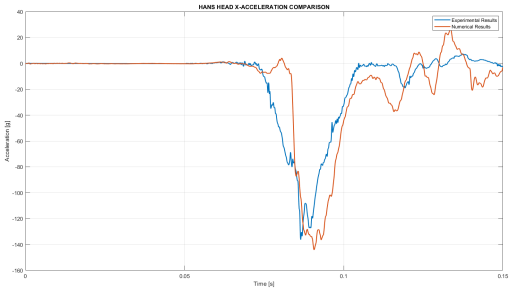

(a) Head x-acceleration

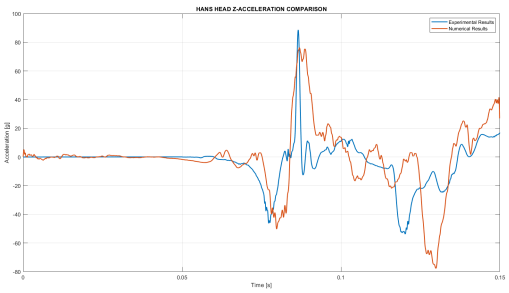

(b) Head z-acceleration

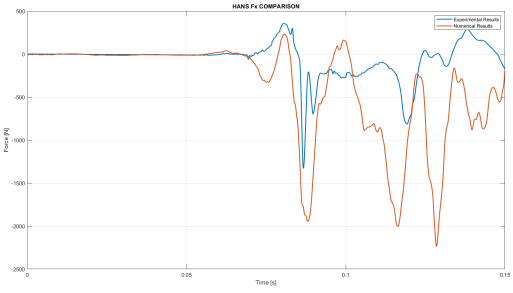

(c) F_x

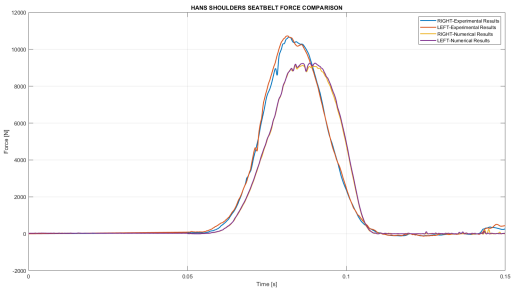

(d) Seatbelt force

Figure 4.29: Dummy with HANS simulation output data comparison

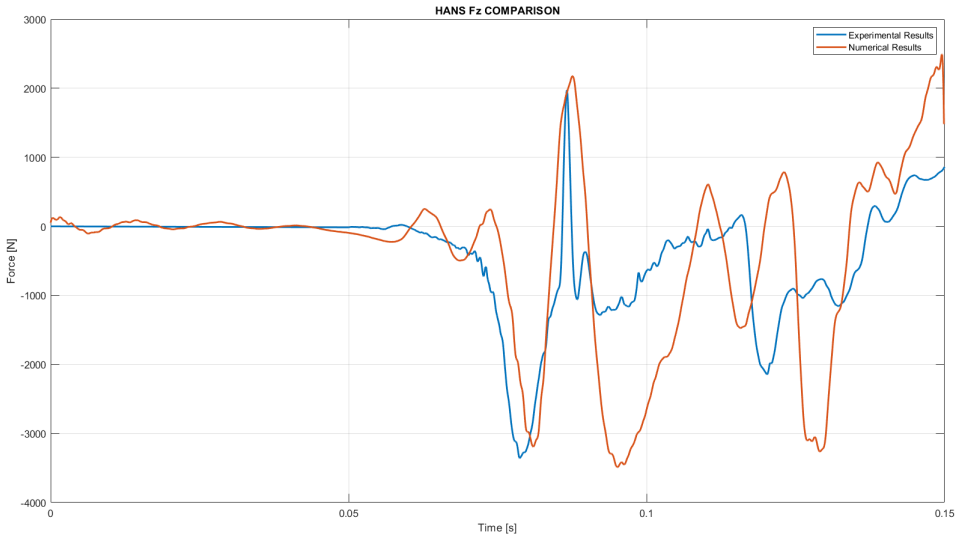

Figure 4.30: Dummy with HANS F_z comparison

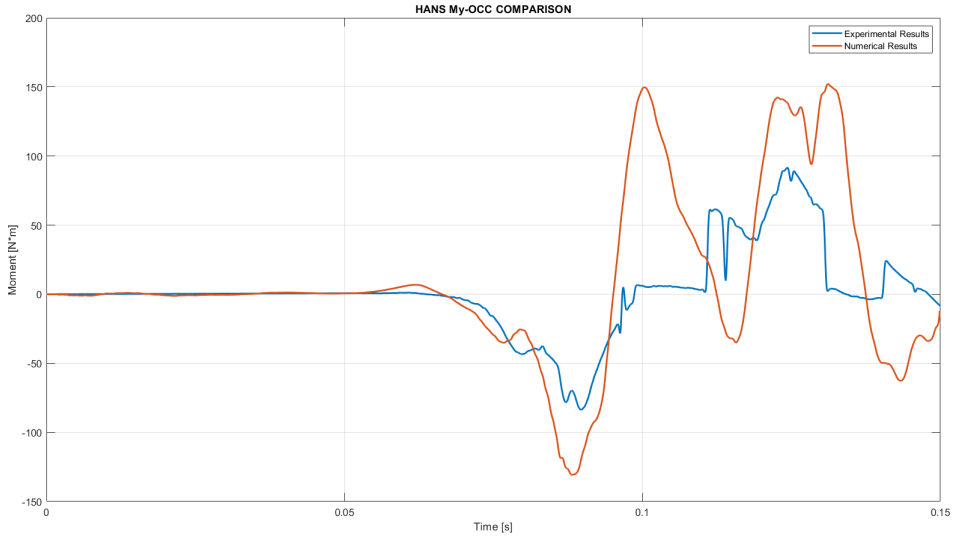

Figure 4.31: Dummy with HANS M_y comparison

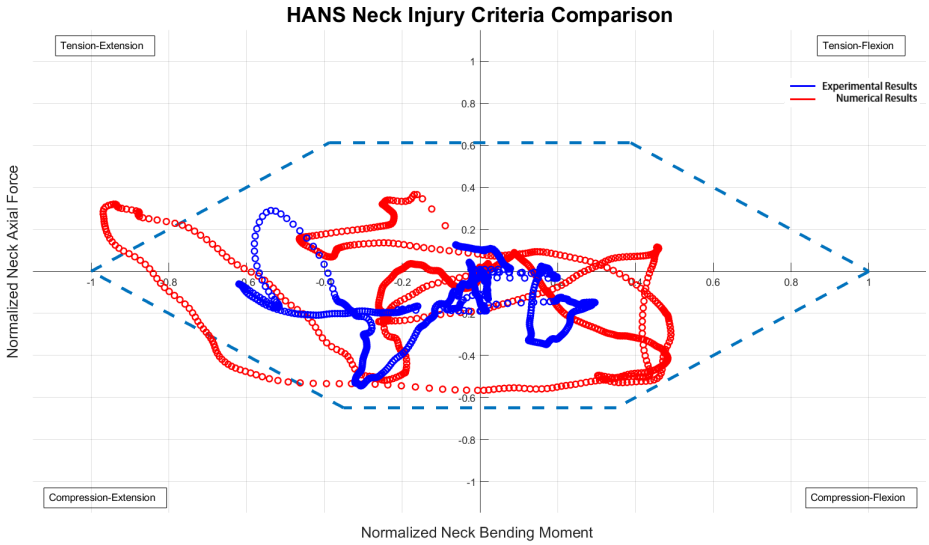

Figure 4.32: Dummy with HANS N_{ij} comparison

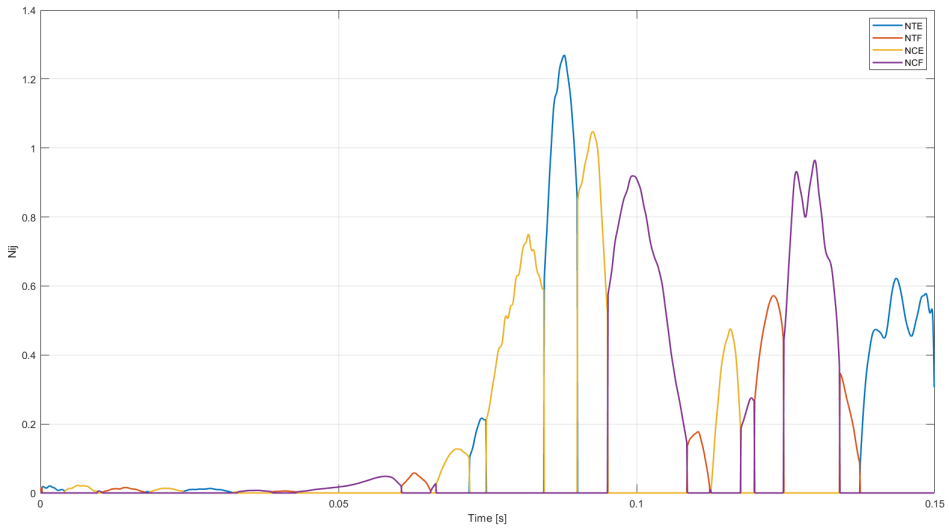

Figure 4.33: Dummy with HANS N_{ij} vs. time

Graph		Peak value	$err_{\%}$	Peak time (s)	Δerr (s)
Head acceleration (g)	acc_x^{EXP}	136.30		0.08648	
	acc_x^{NUM}	144.16	5.77%	0.09070	0.00422
	$acc_z^{EXP}+$	88.69		0.08656	
	$acc_z^{NUM}+$	76.38	13.87%	0.08690	0.00034
	$acc_z^{EXP}-$	53.76		0.12024	
	$acc_z^{NUM}-$	77.69	44.51%	0.12990	0.00966
UpperNeck Force (N)	F_x^{EXP}	1330.15		0.08672	
	F_x^{NUM}	2237.00	68.17%	0.12850	0.04178
	$F_z^{EXP}+$	1971.09		0.08664	
	$F_z^{NUM}+$	2177.07	10.45%	0.08760	0.00096
	$F_z^{EXP}-$	3356.90		0.07872	
	$F_z^{NUM}-$	3487.48	3.89%	0.09510	0.01638
Neck $M_{y,OCC}$ ($N{\cdot}m$)	$M_{y,OCC}^{EXP}+$	91.69		0.12432	
	$M_{y,OCC}^{NUM}+$	152.14	65.93%	0.13110	0.00678
	$M_{y,OCC}^{EXP}-$	83.63		0.08976	
	$M_{y,OCC}^{NUM}-$	130.76	56.36%	0.08810	0.00166
Seatbelt Force (N)	$F_{S_{right}}^{EXP}$	10655.60		0.08192	
	$F_{S_{right}}^{NUM}$	9142.86	14.19%	0.08385	0.00193
	$F_{S_{left}}^{EXP}$	10722.70		0.08160	
	$F_{S_{left}}^{NUM}$	9246.11	13.77%	0.09029	0.00869
Neck Injury Criteria	N_{ij}^{EXP}	0.83		0.08672	
	N_{ij}^{NUM}	1.25	50.60%	0.08770	0.00098

Table 4.4: Dummy with HANS Simulation $err_{\%}$

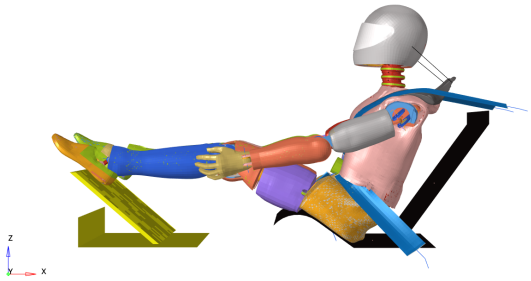

(a) t = 0.085 s

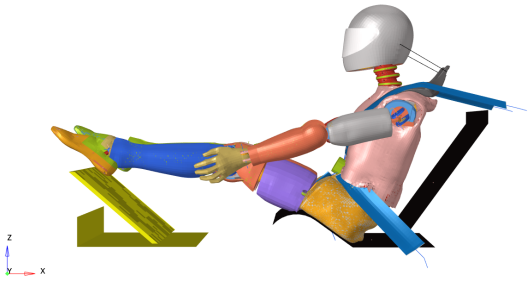

(b) t = 0.090 s

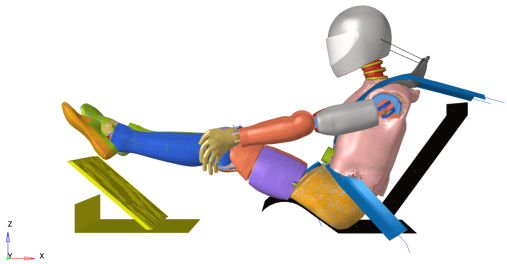

(c) t = 0.095 s

(d) t = 0.130 s

Figure 4.34: Dummy with HANS Simulation Peak Frames

4.2.4 Dummy with Hybrid PRO device

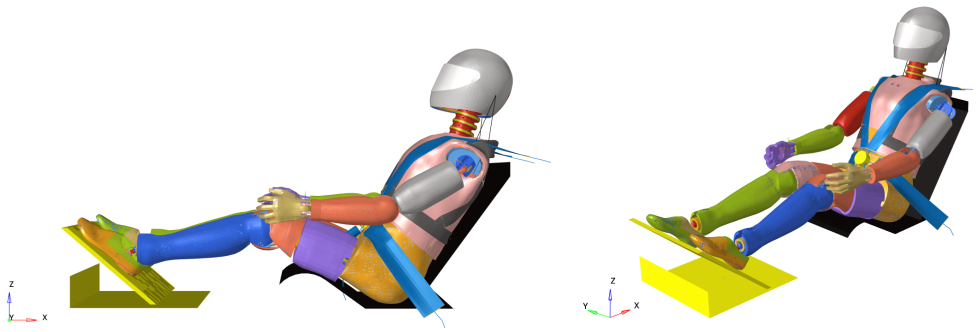

Figure 4.35: Dummy with Hybrid PRO simulation initial configuration

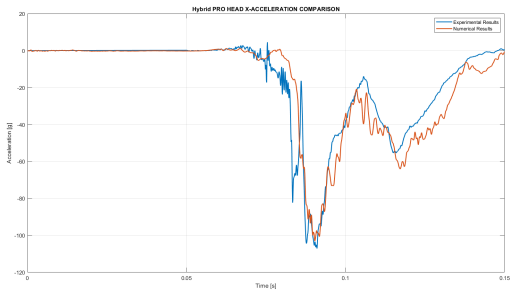

(a) Head x-acceleration

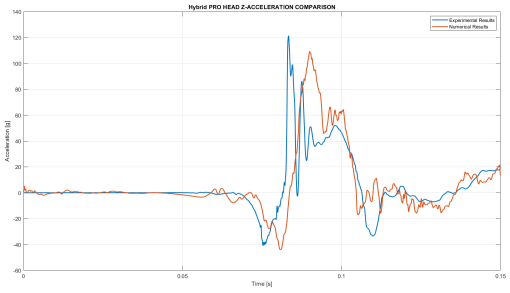

(b) Head z-acceleration

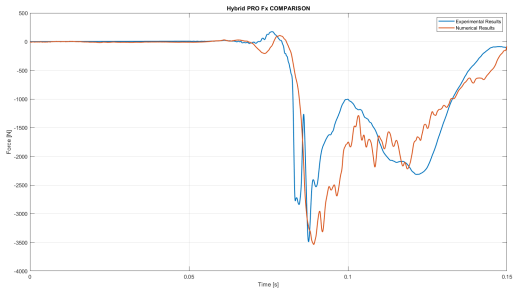

(c) F_x

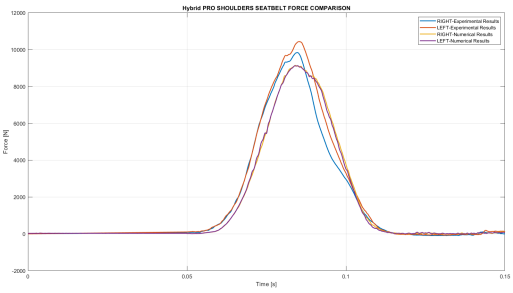

(d) Seatbelt force

Figure 4.36: Dummy with Hybrid PRO simulation output data comparison

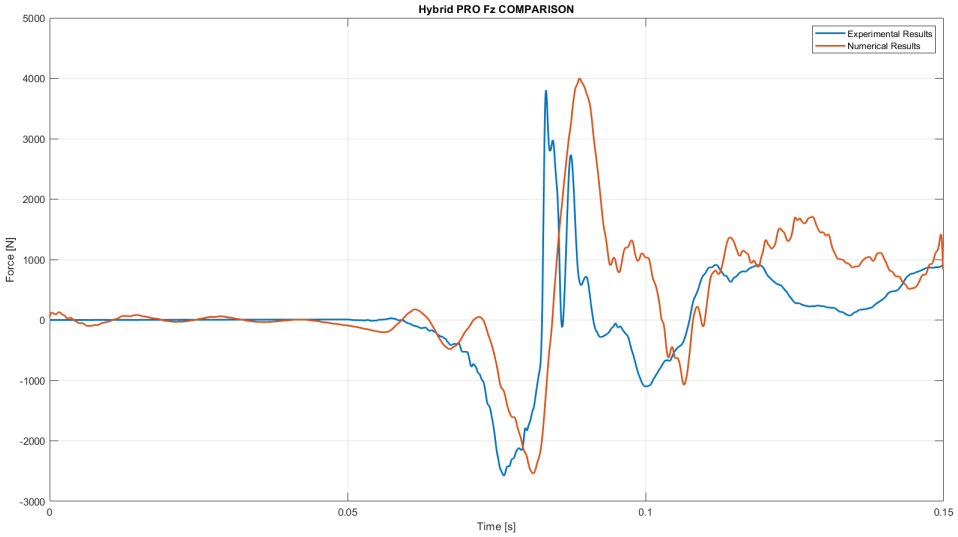

Figure 4.37: Dummy with Hybrid PRO F_z comparison

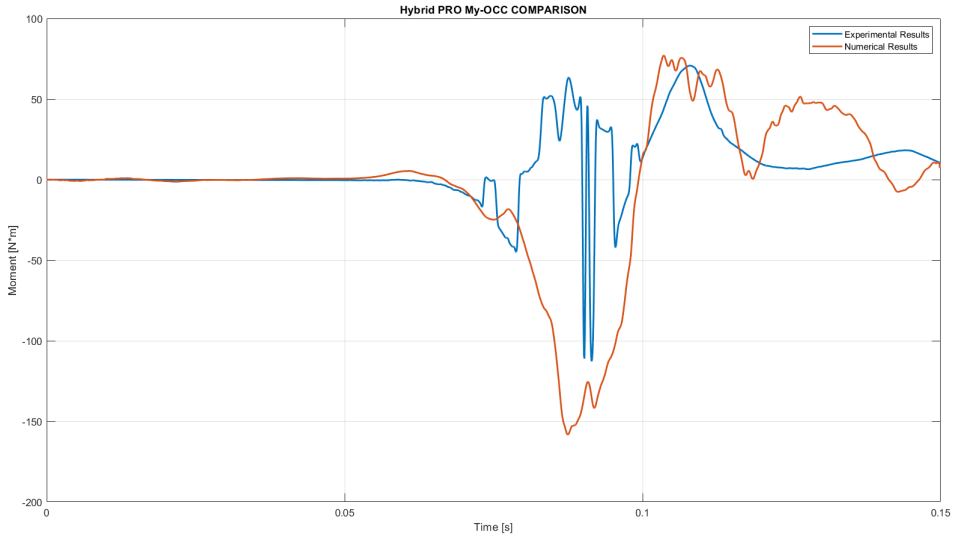

Figure 4.38: Dummy with Hybrid PRO M_y comparison

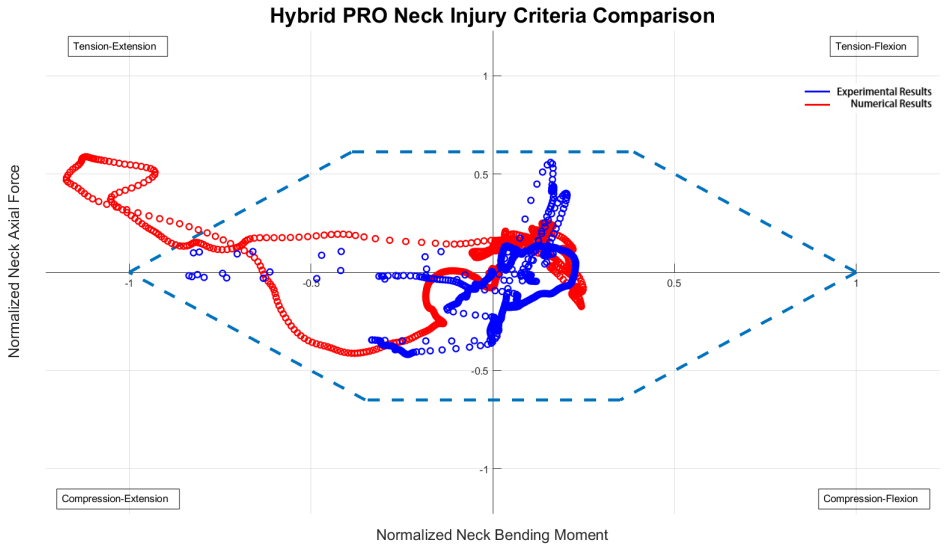

Figure 4.39: Dummy with Hybrid PRO N_{ij} comparison

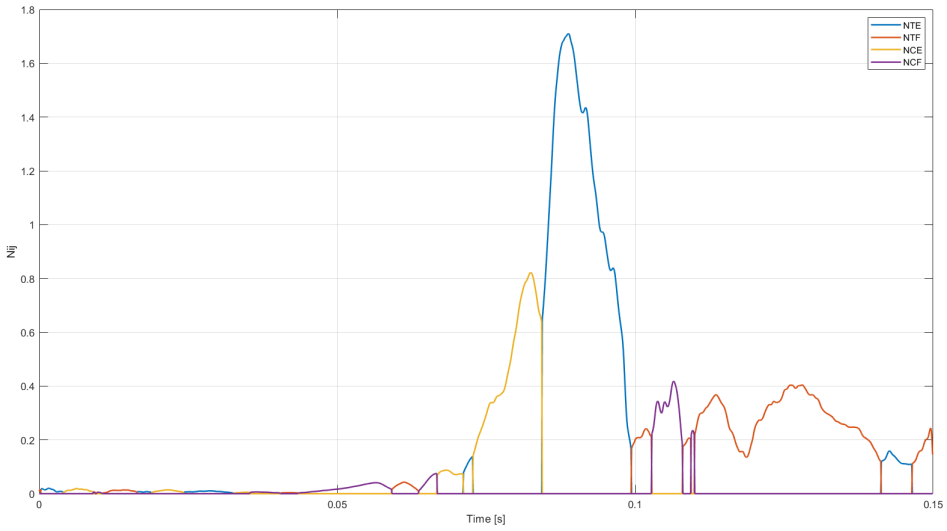

Figure 4.40: Dummy with Hybrid PRO N_{ij} vs. time

Graph		Peak value	$err_{\%}$	Peak time (s)	Δerr (s)
Head acceleration (g)	acc_x^{EXP}	107.11		0.09104	
	acc_x^{NUM}	102.90	3.93%	0.09040	0.00064
	$acc_z^{EXP}+$	121.46		0.08336	
	$acc_z^{NUM}+$	109.44	9.89%	0.09000	0.00664
	$acc_z^{EXP}-$	40.97		0.07528	
	$acc_z^{NUM}-$	43.96	7.29%	0.08100	0.00572
UpperNeck Force (N)	F_x^{EXP}	3493.12		0.08760	
	F_x^{NUM}	3539.49	1.33%	0.08920	0.00160
	$F_z^{EXP}+$	3803.17		0.08328	
	$F_z^{NUM}+$	4000.89	5.20%	0.08890	0.00562
	$F_z^{EXP}-$	2573.96		0.07616	
	$F_z^{NUM}-$	2538.75	1.36%	0.08110	0.00494
Neck $M_{y,OCC}$ ($N{\cdot}m$)	$M_{y,OCC}^{EXP}+$	70.74		0.10800	
	$M_{y,OCC}^{NUM}+$	77.08	8.96%	0.10350	0.00450
	$M_{y,OCC}^{EXP}-$	112.78		0.09144	
	$M_{y,OCC}^{NUM}-$	158.29	40.35%	0.08740	0.00404
Seatbelt Force (N)	$F_{S_{right}}^{EXP}$	9835.26		0.08472	
	$F_{S_{right}}^{NUM}$	9125.73	7.21%	0.08483	0.00011
	$F_{S_{left}}^{EXP}$	10427.80		0.08536	
	$F_{S_{left}}^{NUM}$	9142.91	12.32%	0.08413	0.00123
Neck Injury Criteria	N_{ij}^{EXP}	0.92		0.09024	
	N_{ij}^{NUM}	1.71	85.87%	0.08891	0.00133

Table 4.5: Dummy with Hybrid PRO Simulation $err_{\%}$

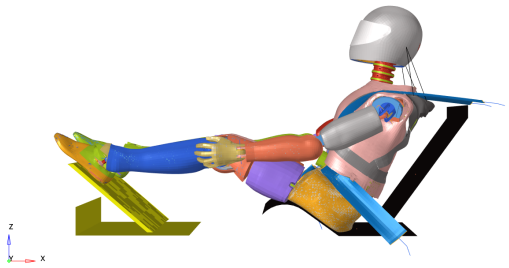

(a) t = 0.080 s

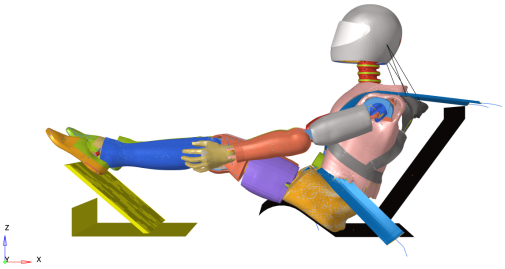

(b) t = 0.085 s

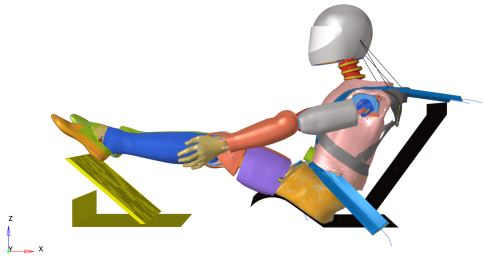

(c) t = 0.090 s

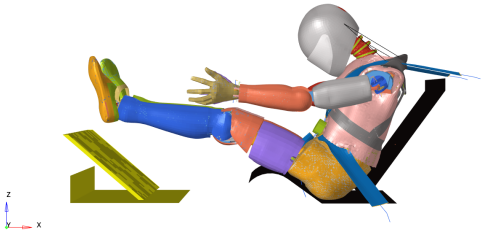

(d) t = 0.105 s

Figure 4.41: Dummy with Hybrid PRO Simulation Peak Frames

4.3 Hybrid III model validation conclusions

From the data showed in the previous section, we can say that the results are satisfactory. All the numerical data follow the same trend of the experimental ones, and they have the same order of magnitude. The biggest errors are for the M_y, this also due to the neck-moment acquisition problems that we had with the neck-loadcell during the experimental tests. As said in Chapter 3.5 these problems caused the loss of M_y signal during the tests, thus leading us to probably have lower M_y acquired values than the real ones. But other than that, we can see that the numerical M_y values are always greater than the experimental ones. We can conclude that regarding the N_{ij}, the numerical models are more conservative. Instead, the neck axial force F_z is very well reproduced in each test, both the compression and tension peaks. But the differences in M_y led us to have errors also in the N_{ij}. This because, as we have seen in the experimental tests, the most critical situation is the tension-extension, caused by the combination or the closeness of the M_y extension peak and F_z tension peak. Since in the numerical simulations we have higher bending moment values, also the numerical N_{ij} peaks increased. In Figure 4.42 is possible to see the comparison between all the numerical and experimental N_{ij} plots.

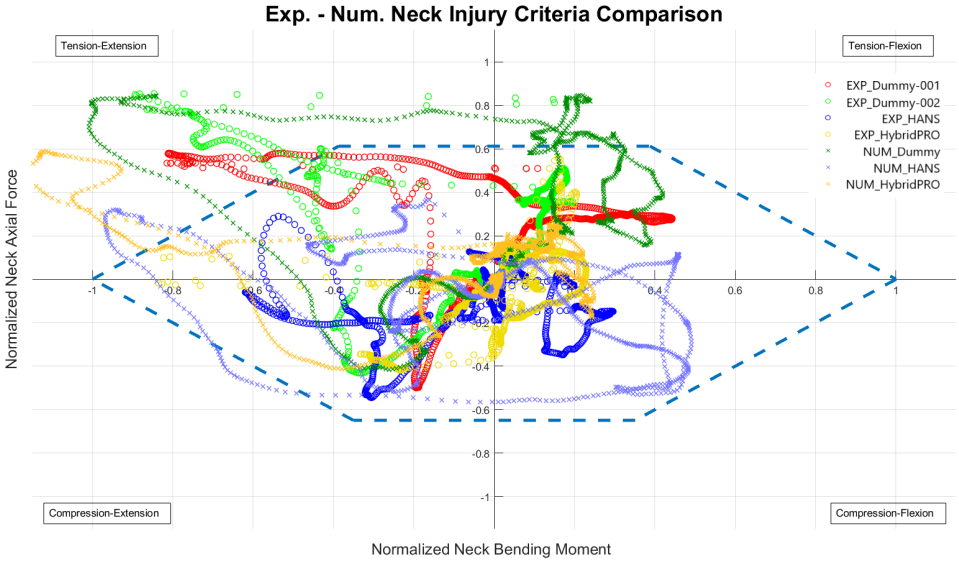

Figure 4.42: Experimental - Numerical N_{ij} comparison

Compared to experimental tests, in numerical simulations also with the FHR devices the N_{ij} values go out from the hexagon limit-box. This situation is only caused by the M_y extension moment, in fact we can see that we never reach the tension limit but we overcome the moment extension limit, thus going out the limit-box. Instead in the simulations without the FHR devices we can see that also the tension limit is overcomed. Therefore the FHR devices helped to reduce the neck tension axial force, as in the experimental tests, but they

could not reduce the extension peaks. In these type of tests, achieving a reduction in the extension peaks for the FHR devices was difficult also due to the tether-helmet attachement points that were behind the neck axis.
Another interesting thing to see is that in the HANS numerical simulation the FHR reduced the neck axial tension force, but to do this it caused a high compression peak that combined with the extension moment made the N_{ij} overcome the hexagon limit-box. The x and z head accelerations are well reproduced too, meaning that the dummy's head moved in the same way of the experimental tests. The average error for the seatbelt force is 7.096% respect to experimental data. This is a very good result for the seatbelt modeling and the seatbelt's material characterization.

Chapter 5

THUMS' numerical simulations

This chapter describes the method used to perform the THUMS' setup and the analysis run, after having validated the Hybrid III FE model. In particular, in the first part the process of positioning, FHRs fitting, the instrumentation implementation and the prescribed motions are explained. Then, the obtained data are discussed and compared.

5.1 THUMS' numerical model setup

Now that the Hybrid III model has been validated, it is possible to use the sled seat setup for running FEA on THUMS, and then confront the obtained results. Of course, as described in Chapter 2, the two FE models are very different from one another, therefore some modification to seatbelts and other parts are necessary to fit the THUMS into the sled seat while maintaining the same geometry.

5.1.1 THUMS' positioning

The positioning of THUMS is different from the Hybrid III one. Due to the complexity of the THUMS LS-DYNA model, simulation based positioning is required. PRIMER contains tools that help to set up simulations to position an occupant by running a model in LS-DYNA. From the PRIMER V17.0 there is a tool similar to the one for the Hybrid III, that permits the movement of the model sub-assemblies, but still a simulation based positioning is required. The Figure 5.1 describes the steps for setting up an LS-DYNA model in PRIMER that will position the THUMS model to a specified target position.

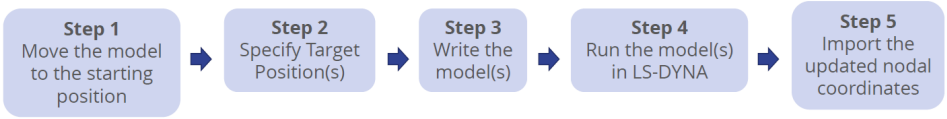

Figure 5.1: THUMS positioning steps

The analysis were performed without the helmet, the seatbelts and sled seat (they have

been added and fitted once the positioning was completed). The first step was to move the model to our desired starting position. This was the starting position at the start of the positioning analysis. Then we specified the target end position, following the Hybrid III model dummy position. Once the model has been created it could be written from PRIMER and run in LS-DYNA. PRIMER had automatically created cables that pulled the THUMS model into the specified target position during the LS-DYNA analysis. After the analysis has finished, the final nodes positions have been exported from the LS-DYNA analysis, and imported in the FE THUMS model.

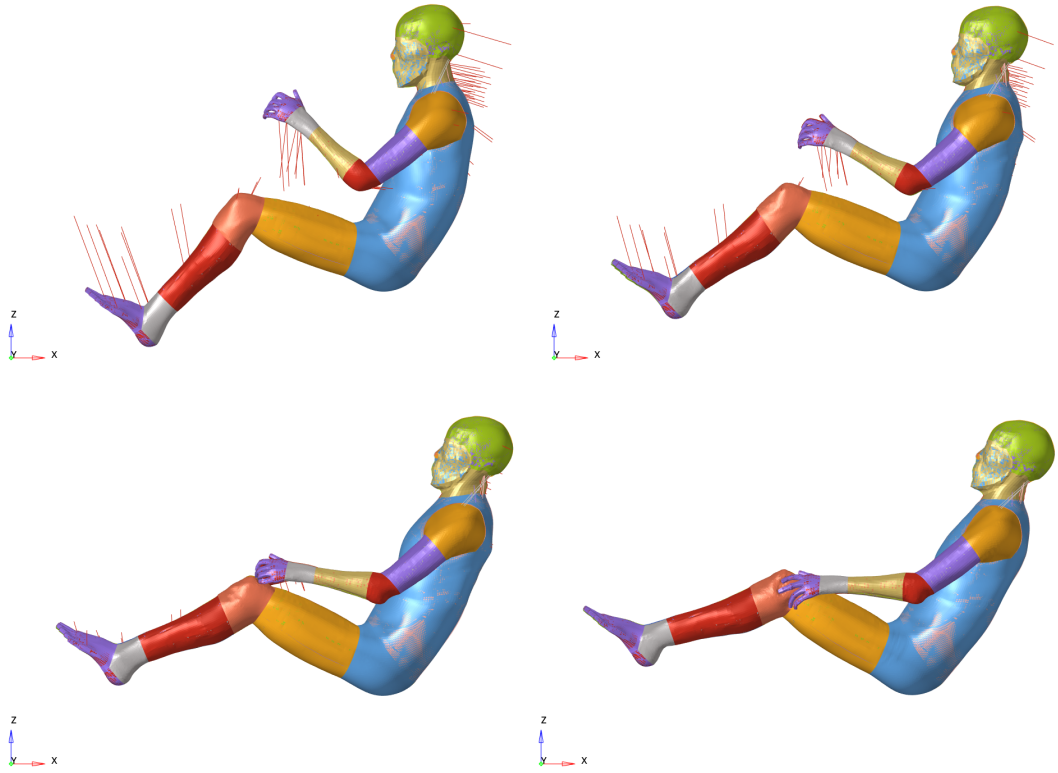

Figure 5.2: THUMS positioning analysis frames

Once the THUMS is correctly positioned, the seatbelts, the helmet and the seat sled were re-inserted in the model. The helmet and the seat sled were the same used for the Hybrid III model. Since the THUMS and Hybrid III models are very different from one another, the seatbelts have been necessarily re-fitted. The same Hybrid III seatbelts attachement points, dimensions and properties, described in Chapter 4.1.4, have been used. In Figure 5.3, the comparison between the THUMS (in red) and Hybrid III (in blue) positions is showed.

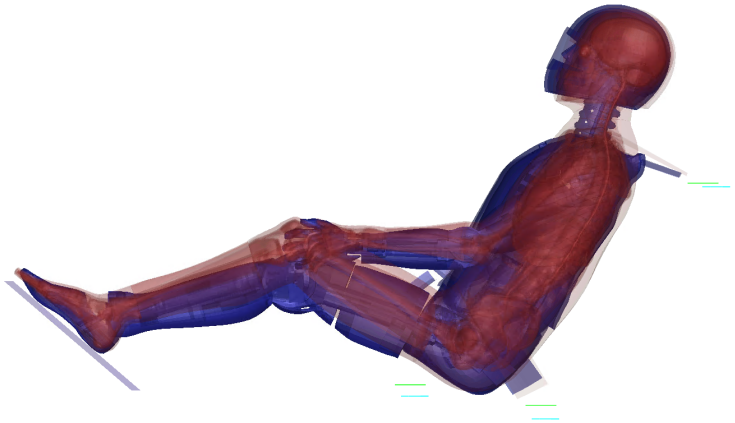

Figure 5.3: THUMS and Hybrid III positions comparison

5.1.2 Cross-sections definition

Because THUMS is a HBM, it is not provided of any type of instrumentation. Therefore cross-sections have to be implemented and some nodes representing important points have to be defined in the output properties. In this work, we implemented several cross-sections in the cervical vertebrae, and defined several nodes representing each cervical vertebrae (showed in Chapter 6.2).

We could define an upper neck cross section also in the THUMS model, but its loads could not be comparable with the Hybrid III upper neck loads due to the differences between the neck models. THUMS' neck section is made of bones, ligaments and other tissue, hence its formulation is way different from the Hybrid III neck that is made of steel and rubber. For this reason it was more interesting to evaluate force and moments inside each vertebra and understand how they change. Fourteen plane cross-sections (see Chapter 4.1.5), two per cervical vertebra, were defined in the THUMS to find the z-axial forces and y-bending moments in each vertebra. The features of each cross-section, which have been studied in another MSc thesis [6], were given by FIA. But since the THUMS in that work was in another position, we had to redo manually all the cross-sections, respecting the position, shape, area and moment of inertia. The cross-sections of each vertebra were defined in two different ways, and so they differ in inclination and section cut height. The modality of definition were:

- section perpendicular to the spinal cord, that maximize the cross-section surface; these have been used to evaluate the z-axial forces parallel to the spinal cordal.

- section plane that cuts through the vertebra's spinous process and maximize the I_{yy}, that can be defined as the indicator of a section's ability to resist to bending moment; these have been used to study the y-bending moments.

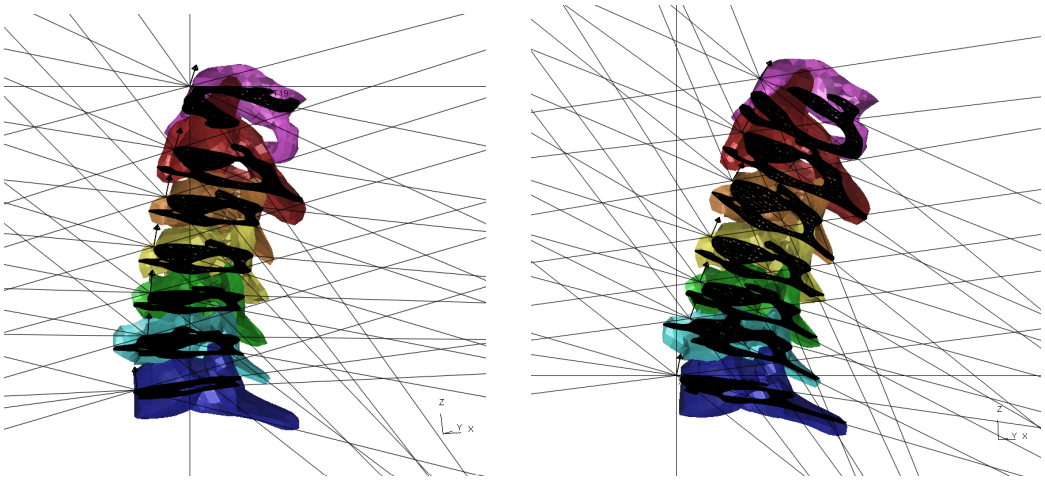

(a) Perpendicular sections (b) Oblique sections

Figure 5.4: THUMS cervical vertebrae cross-sections

Obviously, two reference systems per vertebra (one for each section type) have been defined in order to correctly evaluates the loads in each section. The x axis is directed toward the spinous process of the vertebra and the z axis is directed toward the head (the direction differs accordingly to the section inclination).

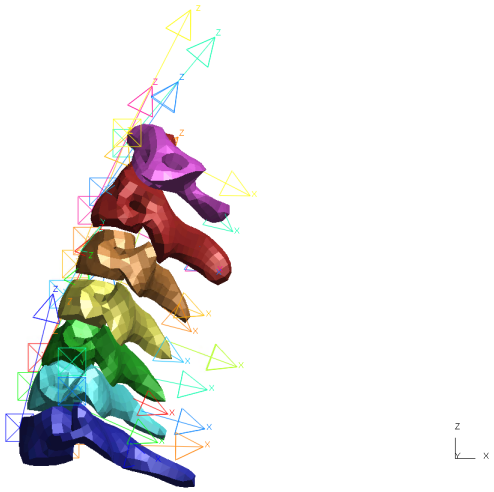

Figure 5.5: Cross-sections reference systems

5.1.3 Crash pulse

Also for the THUMS models the same measured experimental deceleration profiles have been used, as in the Hybrid III model (see Chapter 4.1.2). The same approach of the Hybrid III FE model have been used (Chapter 4.1.2), decreasing the heaviness of the calculations. The crash pulse is provided by prescribing for each test the correct acquired acceleration profile on the sled's foot floor, by using the LS-DYNA card PRESCRIBED_MOTION [33].

In this case, the initial period of adjustment was increased to 70 *ms,* to let the THUMS correctly lean against the seat and to have a good fitting of the FHR devices. In Figure 5.6, it's possible to see that at 0.070 *s* the reaction force between the THUMS and the seat reaches a value of approximately 700 *N*, that is coherent with the THUMS weight.

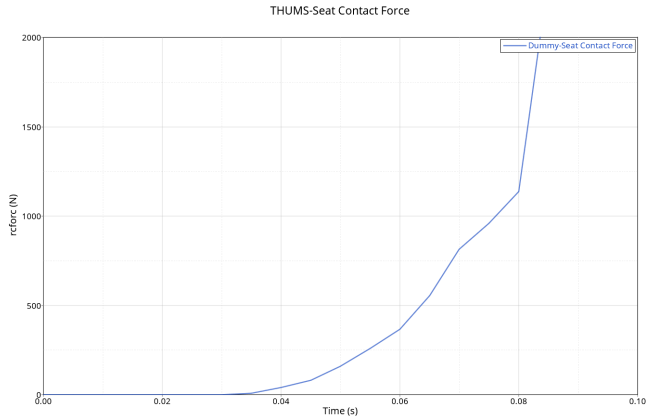

Figure 5.6: THUMS-seat contact force

Also the termination time has been increased, to be sure of having acquired all the force and moment peaks. In this case the simulation continued until the total time left was *270 ms* (hence the CONTROL_TERMINATION [33] card was set to 0.27).

Since in the THUMS model there were no rigid parts in the feet, to reproduce the initial F_z compression peak in this case we gave to the node sets of the feet a PRESCRIBED_MOTION [33] with the same acceleration crash pulse given to the sled's foot floor for each test. In this way the feet moved with the same acceleration profile of the footrest, as they were constrained on it. The same *death_times* used with the Hybrid III models have been used.

5.1.4 FHR devices

With the THUMS model it was not necessary to perform fitting simulations with both the HANS and Hybrid PRO devices. This because these devices have a shape optimized for a real human body, and since the THUMS is a HBM they could be easily positioned on it. During the first 70 *ms* of adjustment, thanks to the shoulders seatbelts the FHR devices went perfectly in contact with the THUMS' shoulders, as showed in Figure 5.7.

To be consistent with the validated Hybrid III model, all the features and parameters releated to the FHR devices have been kept the same. It has been used the same helmet's connection point on the same helmet FE model, and the same tethers' slack lenghts. Since the THUMS' neck is shorter and the chest is higher respect to the Hybrid III, the tethers initial lengths were different as shown in Table 5.1.

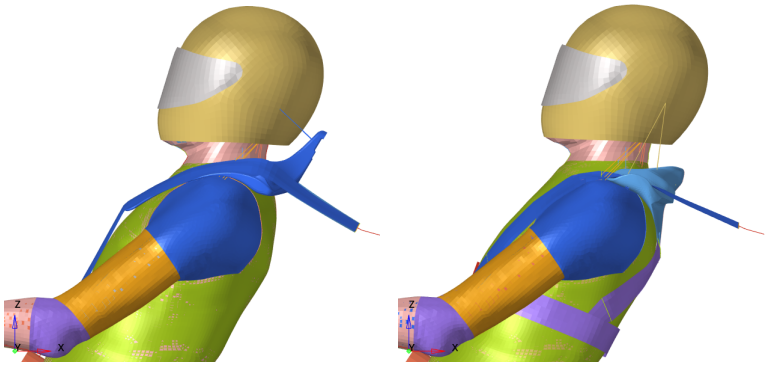

Figure 5.7: FHR's fitting

Tethers' lenght	Hybrid III	THUMS
HANS tether [*mm*]	111.8	75.2
Hybrid PRO front tether [*mm*]	172.9	127.8
Hybrid PRO rear tether [*mm*]	149.9	96.7

Table 5.1: Tethers initial lenghts differences

5.2 THUMS numerical simulations results

In this section, we discuss the THUMS numerical simulations results, in terms of vertebrae F_z axial force and M_y bending moment. The signs of the plotted data showed in this section, are all inherent with the positive directions of neck forces and moments illustrated in Fig.3.15. Therfore, we consider positives tension forces and flexion moments. For each numerical simulation we show the comparison plots between the seven vertebrae, from C1 to C7. The F_z axial forces have been measured on the perpendicular vertebrae cross-sections, instead the M_y bending moments on the oblique cross-sections (see Section 5.1.2). All the numerical raw data results have been filtered with the same type of filter and the frequency response classes used for the experimental tests, showed in Chapter 3.5. To have the numerical animations, BINARY_D3PLOTs [33] with a DT = 0.010 *s* have been set as output.

5.2.1 THUMS with helmet

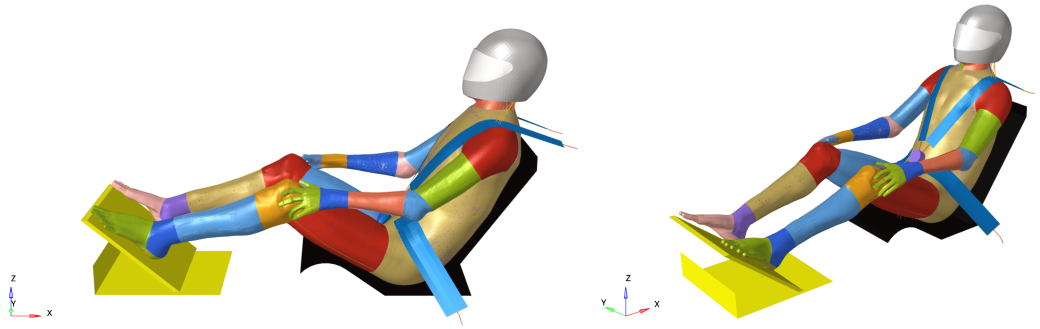

Figure 5.8: THUMS with helmet initial configuration

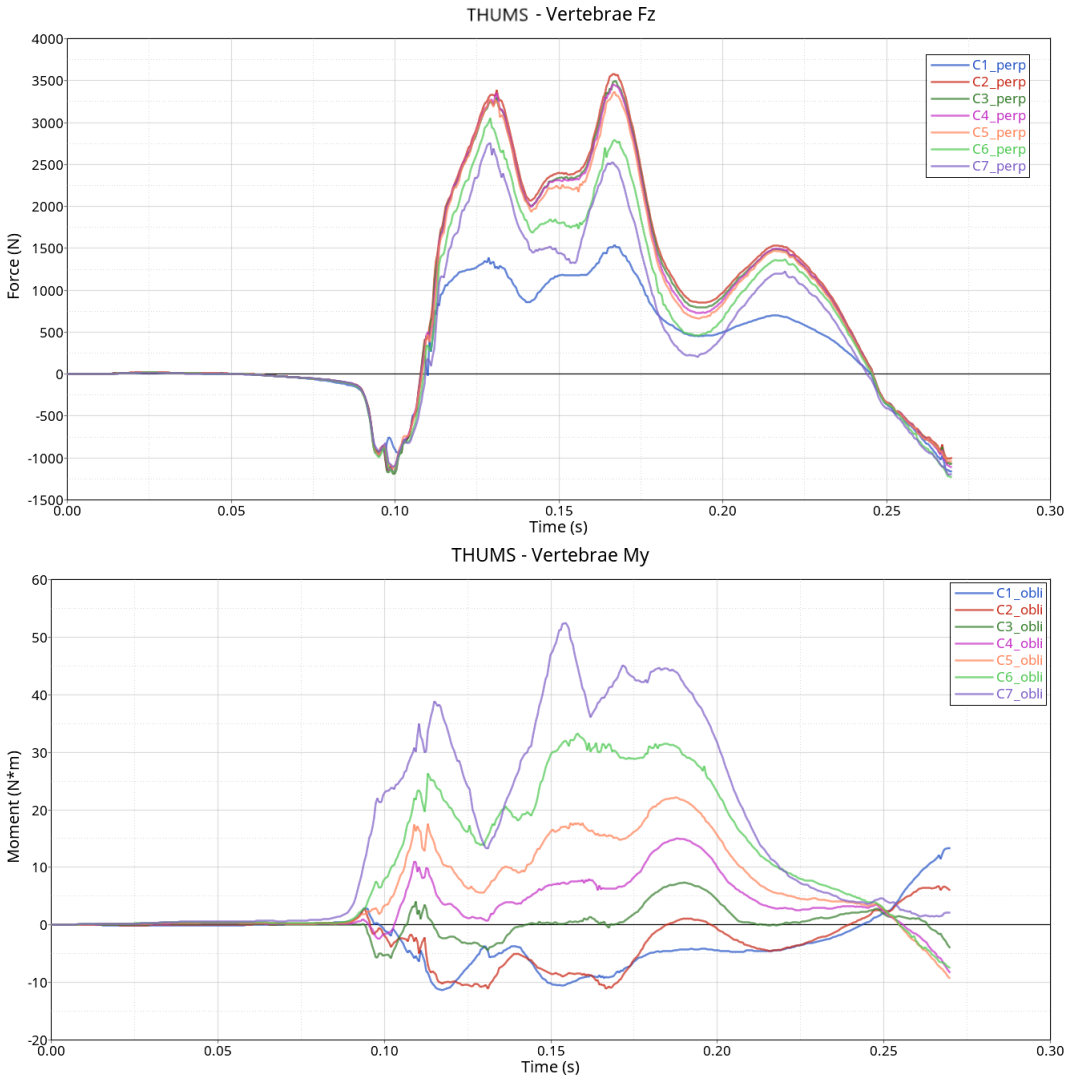

Figure 5.9: THUMS with helmet simulation output data

Looking at the F_z vertebrae forces in Figure 5.9, we can see that all the vertebrae have an initial similar compression peak after 30 *ms* of the crash pulse beginning. as it happened in the Hybrid III model. Then the vertebrae from C2 to C5 follow the same F_z tension profile, with a first peak around 130 *ms* and another higher peak around 170 *ms*. It is possible to notice, with C6 and C7, that the tension force peaks tend to decrease when the distance from the head increases. Instead, C1 does not follow the aforementioned trend but is the least loaded vertebra. Force peaks are all at the same istants. We can say that the forces' trend is similar to that seen in the Hybrid III Dummy simulation (Figure 4.23) but with different peak values and times. Regarding the moment M_y, we can see curves that are initially loaded mainly with extension moments in the first vertebrae (C1-C2), C3 that has a extension-flexion load and then starting from C4 the vertebrae are loaded with flexion moments. In this case we do not have similar values and trend as for F_z, but the most loaded vertebrae are the ones furthest from the head. For this reason we can not make any comparison with the Hybrid III M_y, that has a single extension-flexion trend representative of how its *beam-neck* it is made.

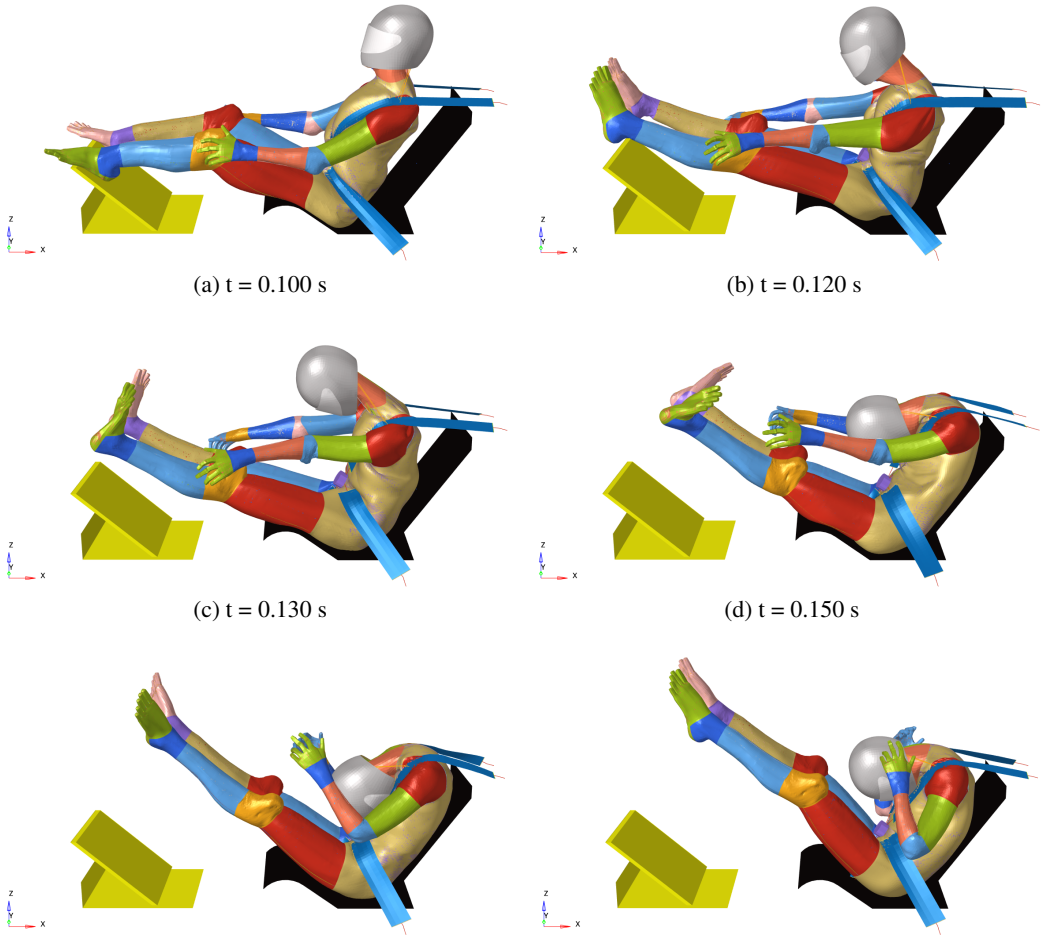

(a) t = 0.100 s (b) t = 0.120 s

(c) t = 0.130 s (d) t = 0.150 s

(e) t = 0.170 s (f) t = 0.190 s

Figure 5.10: THUMS with helmet simulation frames

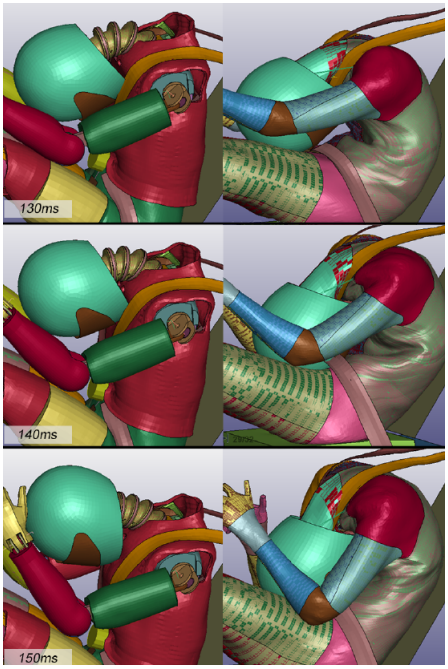

Figure 5.11: Comparison between the THUMS and Hybrid III head motion

Both the THUMS F_z and M_y peaks happen at higher time istants respect to the Hybrid III ones. This indicates that probably the kinematic of the THUMS' neck and head is more damped than the Hybrid III one. This behaviour can be visualized by looking at the last simulation instant in both the numerical analysis. Figure 5.11 show a comparison between the head movements of the two models and is possible to notice that Hybrid III head has finished the forward rotation motion and is returning back, meanwhile the THUMS neck has not reached the end of its rotation.

5.2.2 THUMS with HANS device

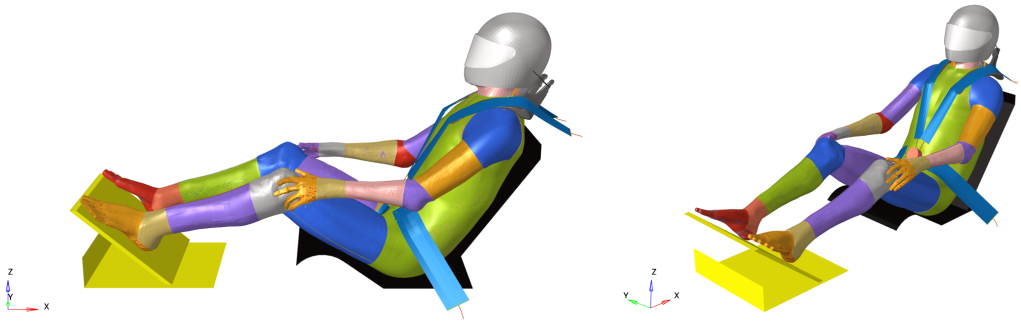

Figure 5.12: THUMS with HANS initial configuration

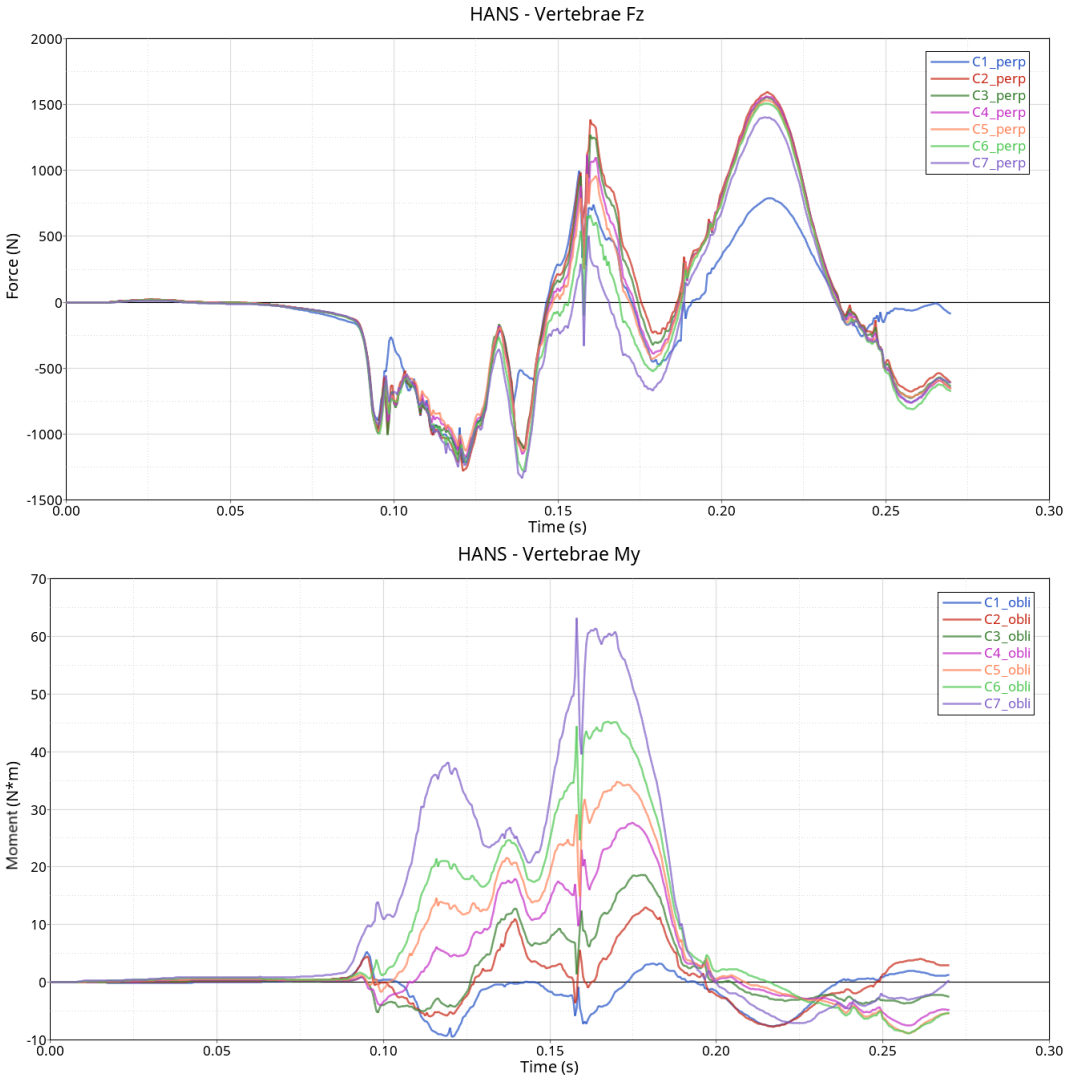

Figure 5.13: THUMS with HANS simulation output data

The forces F_z in the vertebrae have an initial compression part, which lasts from around 0.090 *s* to 0.148 *s*. All the vertebrae almost have the same compression values. C1 is the least loaded in the compression peak at 0.140 *s*, instead the most loaded are the ones furthest from the head (C6, C7). The THUMS initial compression part lasts longer than the one of the Hybrid III (Figure 4.30). Then, the first F_z tension peak begins. They all have the same profile, but the tension force peaks tend to decrease when the distance from the head increases. Also in this case C1 does not follow this trend, but it is not the least loaded. After the tension peak at 0.160 *s,* the HANS' tethers decrease the F_z force until compression is reached again. It is interesting to see that another tension peak is reached at about 0.220 *s*. This happens after the flexion peak, when the tethers pull back the head and it goes in tension with a very small amount of extension bending moment (Figure 5.14f). Another difference that is possibile to see, is that in the Hybrid III simulation the F_z compression peak value are higher than the tension peak value; instead, in the THUMS simulation we

can see that they have the same order of magnitude, with the tension peak slightly higher. Regarding the moment M_y, we can see that we do not have curves that are loaded only with extension moments, but the first three vertebrae (C1-C2-C3) have an extension-flexion load. Starting from C4 the vertebrae are loaded with flexion moments. The most loaded vertebrae are the ones furthest from the head.

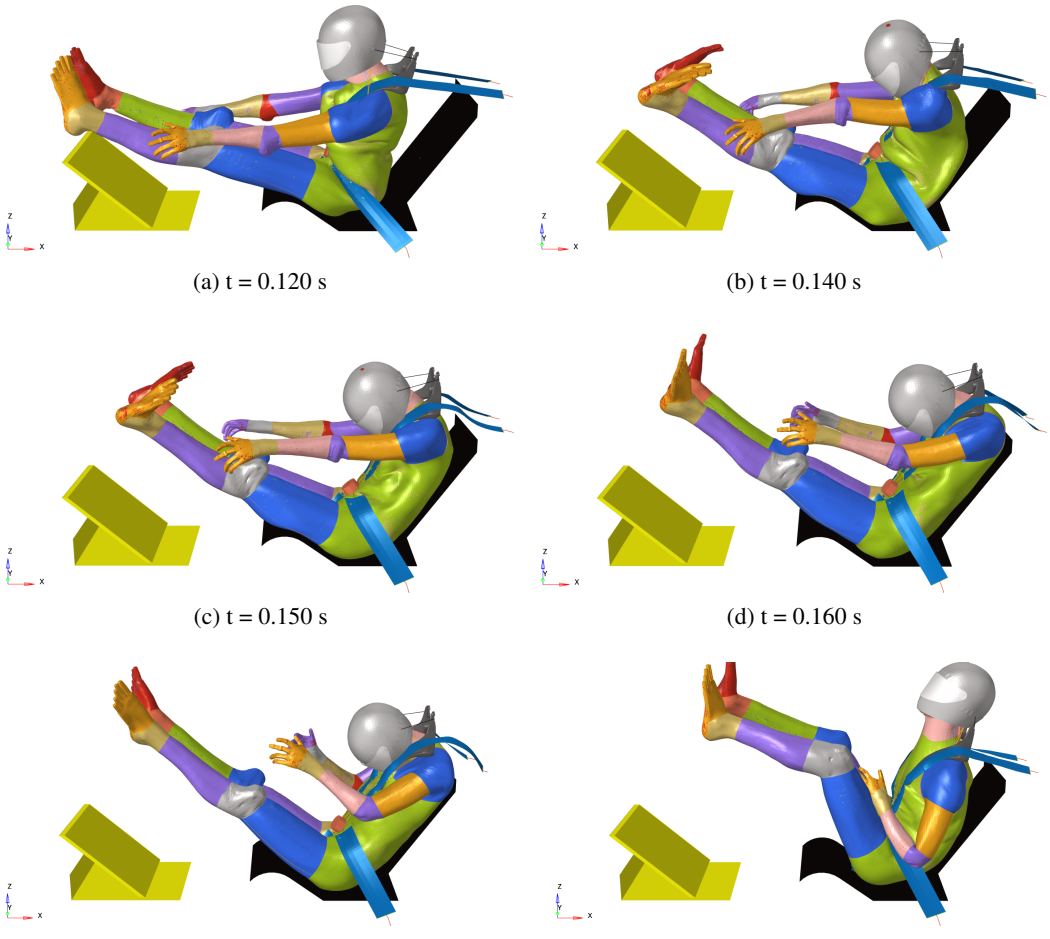

(a) t = 0.120 s (b) t = 0.140 s

(c) t = 0.150 s (d) t = 0.160 s

(e) t = 0.170 s (f) t = 0.220 s

Figure 5.14: THUMS with HANS simulation frames

5.2.3 THUMS with Hybrid PRO device

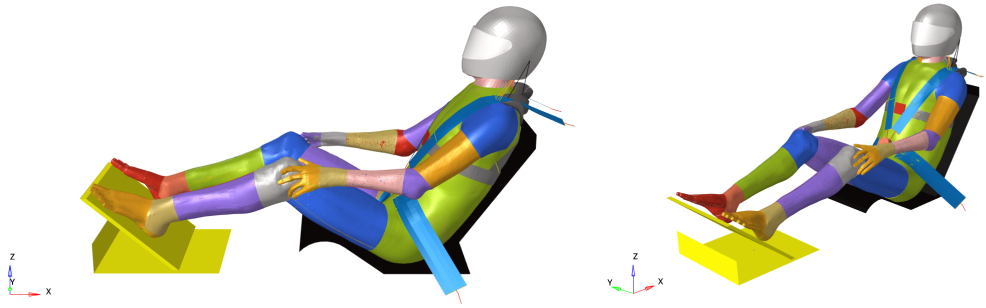

Figure 5.15: THUMS with Hybrid PRO initial configuration

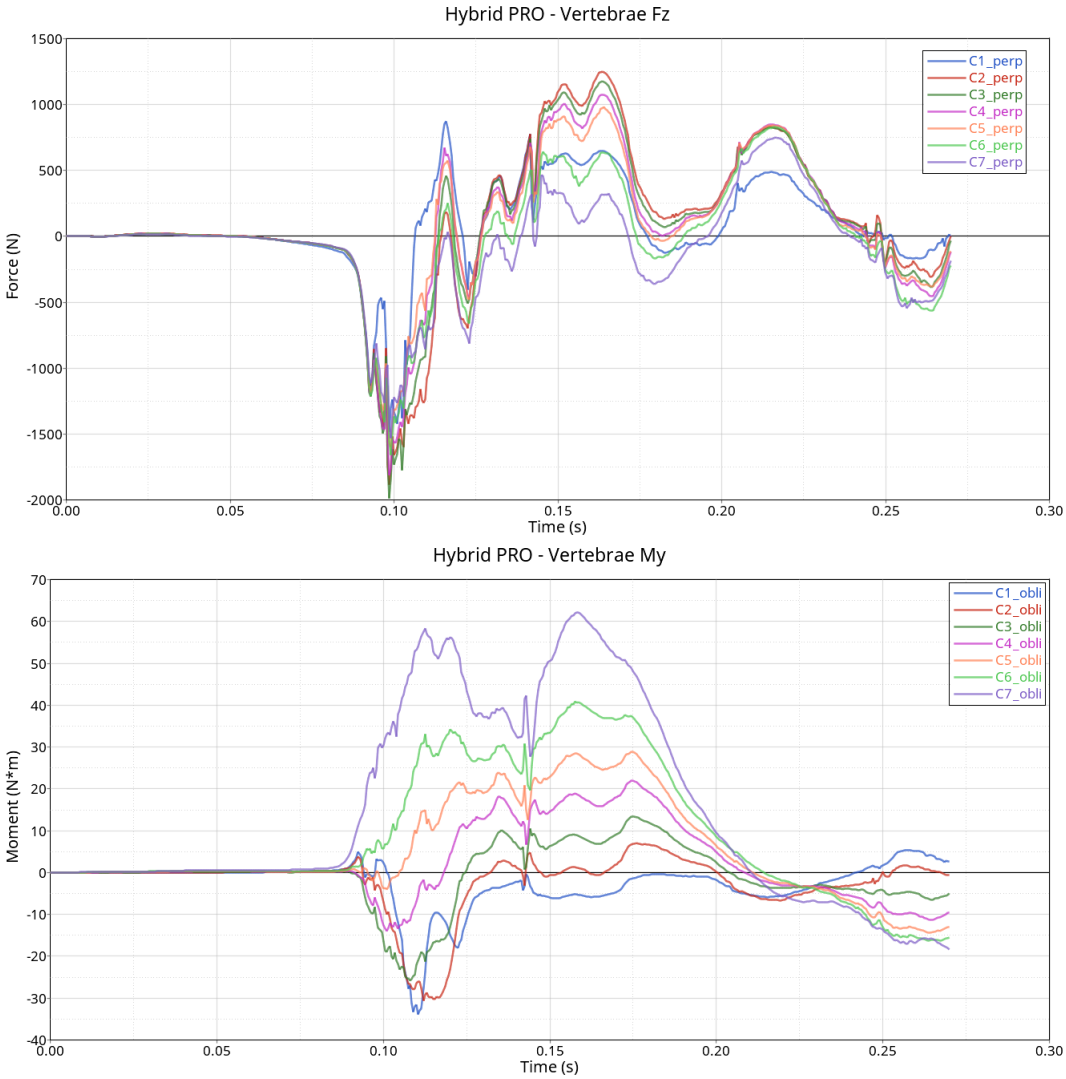

Figure 5.16: THUMS with Hybrid PRO simulation output data

Also with the Hybrid PRO device, forces F_z have all the same initial compression trend. C1 is initially the least loaded, but immediately after the compression peak there is a first tension peak, in which C1 now is the most loaded. Then, the trend is similar to what already see with the HANS device. Regarding the moment M_y, as it is better explained in the next section, there is a big initial extension peak in the vertebrae near the head, much larger than in the other cases. The trend is always the same, with C1 that is loaded mainly by extension moments, from C2 to C4 there is an extension-flexion loading condition, and finally the last vertebrae loaded only with flexion moments.

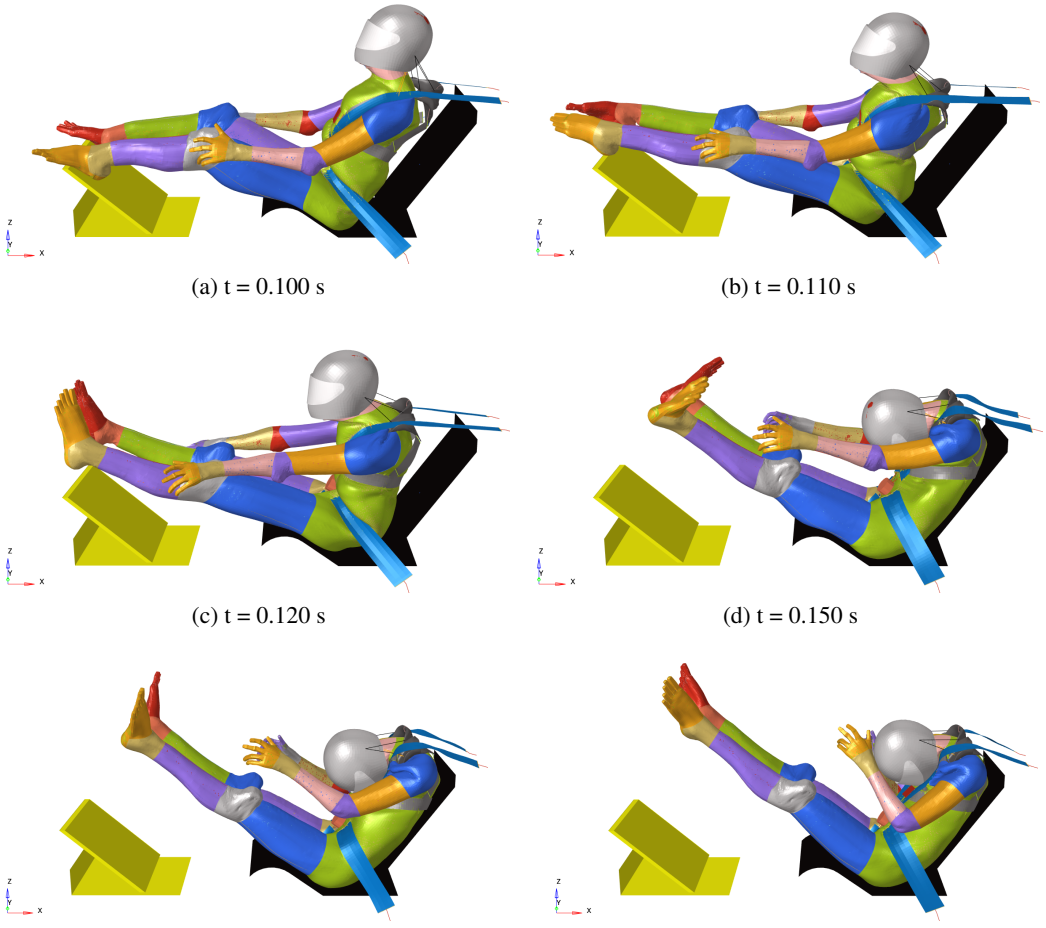

(a) t = 0.100 s (b) t = 0.110 s

(c) t = 0.120 s (d) t = 0.150 s

(e) t = 0.160 s (f) t = 0.170 s

Figure 5.17: THUMS with Hybrid PRO simulation frames

5.3 THUMS results comparison

In this section, the comparison between the resulting F_z forces and M_y are shown. To be more clear, the comparison graphs are made for each vertebra separately. Finally, a histogram shows the comparison between all the peak values. All the signs are inherent with the positive directions of neck forces and moments illustrated in Fig.3.15. Therfore, we consider positives tension forces and flexion moments.

5.3.1 THUMS vertebrae F_z comparison

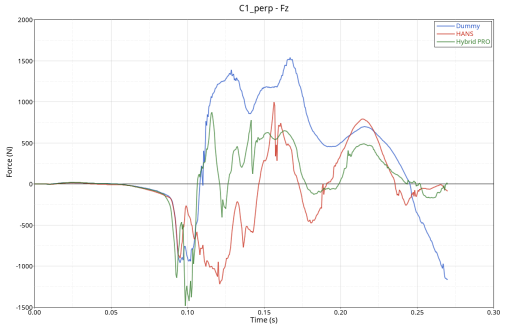

(a) C1

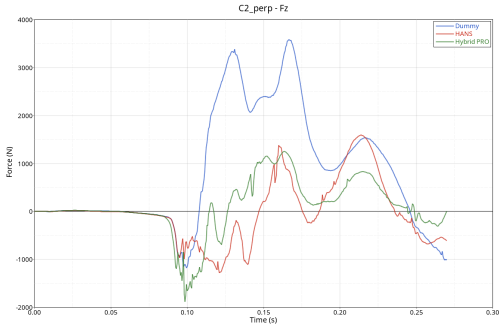

(b) C2

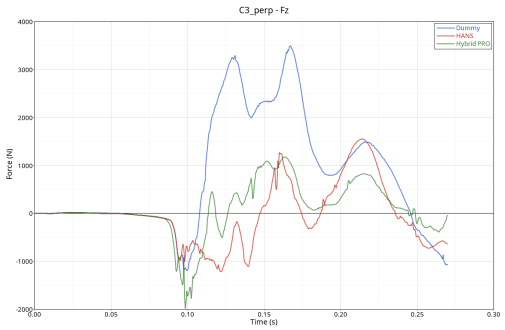

(c) C3

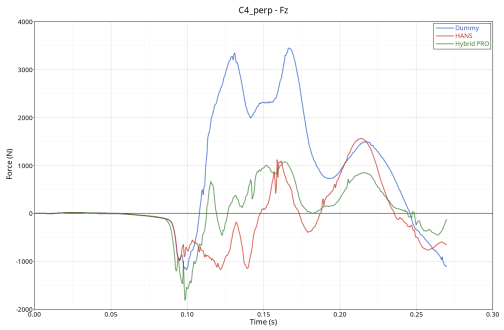

(d) C4

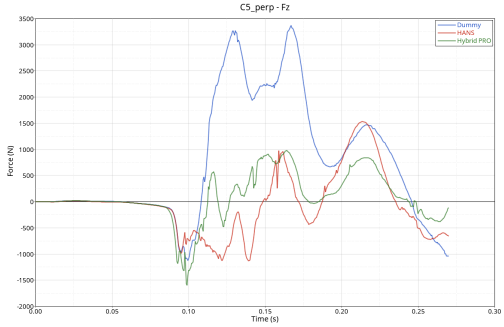

(e) C5

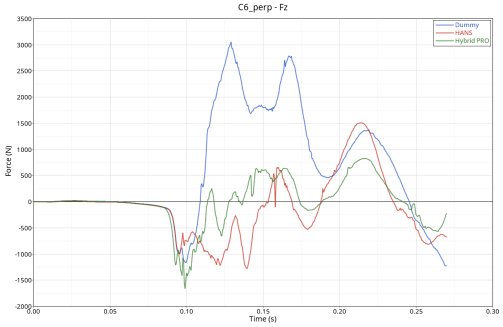

(f) C6

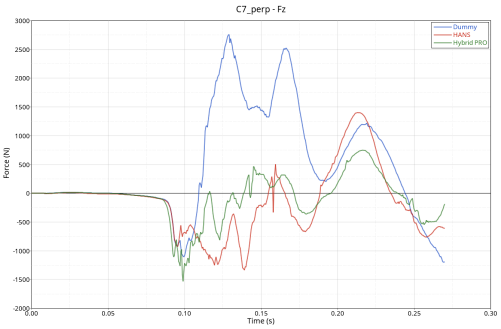

(g) C7

Figure 5.18: THUMS vertebrae F_z comparison

5.3.2 THUMS vertebrae M_y comparison

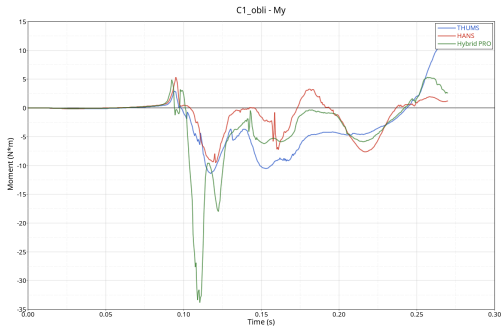

(a) C1

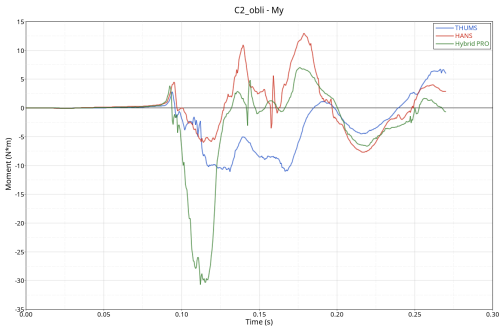

(b) C2

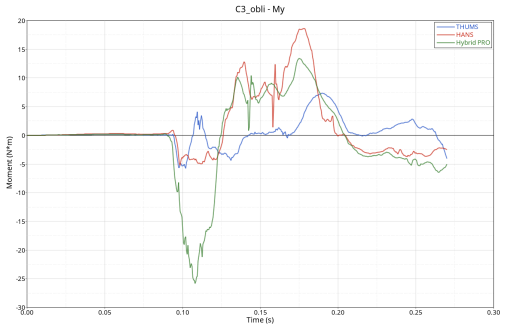

(c) C3

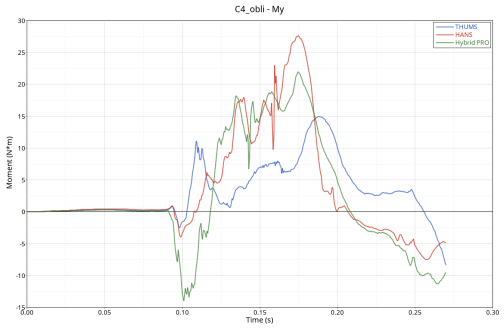

(d) C4

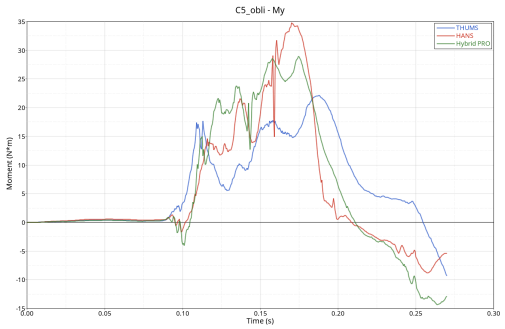

(e) C5

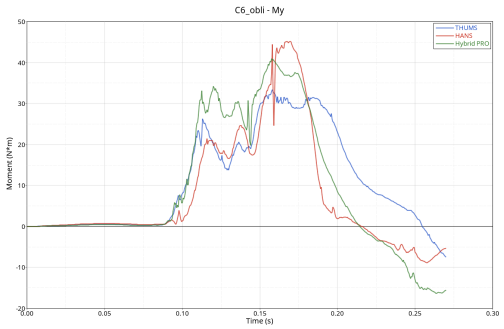

(f) C6

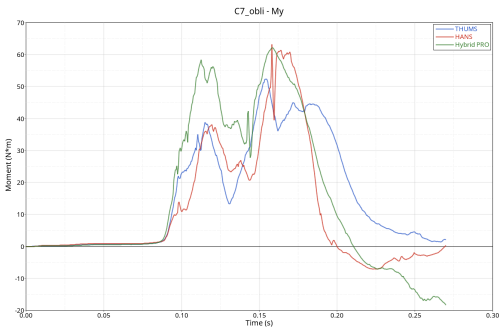

(g) C7

Figure 5.19: THUMS vertebrae M_y comparison

5.3.3 THUMS peak values comparison

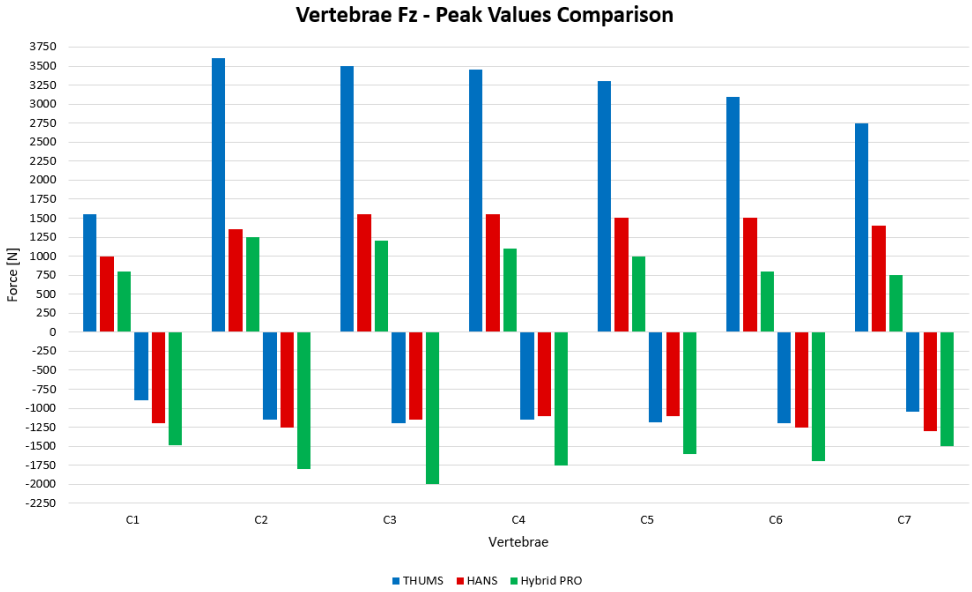

(a) F_z

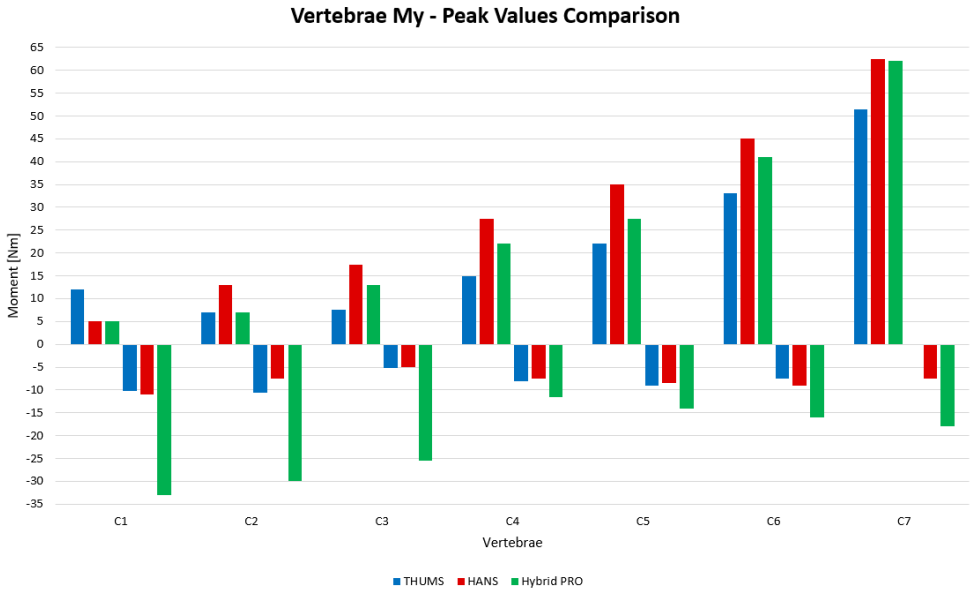

(b) M_y

Figure 5.20: THUMS peak values comparison

From these comparison graphs, it is evident how much the FHR devices are useful to decrease the F_z tension peaks in a human neck. In C2 there is around 63% tension load reduction. In all the vertebrae, the tension peaks with the FHR devices are all below the peaks without the FHR devices. This is not true for the compression peaks, in fact looking at Figure 5.20a it is possibile to see that we have a slight increase in the compression peaks

with the FHR devices. This is the price to pay to have the reduction in the tension load. It is due to the functioning of the devices' tethers, that, to decrease the tension load, they pull the head during the impact, creating a compression on the neck. However, it must be said that the decrease in the tension load is much bigger than the increase in the compression load. It is interesting to see that the Hybrid PRO device is the better looking at the tension load, but it is the worst looking at the compression load.

From the M_y comparison graph we can see that the FHR devices do not completely help to reduce the moment load. With the HANS device we have a significant increase in the flexion moment, instead the extension moment has a mixed behaviour with more or less the same values of the THUMS without FHRs. Also with the Hybrid PRO device, the flexion moment increases but less than with the HANS. Instead, with the Hybrid PRO we have a very big increase in the extension moment, especially in the vertebrae near the head (C1-C2-C3). Analyzing the simulation's animation we understood that this behaviour is caused by the used tethers configuration and position of the attachment point on the helmet. When the Hybrid PRO's tethers begin to pull the head, the position of the attachment point combined with the tether's slack length cause a significant extension rotation of the vertebrae near the head (this can be better seen in the RoM analysis in Chapter 6.2), causing a big increase in the M_y extension moment. In Figure 5.21 is possible to see the comparison between the point of maximum extension with the HANS device and the Hybrid PRO device. It is interesting to see also the difference in height of the FHR side tether's attachement point, which may have helped to create this big difference in the extension peaks.

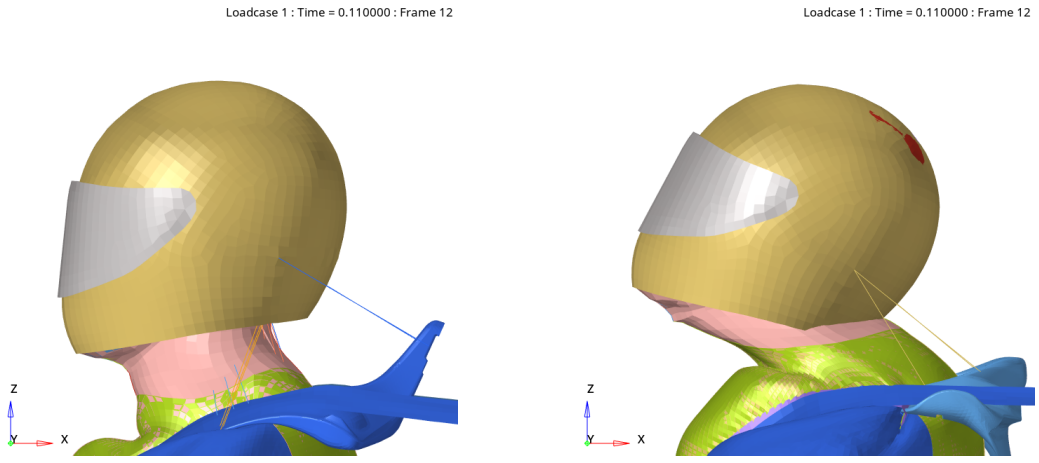

(a) HANS (b) Hybrid PRO

Figure 5.21: Maximum extension comparison

As said in Chapter 4.1.3.1, the CAD model of the real helmet used in the experimental tests was not available, so we used another helmet CAD model, provided by FIA, in all the FE models. This was smaller than the real one, so we could not perfectly reproduce both the real position of the helmet's connection point and the real tether's length. Differ-

ent numerical simulations were run to understand the behavior of the neck axial force F_z and the bending moment M_y changing the position of the helmet's connection point and the tether's slack length. From the results of the analysis we could understand that M_y is principally influenced by the position of the helmet's attachement point. The position used in the analysis was optimized on the Hybrid III with HANS FE model, fitting the corresponding experimental data. Then, to be consistent, the same attachment point position was used in the Hybdrid III with Hybrid PRO model, and then also in the THUMS models. Therefore, the high extension moment values in the THUMS model with the Hybrid PRO device can be caused by a non-optimal position of the helmet's attachement point for that type of FHR. Furthermore, we have seen that with the same helmet's attachement point, the HANS device instead has good M_y results. This could mean that there may be different optimal helmet's attachement point depending on the FHR type.
In this section we evaluated only the comparison of single forces and moments, but to study possible injuries is important to study the effect of the combination of these loads. This is done in Chapter 6.1, evaluating the N_{ij} criteria for the THUMS.

Chapter 6

THUMS' injury criteria

In this chapter, some injury criteria for the THUMS are discussed and proposed. Firstly the Nij criterion is used and then, the assessments of the RoM and of the plastic strain limit are performed. They were all described in Chapter 2.

6.1 THUMS Neck Injury Criteria

To assess the Neck Injury Criteria for each vertebra, the force and moments limits for the THUMS model must be defined. The limits showed in Table 2.1 are only valid for the Hybrid III dummies. The THUMS critical values of force and moment have been given by FIA, after the studies done in the MSc thesis previously mentioned [6]. These limits were founded with a correlation between normalized loads and moments of an Hybrid III pure frontal impact, and the loads and moments in each vertebra of a THUMS pure frontal impact with the same features. Due to the cross-sections' properties, showed in Chapter 5.1.2, the F_z force limits were defined considering the perpendicular cross-sections and the M_y extension and flexion moment limits were defined considering the oblique cross-sections. This procedure permitted to obtain some reasonable values that can be applied in numerical simulation injury assessment, and they are contained in Table 6.1.

Vertebra	$F_{t/c_{lim}}$ $[N]$	$M_{e_{lim}}$ $[N{\cdot}m]$	$M_{f_{lim}}$ $[N{\cdot}m]$
C1	1453	17.940	95.083
C2	1868	30.024	159.124
C3	1607	15.870	84.111
C4	1673	17.197	91.144
C5	1670	17.314	91.765
C6	1990	22.800	120.840
C7	1806	34.982	185.399

Table 6.1: Limit loads for each vertebra cross-section

These limits can be used for calculating the N_{ij}, with Eq.2.1, for each vertebra by replacing the standard Hybrid III's load limits, and they permit to better understand how much the vertebrae are loaded when considering both forces and moments at the same time. Nevertheless, it is important to remark that the described method is affected by some intrinsic problem and limitation that could condition the results. The limitations are listed below [6]:

- The limit loads are directly dependent on the loads measured on the vertebrae, this problem has been partially solved by scaling the first found limits, nevertheless the issue remain.

- Directly related to the first limitation: the measured loads (i.e. the limit loads) obviously depend on the boundary conditions and on the crash pulse.

- The limits are defined on specific cross-section that are not easy to identify. Moreover, they are not possible to be reproduced in other HBM or in THUMS versions that have different vertebral mesh.

- The assumption that the normalized loads are equal in Hybrid III upper neck section and in THUMS cervical vertebrae is not realistic (especially moving away from the occipital condyle), even if it was partially solved by scaling the first found limits.

In the next subsections, the N_{ij} trend in time is showed for each analysis in each vertebra. With these graphs, it is interesting to see how the N_{ij} evolves in time and what is the most critical situation of combined load.

6.1.1 N_{ij} - THUMS with helmet results

From the limits showed in Table 6.1, we can see that in the THUMS with helmet analysis, the F_z tension limit is exceed in all the vertebrae. This leads us to have inevitably a N_{ij} value greater than 1 in all the vertebre. Instead, the moment and compression load values are all less than the limits.

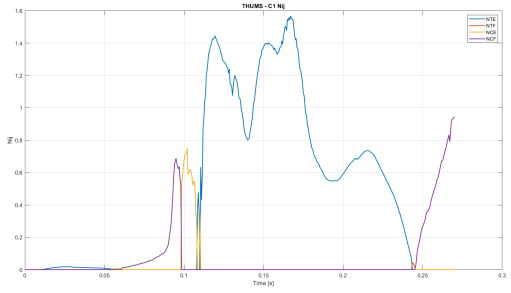

(a) C1

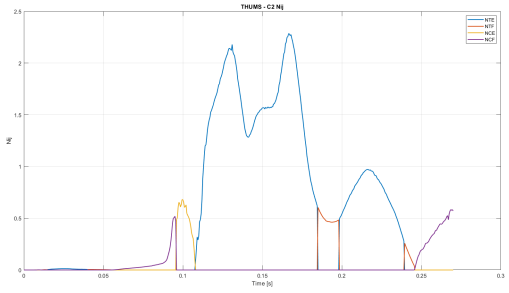

(b) C2

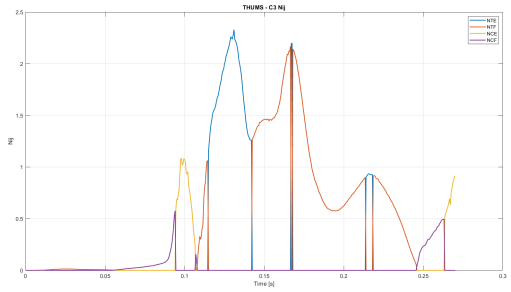

(c) C3

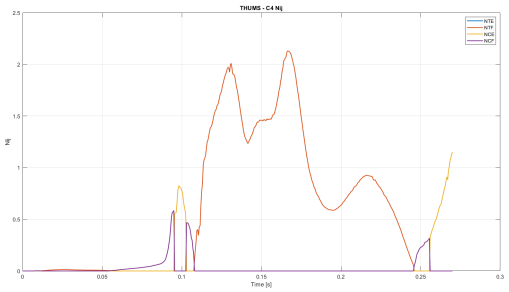

(d) C4

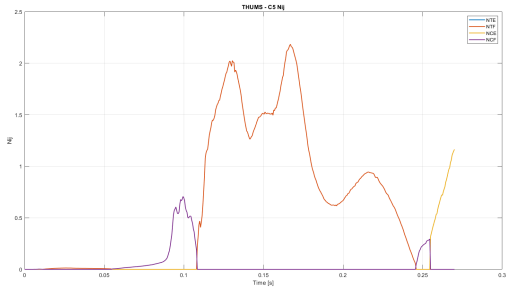

(e) C5

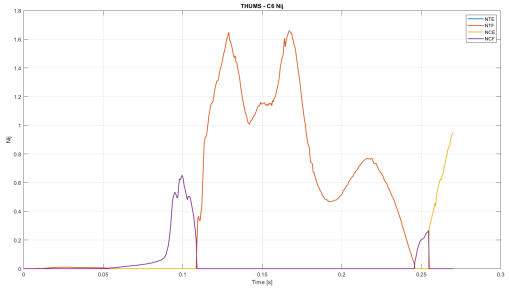

(f) C6

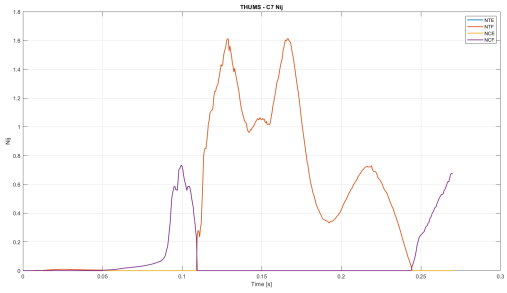

(g) C7

Figure 6.1: THUMS with helmet N_{ij} vs. time

6.1.2 N_{ij} - THUMS with HANS device results

As said in Chapter 5.3, the HANS device drastically reduces the F_z tension force. This permits in this case, to have also the tension load values below the limits. Therefore, with the HANS device we have all the single load peaks less than the corresponding limits. However, we can see that the N_{ij} value exceed 1 in the the first four vertebrae. This is due to the tension-extension or compression-extension combined loading condition. We can see from Eq.2.1, that even if the normalized force and the normalized moment are individually less than 1, added together can give a N_{ij} value higher than 1.

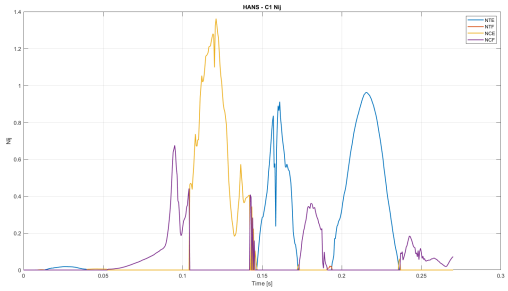

(a) C1

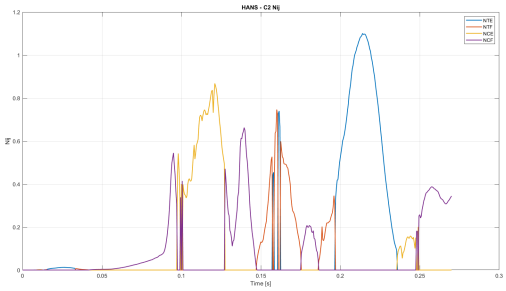

(b) C2

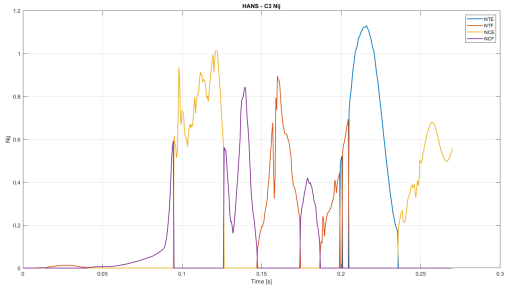

(c) C3

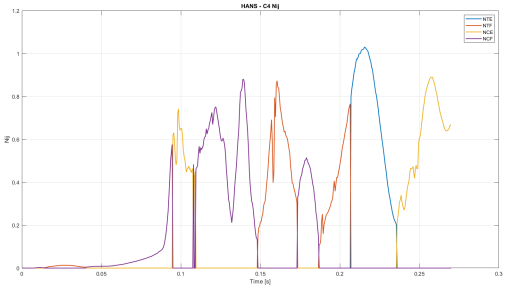

(d) C4

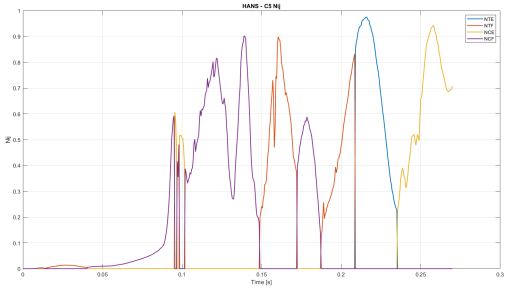

(e) C5

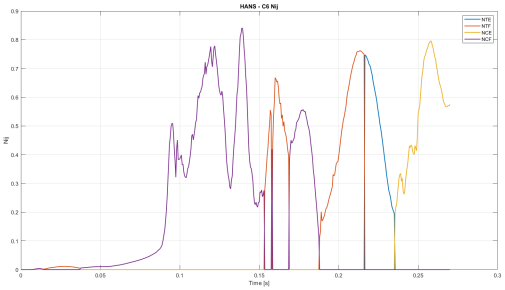

(f) C6

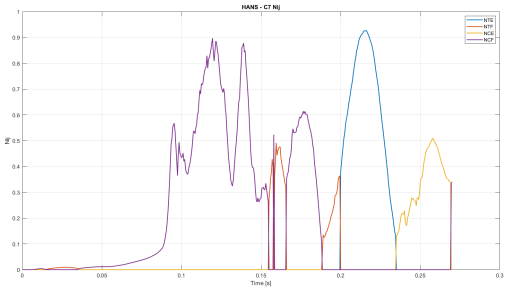

(g) C7

Figure 6.2: THUMS with HANS N_{ij} vs. time

6.1.3 N_{ij} - THUMS with Hybrid PRO device results

Also with the Hybrid PRO device we can see very good results in terms of F_z tension force. All the vertebrae have the F_z tension peaks well below the limits. But as seen in Chapter 5.3, with the Hybrid PRO device we had a very high extension moment peaks in the vertebrae near the head. In fact, in C1 C2 and C3 the extension moment limits are exceed, instead in C4 we are very close to the limit. This led us to have inevitably N_{ij} values higher than 1.

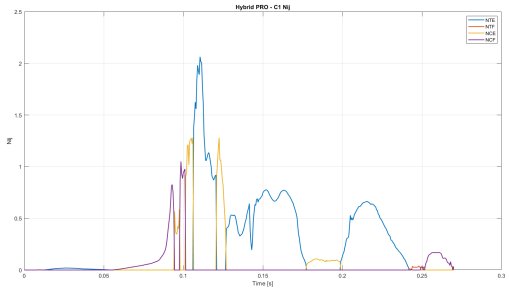

(a) C1

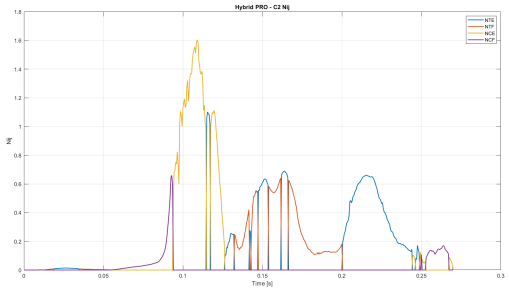

(b) C2

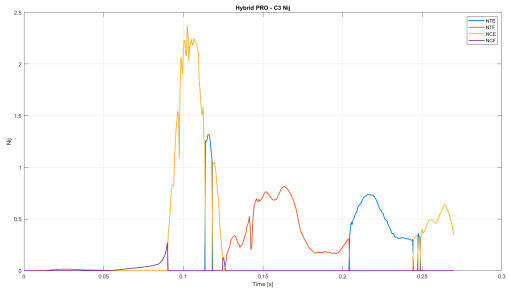

(c) C3

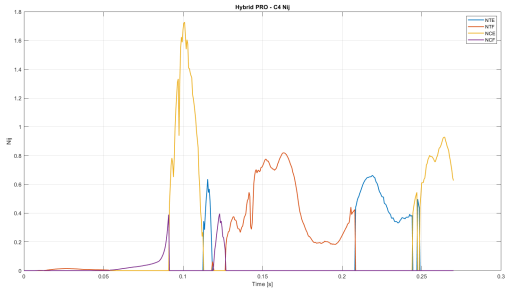

(d) C4

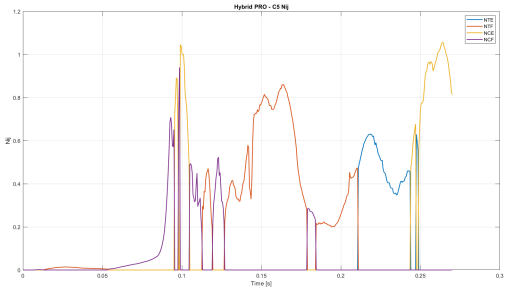

(e) C5

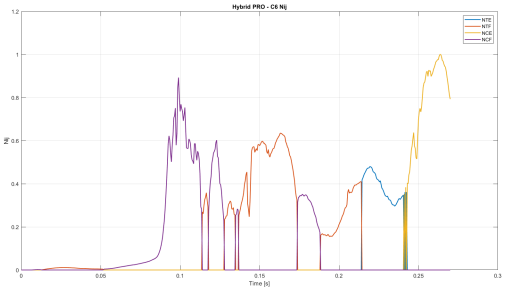

(f) C6

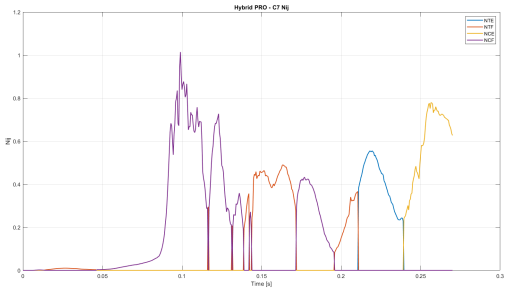

(g) C7

Figure 6.3: THUMS with Hybrid PRO N_{ij} vs. time

6.1.4 N_{ij} THUMS comparison

In Figure 6.4, the comparison between the N_{ij} peak values is showed. It is possible to notice that the peaks tend to decrease when the distance from the head increases. Also from these results we can see the advantages of the FHR devices, especially of the HANS. With the Hybrid PRO device, in C1 we have an higher N_{ij} value, from C2 to C4 we have only a small decrease in the peak values. These low performances of the Hybrid PRO are due to the high extension moment values in the vertebrae near the head, explained in Chapter 5.3.3. Instead, from C5 to C7 we have values similar to those of HANS. With the latter, instead we can see a strong N_{ij} peaks reduction in all the vertebrae.

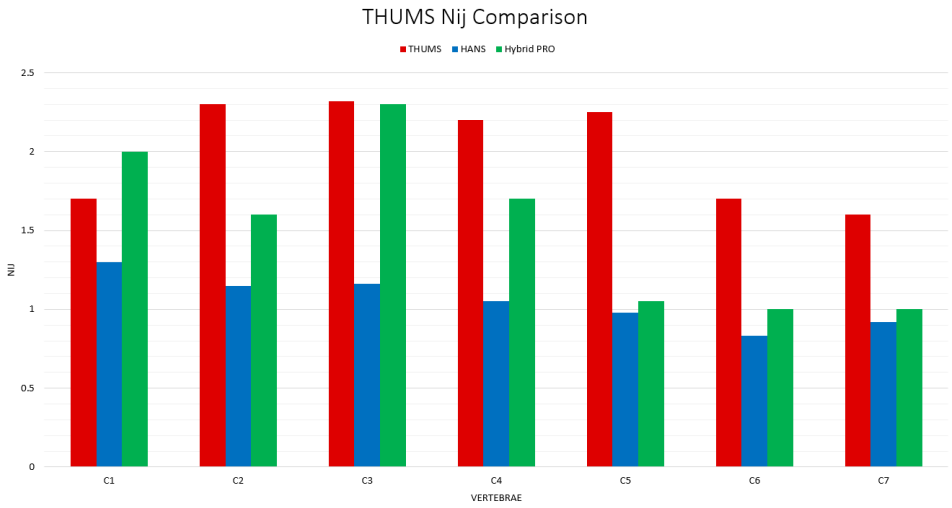

Figure 6.4: THUMS N_{ij} peak values comparison

These reductions can be seen as reductions in the probabilty to have injuries. In Table 6.2, the percentage decreases thanks to the FHR devices in the chance of serious, severe and critical injury are showed. They have been calculated according the *Abbreviated Injury Scale* showed in Chapter 2.2.1.

FHR	Vertebrae	Reduction in probability of serious injury	Reduction in probability of severe injury	Reduction in probability of critical injury
THUMS with HANS	C1	-21%	-12%	-4%
	C2	-51%	-33%	-21%
	C3	-47%	-29%	-19%
	C4	-56%	-31%	-15%
	C5	-61%	-39%	-22%
	C6	-34%	-20%	-7%
	C7	-25%	-13%	-6%
THUMS with Hybrid PRO	C1	+14%	+8%	+6%
	C2	-19%	-23%	-17%
	C3	-3%	-2%	-2%
	C4	-26%	-19%	-15%
	C5	-58%	-35%	-20%
	C6	-31%	-15%	-5%
	C7	-21%	-11%	-5%

Table 6.2: THUMS neck injury AIS risks comparison

6.2 Vertebral range of motion assessment

In Chapter 2.2.2 the mobility of head and neck was discussed. In particular, FSUs' range of motion has been defined and listed in Table 2.3. FEAs are very useful because they permit to evaluate the displacement and the rotation of a chosen node. THUMS is a very accurate HBM and it features accurate reproductions of vertebrae. Therefore, the numerical assessment of RoM permits to take advantage of both the aforementioned features. Practically, one node was chosen as representative of each vertebra. Moreover, it was possible to identify a node for describing the occipital condyle (C0), even if its geometry is not reproduced accurately. So, it was possible to evaluate the relative movement between the occipital condyle and the vertebrae. The rotation of each vertebra's reference node was requested as an output by using the card DATABASE_HISTORY_NODE [33]. Since we didn't define any local reference system, these rotations have been measured respect to the global reference frame. Therefore, to find the relative rotations between the vertebrae, the global rotations have been subtracted each other.

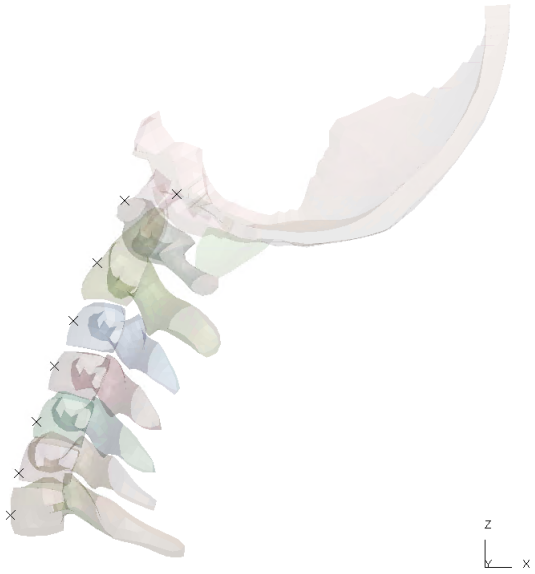

Figure 6.5: Nodes representative of each vertebra

The RoMs defined in the first chapter refer to rotations. The analysis showed that torsion and lateral flexion are almost negligible in the simulation. This indicates that the total rotation almost consist only of rotation in the sagittal plane Θ_y, as it is expected from a frontal impact simulation. Hence only Θ_y rotation is considered.

The assessment has been done by comparing the values of each Θ_y graph with the limit rotation defined in Table 2.3. However, the values contained in the aforementioned table refer to the total angular displacement in the sagittal plane, i.e. they are the angles between the limit positions of flexion and extension. The specific rotation limits for flexion and extension are not defined. B.Watier studied the RoM of the cervical spine in his work *"Etude expérimentale du rachis cervical: comportement mécanique in-vitro et cinématique in-vivo"* [7] and the ration between flexion and extension rotation limits were around 1:1 in subjects from 30 to 50 year-old. Niewiadomski et al. studied RoM in their work *"Experimental assessment of cervical ranges of motion and compensatory strategies" [14]* and found similar results. The flexion limit this time was a little higher than the extension limit with a ratio of 11:10. The study was done on subjects seated on an experimental chair. The torso of the subjects was straight. In this study, THUMS seated position already shows an initial neck flexion with respect to a straight bust configuration because the seat is inclined. Taking this into account, it is reasonable to consider the flexion/extension amplitude ratio as 1:1. Therefore, we considered half the limits of Table 2.3 for both extension and flexion. This is obviously an approximation because the rotation limit ratio between flexion and extension probably varies for each FSU. These limits are showed in the graphs by the positive and negative red areas. The lower limit of the areas represents the weakest subjects, instead the upper limit represents the strongest subjects. In the relative rotations' graphs showed, a positive value means that the first vertebra is in extension respect to the second, instead a negative valued

means that the first vertebra is in flexion respect to the second. From this graphs is possibile to better see the high extension rotation that we have in the first vertebrae with the Hybrid PRO device, therefore its results are influenced by this behaviour. Instead, with the HANS device we can see a reduction in the relative rotations, especially in the vertebrae from C1 to C3 and in the total relative rotation C0-C7.

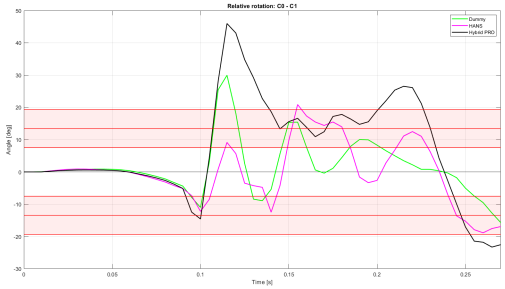

(a) C0-C1

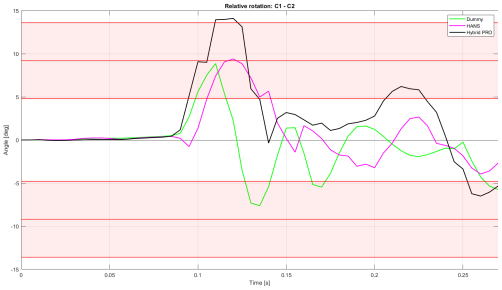

(b) C1-C2

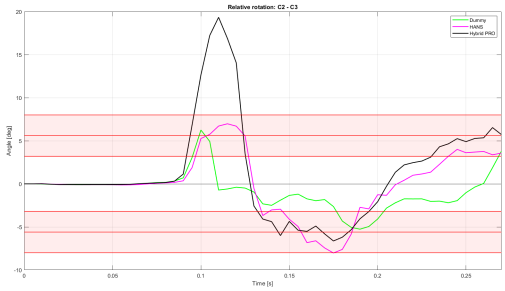

(c) C2-C3

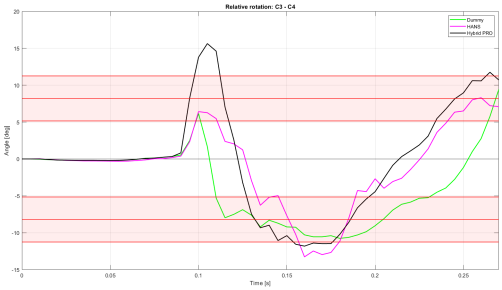

(d) C3-C4

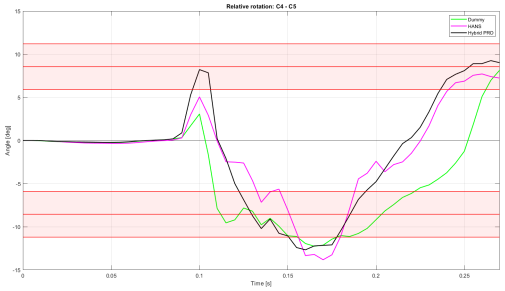

(e) C4-C5

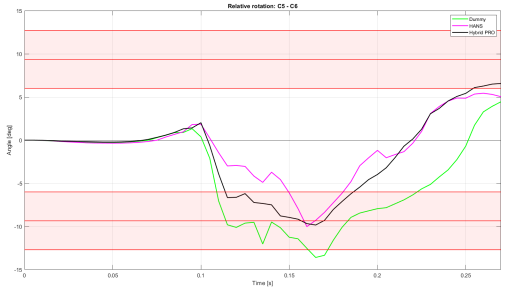

(f) C5-C6

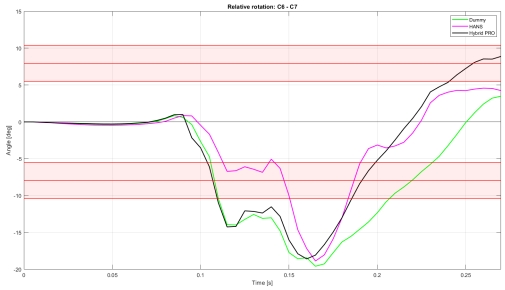

(g) C6-C7

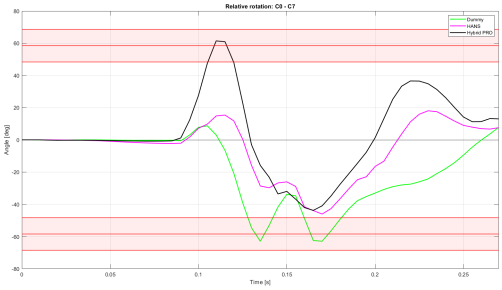

(h) C0-C7

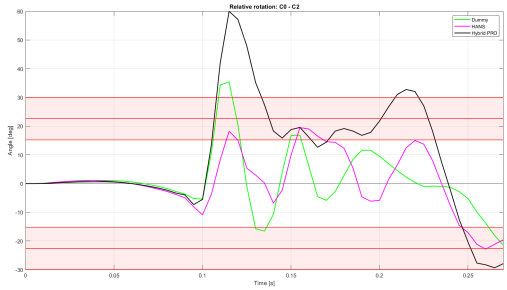

(i) C0-C2

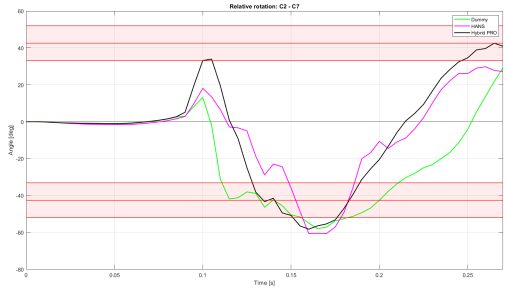

(j) C2-C7

Figure 6.6: THUMS Relative rotations Θ_y comparison

6.3 Plastic deformation on cervical vertebrae

Lately, several studies correlated plastic strain levels with bones fracture. These studies can be applied in crashworthiness, for injury assessment. In fact, FE model are capable of evaluating the plastic strain in every part of the model at each time step. Therefore, it is possible to take advantage of this feature by visualizing the vertebral plastic deformation during the crash numerical simulation. The effective plastic strain values (ε) are compared with a limit value that has been chosen equal to 2% as disclosed in the Chapter 2.2.3. The criteria refers to the cortical part of the bones.
Because of the fact that the focus of this chapter will be vertebral plastic strain, here below are reported the main feature of the FE model of the cervical bones. Each vertebra is composed of four part; two parts are composed of solid elements (one part for the left half and one part for the right half of the vertebra) and two parts are composed of shell elements and cover the surfaces of the solid parts. Given that the assessment has to be performed on the cortical bone, the focus has to be on the shell elements. The main feature of the shell parts are listed below:

- The section card is: SECTION_SHELL with ELFORM=16 [33] (fully integrated shell element)
- Density equal to $2e^{-9}\ \frac{ton}{mm^3}$
- Young modulus equal to $1.302e^{-4} MPa$
- Yield stress equal to 80 MPa
- Second plastic strain of 0.003 corresponding to a second yield stress of 110 MPa
- Third plastic strain of 0.015 corresponding to a second yield stress of 120 MPa
- strain rate parameter C equal to 360.7
- strain rate parameter P equal to 4.605

To better visualize the effective plastic strain, the vertebrae SET_PART from C1 to C7 has been requested as an output by using the card BINARY_D3PART [33].

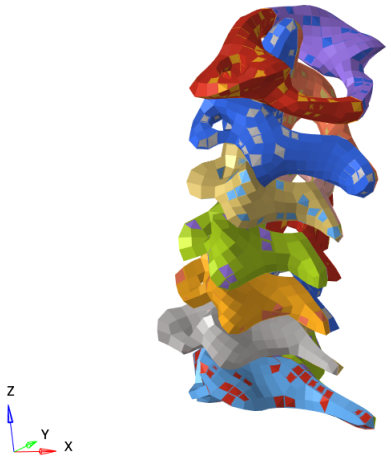

Figure 6.7: SET_PART representing the vertebrae from C1 to C7

The results have been visualized in the post-processing environment where the strain values can be visualized through element coloration. The maximum of the fringe range has been set to 0.02 because it is the strain value that should cause bone fracture. This type of visualization permit us to do an overall evaluation of the strain throughout the entire simulation. Nevertheless, it is not very practical. It is not possible to analyse data by just looking at the figures. In order to obtain other information such as the number of elements that pass the threshold, a MATLAB® script has been implemented. This script analyses an ASCII output file that contains elements' ID and elements' plastic strain. Then, it provided the following graphs:

- Maximum plastic strain
- Percentage of elements that exceeded the threshold
- Percentage of plasticised elements
- Average strain of plasticised element
- Average strain on each vertebra

In Figure 6.8 the comparison between these graphs is showed. We can see that, according to this criteria, the critical vertebra is C7. Also in this case, the effects of the high extension moment with the Hybrid PRO leds to have several elements with $\varepsilon > 2\%$ in the first three vertebrae. In Figure 6.9 the final effective plastic strain values distribution for each case are showed, with the maximum of the fringe range set to 0.02.

Figure 6.8: Effective plastic strain values comparison

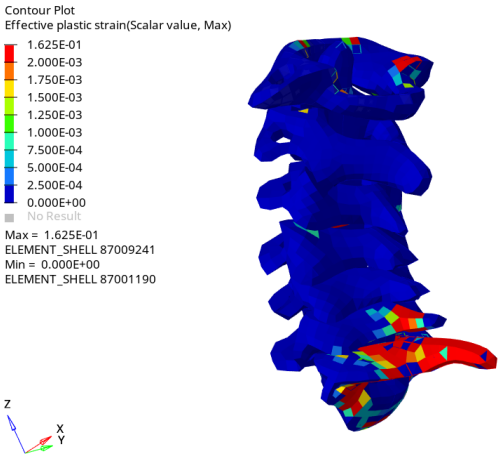

(a) THUMS with helmet

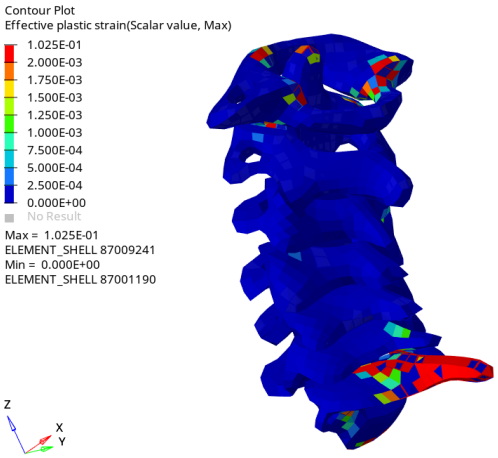

(b) THUMS with HANS

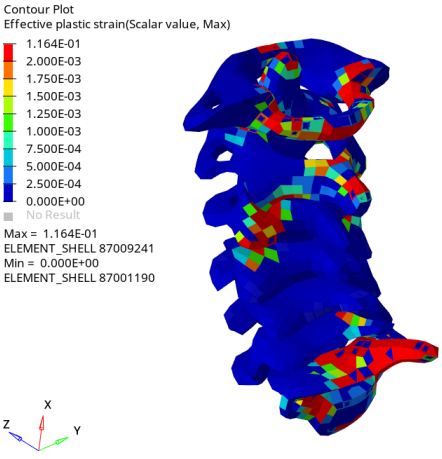

(c) THUMS with Hybrid PRO

Figure 6.9: Effective plastic strain values distribution

Conclusions

This thesis was focused on finding a numerical procedure to evaluate the safety performance of an FHR device in terms of human neck load.

Initially, the validation of the Hybrid III FE model have been done through the experimental tests data acquired. The Hybrid III experimental tests' results already showed good advantages in using the FHR devices, with a reduction in the F_z tension peak. The N_{ij} criteria for the Hybrid III has been used to assess the possibility of having neck injuries. From Figure 3.46, we have seen that with the FHR devices we could stay inside the safe region drawn by the Hybrid III load limits. A good correlation between the experimental tests and the Hybrid III FEA resulted from the simulations' post-processing. This especially for the head accelerations, the neck axial force F_z and the seatbelt forces. Regarding the M_y we could not perfectly validate the model, due to an acquisition problem during the experimental tests that lost in some points the M_y signal. For this reason the numerical moment values were bigger than the experimental ones, and this leds to have also higher numerical N_{ij} values in the tension-extension load combination.

Then the same FE model setup has been used with the THUMS model, in order to evaluate the safety performance of an FHR device in terms of human neck load. This evaluation has been done looking in each cervical vertebra at the z-axial forces parallel to the spinal cordal and the y-bending moments. From the results, we have seen that in all the vertebrae the tension peaks with the FHR devices are all below the peaks without the FHR devices, with reductions up to 63%. This is not true for the compression peaks, in fact we had a slight increase in the compression peaks with the FHR devices. This is due to the functioning of the devices' tethers, that, to decrease the tension load, they pull the head during the impact, creating a compression on the neck. However, it must be said that the decrease in the tension load is much bigger than the increase in the compression load. From the M_y comparison graph we can see that the FHR devices do not completely help to reduce the moment, having more or less the same values of the case without the FHRs. But with the Hybrid PRO we had a very big increase in the extension moment, especially in the vertebrae near the head (C1-C2-C3). Analyzing the simulation's animation we understood that this behaviour is caused by the used tethers configuration and position of the attachment point on the helmet. When the Hybrid PRO's tethers started to pull the head, the position of the attachment point combined with the tether's slack length caused a significant extension

rotation of the vertebrae near the head, causing a big increase in the M_y extension moment. This could be caused by a non-optimal position of the helmet's attachement point for that type of FHR.
Finally, these THUMS results have been analyzed with three injury criteria. The first one was derived from N_{ij} criterion for Hybrid III dummy and it was based on force and moment calculation on THUMS' vertebral sections. Load limits for the THUMS model replaced the standard Hybrid III's load limits, and they allowed to better understand how much the vertebrae were loaded when considering both forces and moments at the same time. From the results we have seen that in the THUMS with helmet analysis, the F_z tension limit was exceed in all the vertebrae, leading us to have inevitably a N_{ij} value greater than 1 in all the vertebre. Instead with the FHR devices the F_z tension limit was never achived in all the vertebrae. Therfore, with the FHR devices we could reduce the N_{ij} peak values in all the vertebrae, although still the vertebrae from C1 to C4 had a N_{ij} peak value higher than 1 due to the combination of forces and moments at the same time. The second criterion was based on anatomy studies and in particular on RoM of cervical spine segments. The results showed in a better way the high extension rotation that we have in the first vertebrae with the Hybrid PRO device, therefore its results were influenced by this behaviour. Instead, with the HANS device we could see a reduction in the relative rotations, especially in the vertebrae from C1 to C3 and in the total relative rotation C0-C7. The last criterion was based on the plastic strain that causes bone fractures. From FEA results we could evaluate the plastic strain in every part of the model at each time step visualizing the vertebral plastic deformation during the crash numerical simulation. The effective plastic strain values (ε) were confronted with a limit value that has been chosen equal to 2%. From this criteria the critical vertebra was C7. This result, was coherent with what seen in the RoM analysis, the N_{ij} instead showed that the critical vertebrae were the ones near the head.

6.4 Future developments

As said in Chapter 5.3, the high extension moment values in the THUMS model with the Hybrid PRO device could be caused by a non-optimal position of the helmet's attachement point for that type of FHR. Furthermore, we have seen that with the same helmet's attachement point, the HANS device instead had good M_y results. This could mean that there may be different optimal helmet's attachement point depending on the FHR type. Therefore, it could be interesting to perform a research in the optimal position of the helmet-tethers' connection point, for each FHR device and any size of helmet.
In this work, the FHRs have been modeled with a rigid material. A material characterization could be done to verify if during the impacts the FHRs deform.
THUMSv4.1 is not provided with muscles activation, so the numerical simulation described in this thesis are similar to PMHS tests. The muscular activation could be useful for simulating the actual behaviour of the occupant during a car crash. However, muscular activation

time and forces are difficult to evaluate correctly. In fact, the occupant response to crash depend on several factor such as reflexes, attention etc. THUMSv5 and following versions have the possibility to implement muscle activation and should be studied for better understanding the human body behaviour during car accident.

Bibliography

[1] The cervical spine. URL: https://teachmeanatomy.info/neck/bones/cervical-spine/. (accessed: 05.05.21).

[2] Stand21 - ultimate fhr. URL: https://www.stand21.com.

[3] Motorsport memorial, 2021. URL: http://www.motorsportmemorial.org/index.php.

[4] V I Adams. Neck injuries: I. occipitoatlantal dislocation - a pathologic study of twelve traffic fatalities. *Journal of forensic sciences*, 37, 3 1992.

[5] Vernard I. Adams. Neck injuries: Ii. atlantoaxial dislocation - a pathologic study of 14 traffic fatalities. *Journal of Forensic Sciences*, 37, 3 1992.

[6] E. Arlotti. Thums neck injury criteria study based on literature and comparison with hybrid iii dummy finite element model. 2021.

[7] B.Watier. Etude expÃ©rimentale du rachis cervical: comportement mÃ©canique in-vitro et cinÃ©matique in-vivo. 1997.

[8] B.Watier. Mechanical behaviour of cervical spine: literature update. *ITBM-RBM 27*, 2006.

[9] Toyota Motor Corporation. About thums.
.

[10] Federation Internationale de l Automobile (FIA). Auto + medical - safety in our hans, 4 2019. URL: https://www.fia.com/news/auto-medical-safety-our-hans.

[11] D.Johnson, B.Koya, and F.S. Gayzik. Comparison of neck injury criteria values across human body models of varying complexity. URL: https : / / www . frontiersin . org /
articles/10.3389/fbioe.2020.00985/full. (accessed: 30.04.2021).

[12] Sicking DL. Accident reconstruction of no. 3 car crash at daytona 500. *Official Accident Report, No. 3 Car, NASCAR Publications*, 2001.

[13] Rolf Eppinger, Emily Sun, Faris Bandak, Mark Haffner, Nopporn Khaewpong, Matt Maltese, Shashi Kuppa, Thuvan Nguyen, Erik Takhounts, Rabih Tannous, Anna Zhang, and Roger Saul. Development of improved injury criteria for the assessment of advanced automotive restraint systems-ii, 1999.

[14] C.Niewiadomski et al. Experimental assessment of cervical ranges of motion and compensatory strategies. *Chiropractic and Manual Therapies*, 2019.

[15] E.N.Marieb et al. Anatomie et physiologie humaines, 4th edition. 2010.

[16] M.Kleinberg et al. Development of improved injury criteria for the assessment of advanced automotive restraint systems. *NHTSA Docket*, 1998.

[17] M.Y.Svensson et al. Neck injuries in car collision-a review covering a possible injury mechanism and the developement of a new rear-impact dummy. *Accident Analysis and Prevention 32.2*, 2000.

[18] FIA. Guide and installation specification for hans devices in racing competition. 6 2017.

[19] FIA. Guide and installation specification for hybrid and hybrid pro devices in racing competition. 9 2018.

[20] Hubert Gramling, Peter Hodgman, and Robert Hubbard. Development of the hans head and neck support for formula one, 1998.

[21] Hubert Gramling and Robert Hubbard. Sensitivity analysis of the hans head and neck support, 2000.

[22] Nancy Heneson. Live animals in car crash studies.

[23] Humanetics. Harmonized hybrid iii 50th male. *User Manual*.

[24] Humanetics. Hybrid iii 50th male.

[25] Humanetics. Evolution of the crash test dummy, 6 2020. URL: https://humanetics.humaneticsgroup.com/perspectives/evolution-crash-test-dummy (accesed 06.10.2021).

[26] Toshio IMAIZUMI, Tsutomu SOHMA, Haruhiko HOTTA, Ichiro TETO, Hitoshi IMAIZUMI, and Mitsuo KANEKO. Associated injuries and mechanism of atlanto-occipital dislocation caused by trauma. *Neurologia medico-chirurgica*, 35, 1995.

[27] SFI FOUNDATION INC. . 4 2019. SFI SPECIFICATION 38.1 - Head and Neck Restraint Systems Specifications.

[28] SAE International. Sae j211-1: Instrumentation for impact test. 3 1995.

[29] J.H.Marcus. Dummy and injury criteria for aircraft crashworthiness. 1996.

[30] Albert I. King, David C. Viano, Nicholas Mizeres, and John D. States. Humanitarian benefits of cadaver research on injury prevention. *The Journal of Trauma: Injury, Infection, and Critical Care*, 38, 4 1995.

[31] Toyota Motor Corporation Toyota Central R'I&'D Labs. Total human safety model am50 occupant model, version 4.1. 2021.

[32] E. R. LeCOUNT. Symmetrical traumatic fractures of the cranium; symmetrical fragmentation. *Archives of Surgery*, 29, 8 1934.

[33] LIVERMORE SOFTWARE TECHNOLOGY (LST). *LS-DYNA KEYWORD USER MANUAL*. 2020.

[34] Stiles M, Walker A, and Milgrom G. Hans device. performance leader to market leader. sae technical paper series 2006-01-3629. 2006.

[35] H. Mertz, V. Hodgson, M. Thomas, and G. Nyquist. An assessment of compressive neck loads under injury-producing conditions. *The Physician and Sport Medicine*, 1978.

[36] Vincent J. Miele, Manohar M. Panjabi, and Edward C. Benzel. Anatomy and biomechanics of the spinal column and cord, 2012.

[37] S. Motta. Ottimizzazione di testa e collo di modelli fem di hybrid iii e validazione attraverso il confronto con prove sperimentali. a.a. 2017/2018.

[38] Code of Federal Regulations. Title 49 - subtitle b - chapter v - part 571 - subpart b - 571.208 standard no. 208; occupant crash protection., 1 2019.

[39] Famous Offaly People. Mary ward 1827-1869, 2007.
.

[40] M S Pollanen, J H Deck, B Blenkinsop, and E M Farkas. Fracture of temporal bone with exsanguination: pathology and mechanism. *The Canadian journal of neurological sciences. Le journal canadien des sciences neurologiques*, 19, 5 1992.

[41] Hubbard RP, Begeman PC, and Downing JR. Biomechanical evaluation and driver experience with the head and neck support, 1994.

[42] M Shojaati and Eth Zurich. Correlation between injury risk and impact severity index asi.

[43] D. A. SIMPSON, P. C. BLUMBERGS, R. D. COOTER, M. KILMINSTER, A. J. McLEAN, and G. SCOTT. Pontomedullary tears and other gross brainstem injuries after vehicular accidents. *The Journal of Trauma: Injury, Infection, and Critical Care*, 29, 11 1989.

[44] N. T. Spark. The fastest man on earth. *Annals of Improbable Research*, 2003.

[45] Van Tomme. Failure strains properties of the whole human vertebral body.

[46] Toyota Motor Corporation (Toyota). Documentation total human model for safety (thums) am50 occupant model, 2019.

[47] PH Trott, MJ Pearcy, SA Ruston, I Fulton, and C Brien. Three-dimensional analysis of active cervical motion: the effect of age and gender. *Clinical Biomechanics*, 11, 6 1996.

[48] B. M. VANCE. Fractures of the skull. *Archives of Surgery*, 14, 5 1927.

[49] Wikipedia. Crash test dummy. (accessed 01.10.2021).

[50] Wikipedia. List of driver deaths in motorsport, 2021.
.

[51] Bao-Li Zhu, Li Quan, Kaori Ishida, Mari Taniguchi, Shigeki Oritani, Masaki Q. Fujita, and Hitoshi Maeda. Longitudinal brainstem laceration associated with complex basilar skull fractures due to a fall: an autopsy case. *Forensic Science International*, 126, 3 2002.

Appendix A

Seatbelts' material characterization

To better model the seatbelts in the numerical models, a material characterization has been done. The seatbelts used in the experimental tests are described in Chapter 3.4.2. They were an OMP® six points safety harness with 2"/3" shoulders straps, 3" lap straps and 2" crotch straps.

Displacement controlled tensile tests have been done on each seatbelt's strap, in order to have the experimental force vs. displacement curves. The tests have been done in the laboratory of the Politecnico di Milano's Aerospace Science and Technology Department. We disassembled the safety harness, obtaining the three different sections (shoulders, lap and crotch) to be tested. At the extremities of these sections we left the steel hooks and we used them for the grasping to the machine's crossheads. Before all the tests we measured the effective sections' lenghts in order to reproduce them correctly in the FE models. The dimensions of the three seatbelts' sections are reported in Table A.1.

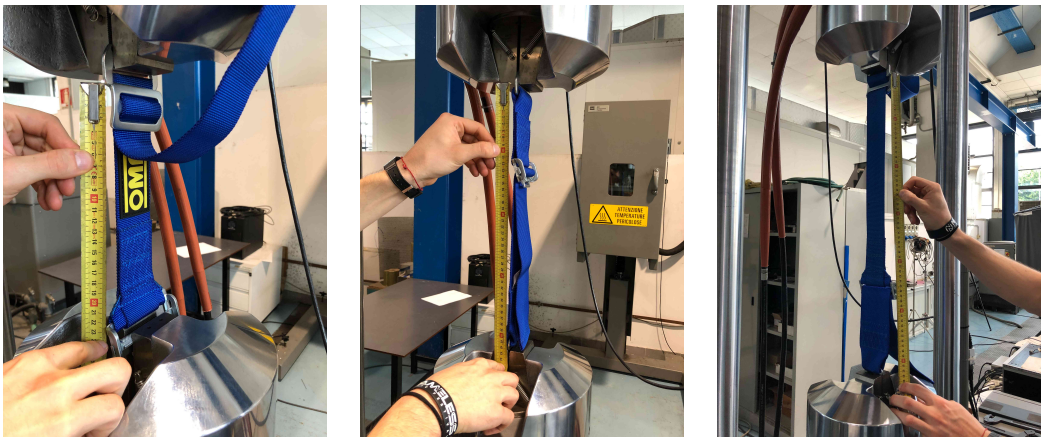

(a) Crotch section (b) Lap section (c) Shoulders section

Figure A.1: Seatbelts experimental tests' setups

Seatbelt section	Length [mm]	Width [in]	Thickness [mm]
Crotch	220	2	1.8
Lap	400	3	1.8
Shoulders	690	2	1.8

Table A.1: Seatbelts' sections dimensions

In all the tests we mantained a constant controlled displacement rate of $5\frac{mm}{min}$, measuring the force exercised by the machine. The resulting force vs. displacement curves are showed in Figure A.2. The curves have a small initial non-linear elastic part, also caused by the non-linearities of the machine clamps not perfectly fitted on the seatbelts' ends. Then there is a linear part, and finally the failure. It was interesting to see that the failure was not given by the material, but by the seatbelts' stitchings as showed in Figure A.3. From the curves it also possible to see the hysteresis phenomenon in the unloading phase. This difference in energy could be dissipated by the sliding of the wrapped strands, as internal friction (heat), during the test cycle.

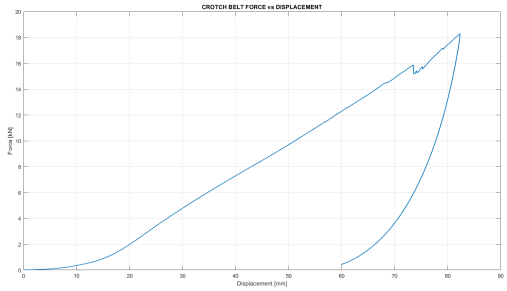

(a) Crotch Force vs. Displacement experimental curve

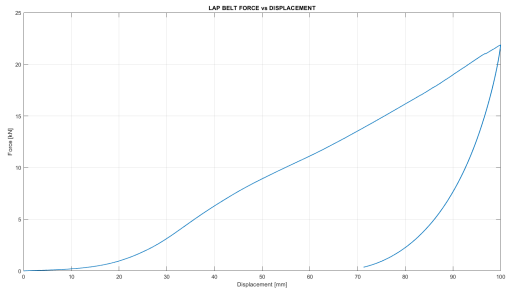

(b) Lap Force vs. Displacement experimental curve

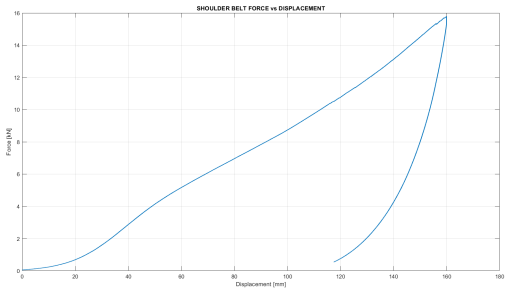

(c) Shoulders Force vs. Displacement experimental curve

Figure A.2: Seatbelts Force vs. Displacement experimental curves

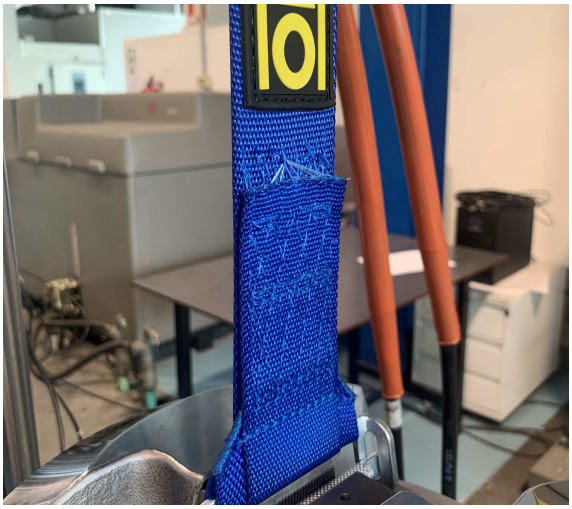

Figure A.3: Seatbelts' stitchings failure

From the graphics, we were mainly interested in the linear central part which best described the stiffness of the belt. In fact, in a force vs. displacement curve the stiffness is represented by the slope of the curve. To represent it, three FE models of the three seatbelts' sections have been created. They were made only of shell elements, with the same mesh size used in the Hybrid III and THUMS FE models. The nodes of one end have been constrained and to the ones of the other end has been assigned a constant velocity PRESCRIBED_MOTION_SET [33] card. Since we have seen from experimental results that there is a very big linear part, initially we decided to use a simple MAT_001-ELASTIC to model the seatbelts' material. So we run several static implicit analysis for each model, changing the elastic modulus until similar behaviours in the force vs. displacement curves have been reached.

Since all the sections were made of the same material, ideally only one elastic modulus could be enough to model all the three sections. But due to the non linearities given by the stitchings, the graspings, etc., this could not be done. Two elastic modulus have been defined, one for the 3" sections and another for the 2" sections. So we could model the shoulders and crotch straps with the same material properties, showed in Table A.2. The force vs. displacement comparison curves are showed in Figure A.4.

Seatbelt section	Density $\left[\frac{ton}{mm^3}\right]$	Elastic Modulus $[MPa]$	Poisson ratio
Crotch	$1.0e^{-9}$	735	0.3
Lap	$1.0e^{-9}$	835	0.3
Shoulders	$1.0e^{-9}$	735	0.3

Table A.2: Final MAT_001-ELASTIC properties

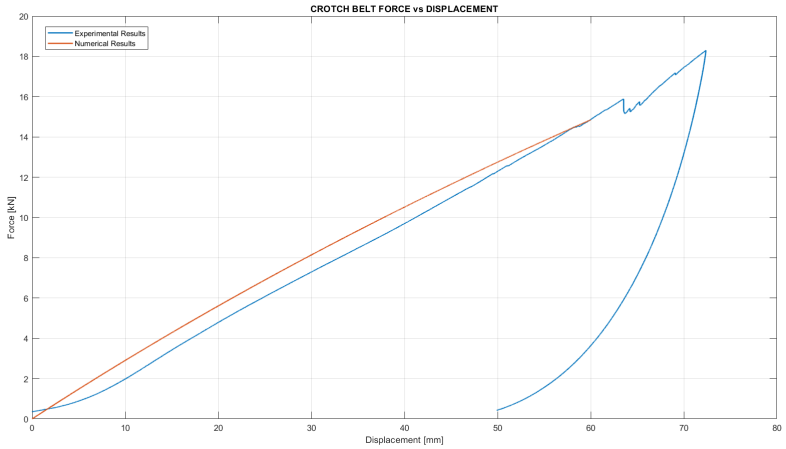

(a) Crotch numerical-experimental comparison

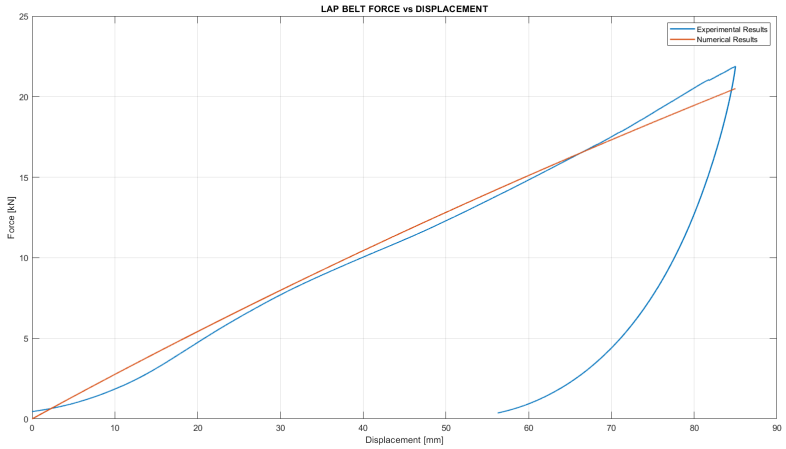

(b) Lap numerical-experimental comparison

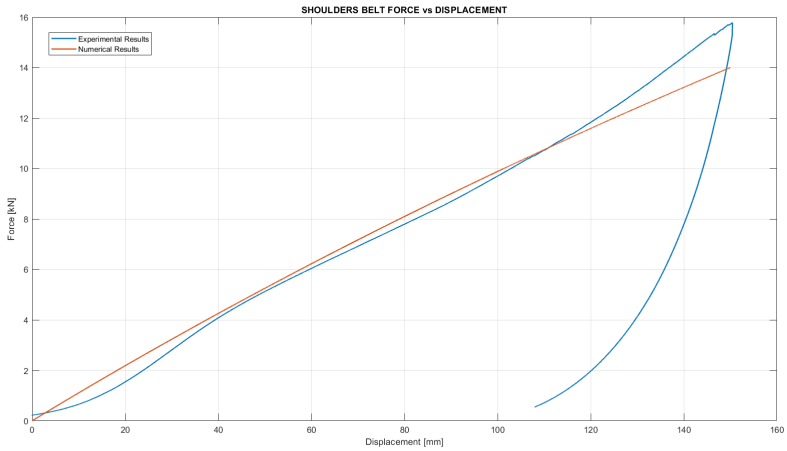

(c) Shoulders numerical-experimental comparison

Figure A.4: Force vs. Displacement comparison curves

As said in Chapter 4.3, using this material card inside the Hybrid III model we had an average error for the shoulders seatbelt forces of 7.096% respect to Hybrid III experimental data. This was a very good result, therefore we decided to use these properties for all the numerical models. For a future development, to reproduce even better the experimental force vs. displacement curves can be taken into account the MAT_181_SIMPLIFIED_RUBBER material card. Setting the *K* bulk modulus and a piecewise linear loading curve *LC,* it is possible to reproduce the inflection points of the experimental force vs. displacement curves with straight lines with different slopes.

Appendix B

SAE J221 Butterworth filters

The SAE filtering operation performs two-pass, zero phase shift, second-order Butterworth filtering. A Butterworth four-poles digital filter is here described. A difference equation is used for filtering a sequence of data samples. The filtering results in an amplitude versus frequency response curve [28]. The difference equation in the time domain has this form:

$$Y[t] = a_0X[t] + a_1X[t-1] + a_2X[t-2] + b_1Y[t-1] + b_2Y[t-2] \tag{B.1}$$

where: *X [t]* is the input data stream, *Y [t]* is the filtered output data stream, a_0, a_1, a_2, b_1, b_2 are constant depending on the cutoff frequency and sample period *T*.

$$w_d = 2\pi \cdot CFC \cdot 2.0755$$

$$w_a = \frac{sin(w_d) \cdot 0.5 \cdot T}{cos(w_d) \cdot 0.5 \cdot T}$$

$$a_0 = \frac{w_a^2}{1 + \sqrt{2 \cdot w_a} + w_a^2}$$

$$a_1 = 2 \cdot a_0$$

$$a_2 = a_0$$

$$b_1 = \frac{-2(w_a^2 - 1)}{1 + \sqrt{2 \cdot w_a} + w_a^2}$$

$$b_2 = \frac{-1 + \sqrt{2 \cdot w_a} - w_a^2}{1 + \sqrt{2 \cdot w_a} + w_a^2}$$

Equation B.1 is for a two-pole filter. To make a four-pole filter, the data are passed

through the filter twice. By passing the data through the filter forward and then backward, the filter will not phase shift the data. Peaks in filtered data set will occur at the same time as peak in the unfiltered data. In this work, this has been done with the *filtfilt* MATLAB® function.

y = filtfilt(b,a,x) performs zero-phase digital filtering by processing the input data, x, in both the forward and reverse directions. After filtering the data in the forward direction, filtfilt reverses the filtered sequence and runs it back through the filter. The variables *a* and *b,* are the vectors containing the filters constant a_0, a_1, a_2, b_1, b_2.

Startup of a digital filter yields the same response as switching a signal into the input of an analog filter. The digital filter sees nonzero initial data as a step function and responds with a typical underdamped second-order response.

There are class-specific operators filters for each of supported SAE filtering classes. This filters are named CFC[1]. Each class has its own characteristics defined by its identification number. This number is not the cutoff frequency but indicates the minimum sampling frequency for the input data. It is clear from the J211 filter specifications that they were derived from analog Butterworth filters whose corner frequency is equal to the CFC designation divided by 0.6.

Filter type	**Filter parameters**	
CFC60	3 dB limit frequency	100Hz
	Stop damping	-30 dB
	Sampling frequency	at least 600 Hz
CFC180	3 dB limit frequency	300Hz
	Stop damping	-30 dB
	Sampling frequency	at least 1800 Hz
CFC600	3 dB limit frequency	1,000Hz
	Stop damping	-40 dB
	Sampling frequency	at least 6 khz
CFC1000	3 dB limit frequency	1,650Hz
	Stop damping	-40 dB
	Sampling frequency	at least 10 khz

Figure B.1: CFC classes requirements

[1] Channel frequency classes

Appendix C

Hybrid III simulation with crash tubes

As said in Chapter 4.1.2, for what concern the crash pulse in the numerical models we used a PRESCRIBED_MOTION crash pulse approach to decrease the heaviness of the calculations that have to be performed by the calculator, hence the time needed to finish the simulation. Instead, in the experimental tests the crash deceleration was provided by stopping the sled with several crash tubes while it was moving at high speed. Therefore we made a numerical model of the Hybrid III with helmet test, to verify that the two approaches gave the same results.

It has been used the same model, removing the PRESCRIBED_MOTION crash pulse. Therefore, to reproduce the crash pulse we had to create the FE model of the crash tubes described in Chapter 3.2. The crash tubes' setup used in the experimental tests was composed by seven square tubes 60 x 60 *mm* and 3 *mm* thick, made of *6082 Aluminum alloy* and with the length starting from 640 *mm* and then for each tube the length decreased of 20 *mm,* so the shorter one was 520 *mm* long. We created the tubes FE model with only shell elements, respecting all the dimensions and positions. The tubes' material has been modeled with the MAT_024_PIECEWISE_LINEAR_PLASTICITY using the *6082 Aluminum alloy* properties taken from the Total Materia® database. An INITIAL_VELOCITY with a x-velocity of 50 $\frac{km}{h}$ has been given to the whole model's nodes, expect those of the tubes. In this way we reproduced the experimental impact velocity of the sled. The contact between the sled and the crash tubes is modeled with an AUTOMATIC_SURFACE_TO_SURFACE contact card. To simulate the work done by the constraint of the feet to the footrest with the ratcheting strap, this time we could not use the PRESCRIBED_MOTION card. Therefore, two DEFORMABLE_TO_RIGID cards have been used. With the DEF_TO_RIGID card, deformable parts defined in the model may be switched to rigid during the calculation [33]. In the definition of the card, a MRB could be setted. MRB was the Part ID of the master rigid body to which the deformable part is merged when switched to rigid. In this way we defined a first switch point at the beginning of the simulation, in which a deformable

part-set of the feet has become rigid, with as MRB the rigid foot-floor part. Thanks to this, from that time on, the feet moved as constrained with the foot-floor. The feet remained constrained also after the impact with the tubes, for a time equal to the *death-time* used in the PRESCRIBED_MOTION approach. After this time, we defined a second switch, RIGID_TO_DEF, which caused the feet rigid parts to become deformable again, removing the constraint. In this way we could model the initial F_z compression peak.

In Figure C.1, it is showed the comparison between the ouput data obtained with the PRESCRIBED_MOTION approach and the ones obtained with the crash tubes.

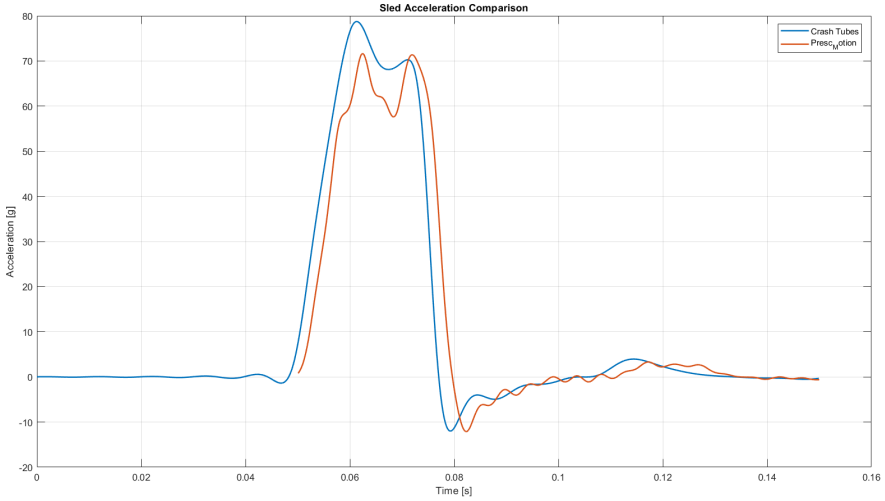

(a) Crash pulse

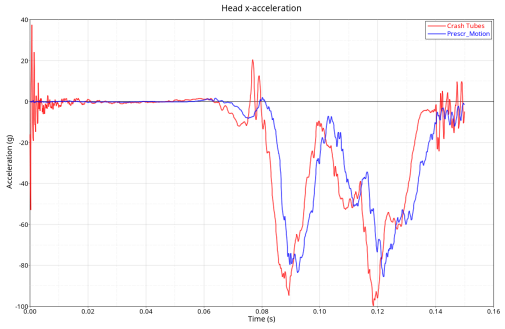

(b) Head x-acceleration

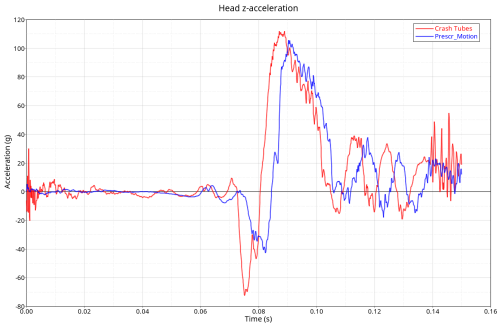

(c) Head z-acceleration

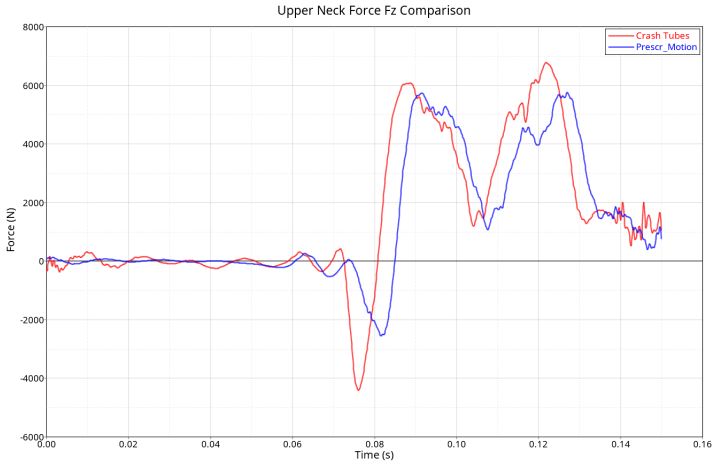

(d) Upper-Neck F_z

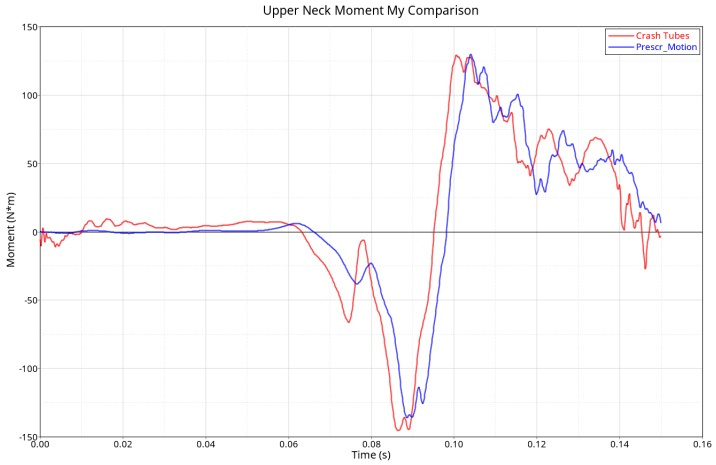

(e) Occipital condyle M_y

Figure C.1: Comparison between PRESCRIBED_MOTION and crash tubes approaches

It is possible to see that the crash pulse is slightly higher. This can be caused by the material properties data used and variability of tubes properties in the experimental tests. All the other comparison results are very good. In Figure C.2 the comparison of the animations' frames is showed, with on the left the numerical results using the PRESCRIBED_MOTION approach, in the center the experimental tests and on the right the numerical results using the crash tubes.

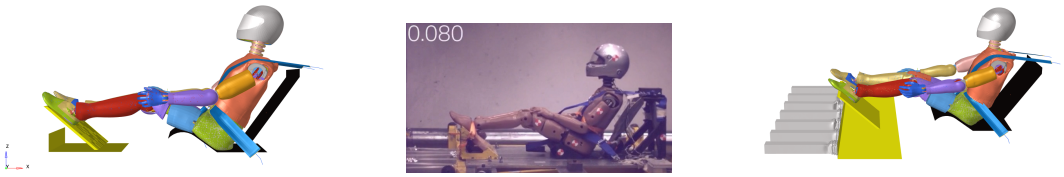

(b) t = 0.080 s

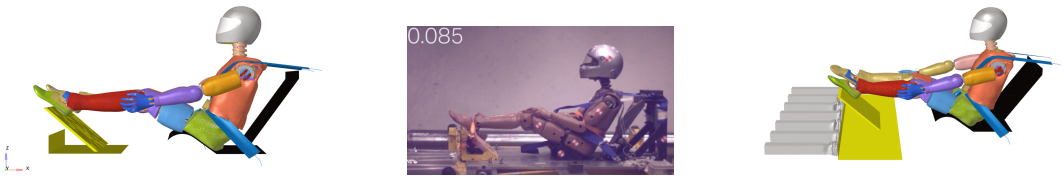

(e) t = 0.085 s

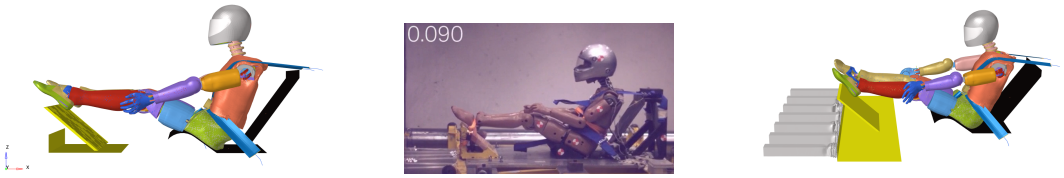

(h) t = 0.090 s

(k) t = 0.100 s

Figure C.2: Comparison between animations

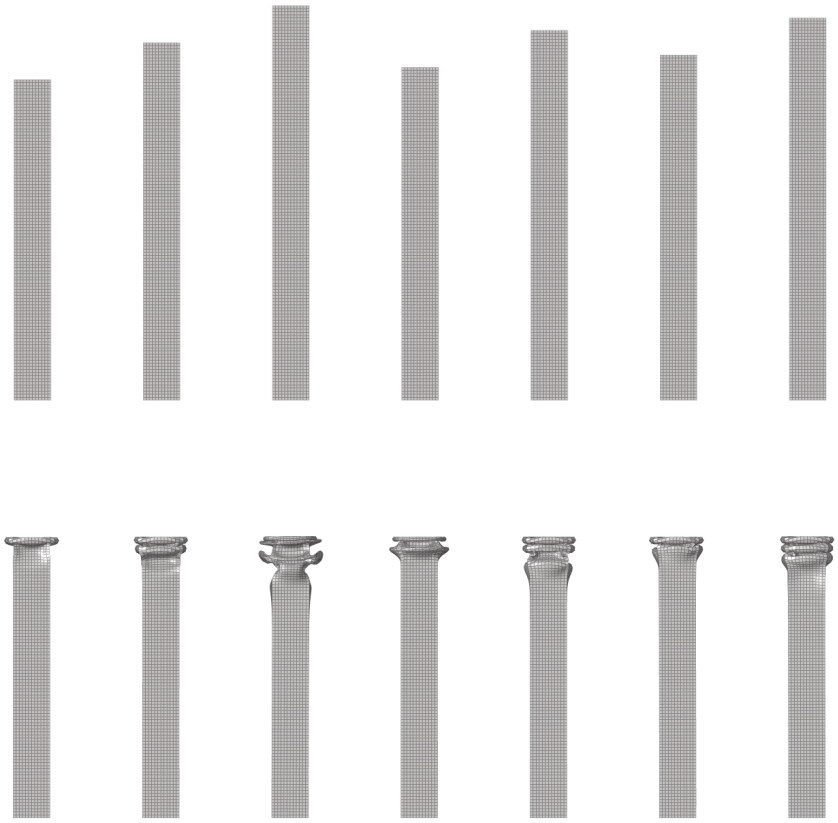

Figure C.3: Initial and final crash tubes' states